8-2017

Understanding the Structure-Function Relationships of Dendrimers in Environmental and Biomedical Applications

Bo Wang
Clemson University, bwang4@g.clemson.edu

UNDERSTANDING THE STRUCTURE-FUNCTION RELATIONSHIPS OF DENDRIMERS IN ENVIRONMENTAL AND BIOMEDICAL APPLICATIONS

A Dissertation
Presented to
the Graduate School of
Clemson University

In Partial Fulfillment
of the Requirements for the Degree
Doctor of Philosophy
Physics

---

by
Bo Wang
August 2017

Accepted by:
Dr. Feng Ding, Committee Chair
Dr. Emil Alexov
Dr. David A Lander
Dr. Jian He

ABSTRACT

We are living an era wherein nanoparticles (NPs) have been widely applied in our lives. Dendrimers are special polymeric NPs with unique physiochemical properties, which have been intensely explored for a variety of applications. Current studies on dendrimers are bottlenecked by insufficient understandings of their structure and dynamic behaviors from a molecular level. With primarily computational approaches supplemented by many other experimental technics, this dissertation aims to establish structure-function relationships of dendrimers in environmental and biomedical applications. More specifically, it thoroughly investigates the interactions between dendrimers and different biomolecules including carbon-based NPs, metal-based NPs, and proteins/peptides. Those results not only provide profound knowledge for evaluating the impacts of dendrimers on environmental and biological systems but also facilitate designing next-generation functional polymeric nanomaterials.

The dissertation is organized as following. Chapter 1 provides an overview of current progresses on dendrimer studies, where methodology of Discrete Molecular Dynamics (DMD), my major research tool, is also introduced. Two directions of utilizing dendrimers will be discussed in following chapters. Chapter 2 will focus on environmental applications of dendrimers, where two back-to-back studies are presented. I will start from describing some interesting observations from experiments i.e. dendrimers dispersed model oil molecules. Then, I will reveal why surface chemistries of dendrimers lead to different remediation efficiencies by computational modelings. Finally, I will demonstrate different scenarios of dendrimer-small molecules association.

Chapter 3 is centered on dendrimers in the biomedical applications including two subtopics. In the first topic, we will discuss dendrimers as surfactants that modulating the interactions between proteins and NPs. Some fundamental concepts regarding to NPs-Protein interactions such as NP-protein corona are also explained. In the following topic, I will look into amyloid protein aggregation mediated by dendrimers, which is of high expectations for combating amyloidogenic-related diseases. Chapter 4 concludes the whole dissertation. It also briefly introduces my ongoing projects and future research directions about dendrimers.

This dissertation has presented a systematic study of dendrimers in environmental and biomedical applications which might provide valuable information for future dendrimer design thus benefit the nanobiotechnology.

DEDICATION

To my parents, for their unconditional support and love.

ACKNOWLEDGMENTS

I would like to thank a lot of people who have been guiding me and supporting me along with my Ph.D. journey.

First of all, I would like to thank my committee members. My advisor Dr. Feng Ding is such a great mentor. He is so knowledgeable and always ready to help when I have questions. Dr. Emil Alexov is a good friend. He provides nice suggestions and visions when I discuss with him about my research ideas. Dr. David Lander is the best committee member you can expect. As he has a unique background, meeting with him always gives me a lot of inspirations. Dr. He always encourages me to conquer the difficulties and achieve academia success.

I also owe great gratitude for my longtime collaborator Dr. Pu Chun Ke, who is in Monash University (Australia) leading a bio-nano center. And I always refer him as my "mysterious fifth committee member". We have more than 10 publications together and there're definitely more to come in the future.

At last, I would like to thank fellow young talents in my groups. It's such a great time to working with you.

TABLE OF CONTENTS

Page

Table of Contents (Continued)

Page

LIST OF TABLES

LIST OF FIGURES

List of Figures (Continued)

Figure Page

List of Figures (Continued)

Figure Page

List of Figures (Continued)

Figure Page

CHAPTER ONE

AN OVERVIEW OF DENDRIMERS

Dendritic polymers at a glance

The name of dendrimers is adapted from Greek word "Dendron", which refers to branches or trees.[1] Besides dendrimers, other tree-like polymers (often termed as dendritic polymers) include hyperbranched polymers, dendrigrafts and dendronized polymers (Fig. 1.1).[2] A historical perspective of dendrimer studies, especially on the discovery of dendritic polymers, was well introduced by Donald A. Tomalia and Jean M. J. Frechet.[3] Since the first synthesis by Flory[4], dendritic polymers have received a lot of attentions due to the fact that they are representing the fourth major class of macromolecular architectures and a frequently observed structure in nature (such as trees in ecosystem or neurons network in humanbody).[5] Compared to other members of dendritic polymers, dendrimers are highly controlled in synthesis while appearing in a nearly perfect symmetrical conformation. Therefore, they are always picked as model polymers.

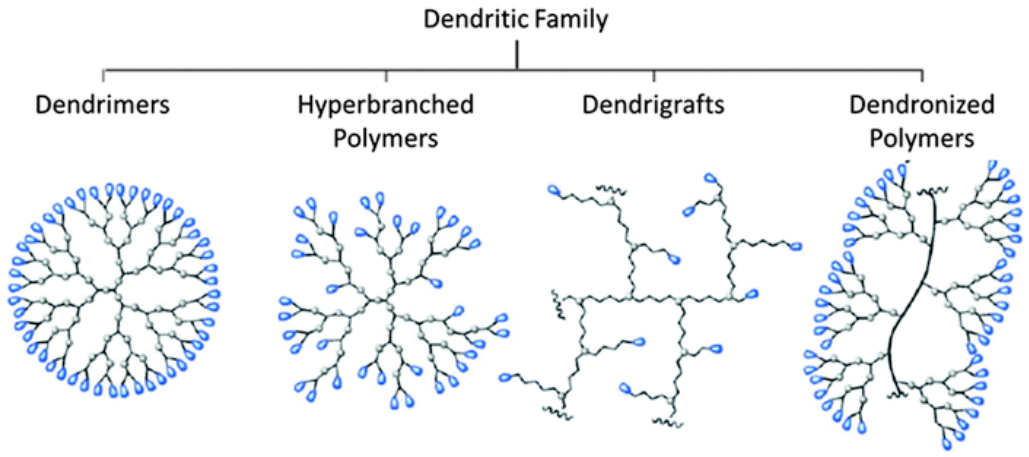

Figure 1.1 Schematic presentation of the dendritic family[2]. Reprinted with the permission from RSC.

After decades of explorations and optimizations, the general strategies for dendrimers' synthesis could be summarized into two categories i.e. divergent approach and convergent approach (Fig. 1.2).[6,7] However, several new approaches have also been reported with much improved efficiency including orthogonal chemistries, 'click' chemistries, fast non-'click' chemistries, hypercores and self-assembling dendrimers.[5,8] As a result, the production of dendrimers has gradually stepped out of the academic labs and entered into industry. And some common dendrimers species have already become commercially available. Examples are poly-amide-amine PAMAM (Starburst^{TM}), poly-etherhydroxily-amine PEHA (Priostar^{TM}), polyropyleneimine PPI (Astramol^{TM}). [9]

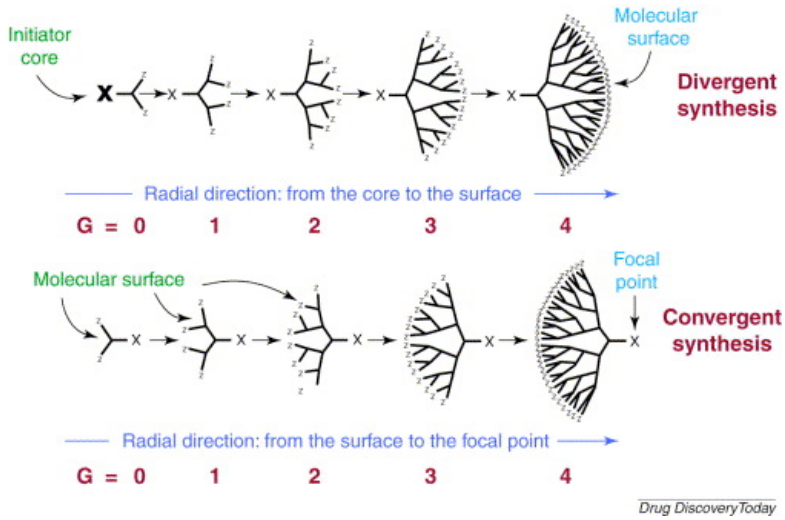

Figure 1.2 Divergent and Convergent approaches for dendrimer synthesis.[10] Reprinted with the permission from Elsevier.

Dendrimers are completely artificial macromolecules. So they are typically named after the monomers which they are constructed from. Dendrimers are also classified by "generations" i.e. how many branching layers they comprise of. Naturally, the size and number of atoms in a dendrimer are significantly increasing with the growing generation (Fig 1.3A). Over the years, striking efforts have been made on the atomistic characterization of dendrimers through both experimental and computational technics. Due to the large energetically permissible conformation space of dendrimers, it is difficult to probe the structural information through some traditional methods like diffraction, infrared or NMR.[11] And the first precise experimental measurement on dendrimers was performed by size exclusion chromatography (SEC), while results from small-angle neutron scattering (SANS), small-angle X-ray scattering as well as many other technics were also compared as references. [12–14] Growing evidences from existing

experimental measurements implied that dendrimers adopts remarkable monodispersed conformations.[5] These observations was further verified by the Molecular Dynamics (MD) simulations, which were powerful tools in providing atomistic details.[15] The first computational work on dendrimers was performed by Goddard and co-workers on the system of PAMAM dendrimers.[16,17] They found that among different generations (G1-G6), low generation dendrimers are less symmetrical comparing to high generation dendrimers. Another remarkable computational work was conducted by Maiti et al., who thoroughly investigated the structural properties of PAMAM dendrimers of G1-G11.[11] They not only verified that dendrimers of Generation 3-11 demonstrate a monodispersed and homogeneous structure but also provided a quantitative relationship between the size and the number of comprising monomers i.e. $R_g \sim N^{1/3}$.[11] Current progresses on dendrimer study from theoretical and computational approaches have been nicely reviewed by several groups including Tian et al. and Martinho et al. [15,18] Some important conclusions are listed as following: 1) Dendrimers demonstrate a well-defined structure comprising of three major components, namely, core, interior and shell. 2) Due to the unique physiochemical properties, dendrimers are perfect candidates for delivery vehicles/nanocontainer. And depending on the types of "cargos", dendrimers could ether load them inside the "protected" interior or conjugate them at the surface (Fig. 1.3B). 3) As dendrimers grow like fractals and are spherical in shape, calculations from radial density distribution illustrated that surface atom density is more sensitive with the increasing generation. Therefore, in high generation dendrimers (G11 and beyond), the surface will completely seals the interior space so that the whole dendrimers turn into a

"hard-sphere". This phenomenon is also referred as Gennes dense packing limit (Fig. 1.3B).[19] 4) Environmental factors like the properties of the solvent (good or poor), ionic strength, pH etc. also play big roles in determining the conformations of dendrimers (Fig. 1.3C). Understandably, a dendrimer whose interior is rich in hydrophobic components will become more compact in good solvent yet more expanded in poor solvent. Also, if the dendrimers are charged (i.e. easily protonated/deprotonated), the protonation states of charge atoms may altered in different condition thus leading to conformational changes of dendrimers.

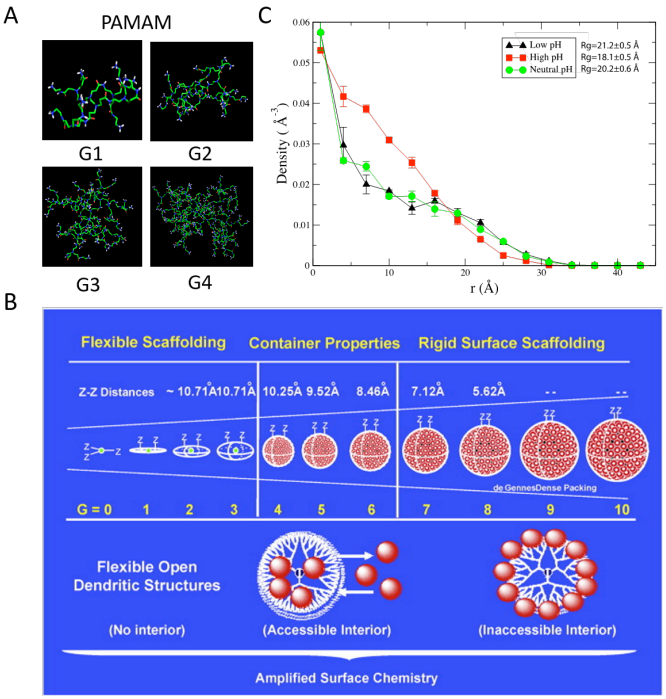

Figure 1.3 Structures and functions of PAMAM dendrimers. A) Snapshots of G1-4 PAMAM dendrimers in equilibrium conformations obtained from DMD simulations. B) Structures and functionalities of PAMAM dendrimers from G0-G10. The distances between surface charges are noted as Z-Z distance.[5] C) Radial density distribution of the G4 PAMAM dendrimer at different pH calculated by DMD simulation. C) reprinted with the permission from Elsevier.

Dendrimers possess many biomimetic properties and often considered as "artificial proteins" since they are dimensional similar to actual proteins.[21] Starting from their birth, dendrimers are of high biomedical expectations especially working as drug delivery vehicles, imaging agents, gene transfection agents or drugs.[8] A couple of nice reviews on biomedical applications of dendrimers could be found elsewhere.[1,5,9,10,15,18,22] Interestingly, the study of dendrimers has such a great influence on the field of biomedicine that several new concepts have been proposed along the time. For example, "Dendritic effect" was used to describe unique physiochemical properties of dendrimers that are evolving with generation level, which was also closely related to critical nanoscale design parameters (CNDPs).[23] "Dendrimer space" (Fig 1.4) was first proposed by Mignani et al that affords a new paradigm of thought for medicinal chemists and opens new promising avenues toward the identification of original dendrimer-based drugs.[24,25] To better facilitate the dendrimer-based drug screening process, a variety of toolboxes have been developed by the researchers from computational background (such as Dendrimer Builder Toolkit (DBT) from Maiti and coworkers[26]).

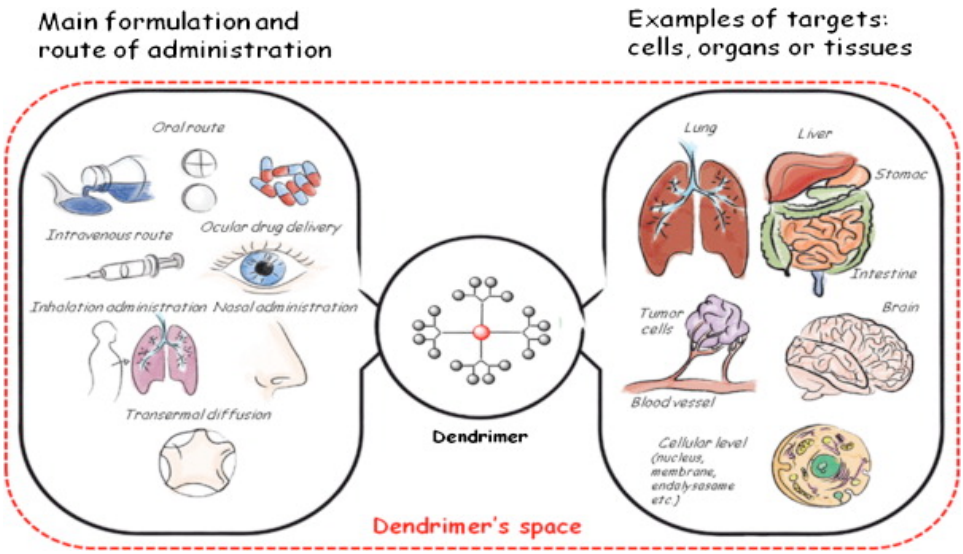

Figure 1.4 Main formulation, route of administration and targets using dendrimers.[24] Reprinted with the permission from Elsevier.

Dendrimers could also be applied into other applications such as environmental pollution remediation. A nice perspective on this topic was provided by Bhattacharya et al.[27] For instance, motivated by 2010 Deepwater Horizon Oil Spill, Geitner et al. examined the interactions of PAMAM dendrimers and hyperbranched poly(ehyleneimine) polymers with model linear and polyaromatic hydrocarbons. They found that both types of dendritic polymers were able to host model carbons yet yielding different mechansims.[28] On another study, DeFever et al. simulated naphthalenes encapsulated by PAMAM dendrimers of G3-G6 suggesting that dendrimers are able to remove contaminants from water.[29] Despite the current advances of applying dendrimers into different applications, it is still far from a established procedure to translate dendrimers into clinic or commercial use. More specifically, knowledge are greatly lacking in

following two aspects: 1) what's the impacts of dendrimers on environmental system and biological system? 2) What's the structure-function relationships of dendrimers?

Toxicities of dendrimers and dendrimer-protein interactions

NPs are circulating within environmental systems and eventually enter a given biological body via different paths. The corresponding impacts are often evaluated by toxicities or biocompatibilities. Duncan and Izzo nicely summarized current understandings of dendrimer biocompatibility and toxicity.[30] They introduced that although dendrimers are unique in conformations, their toxicities are no significant different from a typical polymeric NP such as copolymers.[30] Therefore, existing handbooks in terms of toxicities of other polymeric NPs are providing nice references to those of dendrimers.

It is well-known that NPs are able to interact with a variety of biocomponents due to their large surface-to-volume ratio.[31] Therefore, it is critical to explore the dendrimer-biomolecules interactions, which has a two-fold meaning: firstly, understanding those interactions could possibly elucidates the origin of dendrimer toxicity; secondly, considering the wide biomedical applications of dendrimers, we aim to reveal the binding mechanisms thus improving the functionalities of dendrimers. Growing evidences from experiments and computational studies indicated that electrostatic interactions are the major driving force between charged dendrimers and biomolecules (Fig 1.5A). [9,15,30,32] And a cationic surface is responsible for most toxic effects (Fig 1.5B). A well-known example is cationic PAMAM dendrimers, which causes cell death across different cell

lines tests.[30,32,33] Other factors that may cause toxic effects include the types of core and generations. While the core is shielded inside the dendrimer most of time, it might be exposed in changing environmental conditions or while dendrimers-biomolecules complexing. This is because dendrimers are soft polymeric nanoparticles and easily altered in conformation. In addition, hydrophobic interactions may also participate in dendirimer-biomolecules association especially for non-charged dendrimers.[9,30] As the toxicity often caused from the accessible surface terminal groups, high generation dendrimers are more likely reduced in toxicity due to the surface rigidity and crowding.[30]

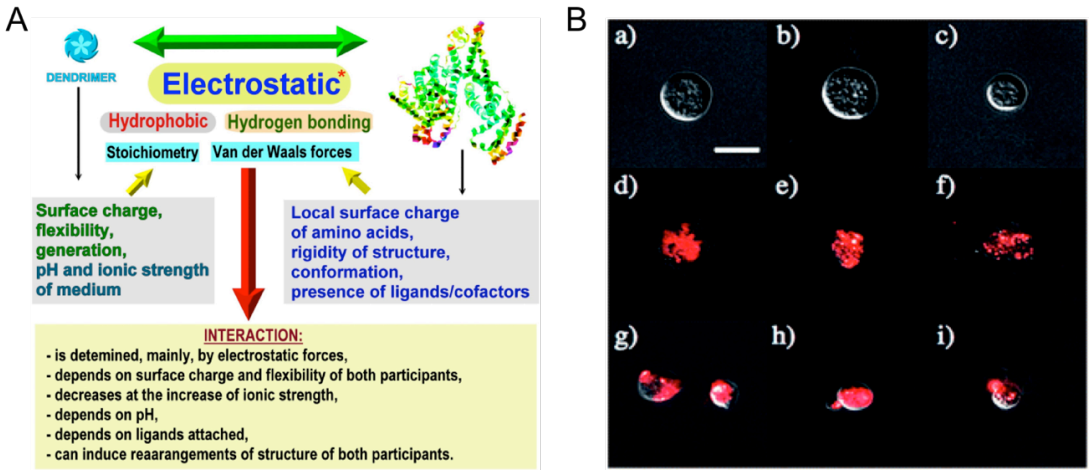

Figure 1.5 A) the mechanisms of interactions between dendrimers and proteins.[9] B) DIC and fluorescence overlaid images of amoebae. Controls (a-c) with no dendrimers, cells incubated with 10 μM SCC-labeled dendrimers alone (d-f) and cells incubated with 10 μM PN-loaded SCC-labeled dendrimers (g-i). Scale bar: 10 μM[32]. A) reprinted with the permission from Elsevier, B) reprinted with the permission from RSC.

Different strategies have been proposed to eliminate toxicity while the most popular one, also known as "anti-fouling", is substituting toxic surface terminal groups into non-toxic ones. For instance, once modified the cationic surface of PAMAM

dendrimers by neutral or anionic derivatives the toxicities were observed significantly dropped, which is most likely due to the interactions between dendrimers and the underlying biocomponents were reducing.[30] Grafting NPs with polyethylene glycol (PEG) has already become "gold standard" for "anti-fouling". Therefore, the structural and physiochemical properties of PEGylated dendrimers have been investigated by many studies, which concluded that variables like dendrimer generations, PEGylation densities, and molecular weights of PEGs could significantly alter the microstructure of PEGylated dendrimers (Fig. 1.7).[34–36] Despite the fact that surface modifications improve the biocompatibilities of dendrimers, they may be at the penalty of reducing loading efficiency. For intense, in the case of PAMAM-based dendrimers, a negatively charge surface might be back-folded making contact with the interior protonated amines thus occupying the interior space.[37] Long PEG chains might also create a "PEG cloud" thus preventing drug loading and releasing.[34] In summary, it still requires much more computational and experimental tests to verify optimized structures for dendrimers.

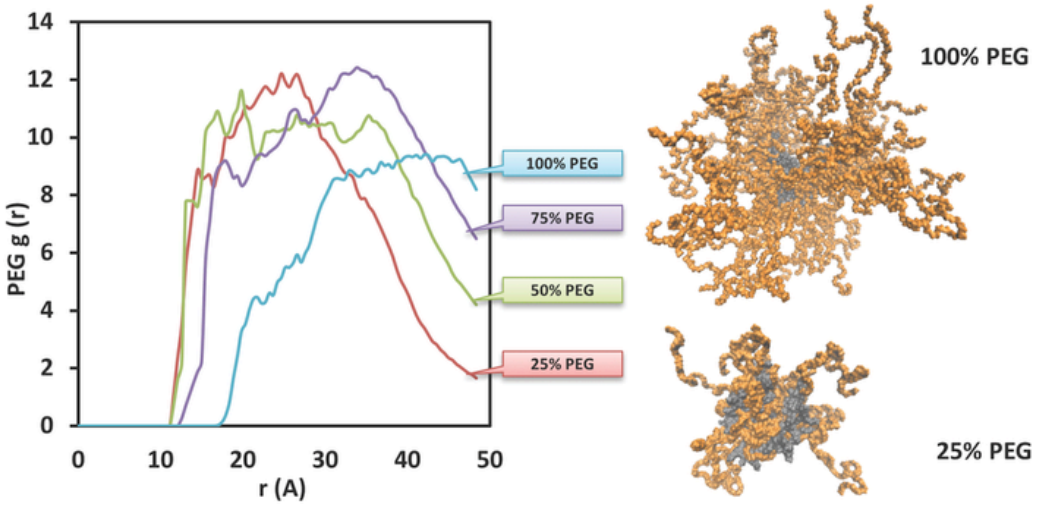

Figure 1.6 Radial distribution functions (RDFs) and structural representations of PEG chains in PEGylated PAMAM-G4 systems obtained from simulations. Water molecules and counter ions have been omitted for better visualization. [35] Reprinted with the permission from John Wiley and Sons.

Investigating structure-function relationships of dendrimers

With increasing knowledge, we were gradually building up libraries that capture the functionalities of dendrimers of different species and generations. For example, low generation dendrimers like G1-G3 have been used as flexible scaffolding; G4-G5 dendrimers are nanocontainers utilizing their encapsulating abilities; G6-10 are used like rigid scaffold nanoparticles (Fig 1.3B).[5] Much efforts have also been put on screening dendrimer-based pharmaceuticals or strategies of loading drugs on dendrimers.[24,25] More specifically, the core and constructing monomers are tailored to achieve maximum binding affinities for drugs or designated functions. To further explore other possible applications and improving the biocompatibility, researchers have kept testing more and more biomolecules including different types of membranes, proteins, DNA/RNA etc. [9]

However, current literatures about dendrimers are predominately focused on describing the phenomenological effects of adding dendrimers to different systems. In other words, the physiochemical properties of dendrimers are analyzed on a case-by-case basis. As a result, the observations from an existing dendrimer-ligand system cannot transfer or predict the behaviors of new dendrimer-ligand systems. For example, a unimolecular micelle diagram has been frequently used to depict dendrimer-ligand associations. Yet it failed to explain several contradicted observations from different dendrimer-ligands system.[28] On another example, it has been reported that dendrimers are able to regulate protein amyloid aggregation.[9,38] Inspired by those results, further studies verified that some dendrimers such as cationic PAMAM dendrimers are able to inhibit amyloid protein self-assembly [25] thus potentially used to treat amylodogenic-related diseases e.g. Type II Diabetes[39], Alzhemimer's Disease[40]. However, detailed inhibition mechanisms from those dendrimers are far from well explored. At current stage, we could only concluded that the mediation effects are co-determined by several factors including the dendrimers species, surrounding environment (such as global charges, ionic strength) and properties of ligands.[9,38] Therefore, we are still looking for a more practical and predictable model that well representing the structural-function relationships of dendrimers.

Molecular simulations are among the best approaches to fulfill this goal. However, as dendrimers are featured as complicated macromolecules with huge numbers of atoms especially for those in high generations, current computational studies are bottlenecked by several difficulties. To start with, traditional all-atom molecular dynamics (MD)

simulations are most popular approaches as they are able to provide enough atomistic detailes. Yet all-atom MD are very time-consuming and computational expensive. Therefore, it is not a feasible approach in simulating complicated systems such as high generation dendrimers or systems with multiple-ligands involved. While coarse-graining simulations may act as alternative methods especially in investigating the kinetics of large systems, they often fail to provide enough details for binding, which is critical information for drug design. In this dissertation, I will demonstrate a new in-house developed molecular dynamic – Discrete Molecular Dynamics (DMD) which might be provide a nice solution for those difficulties. It is therefore used as my primary tool in studying dendrimers.

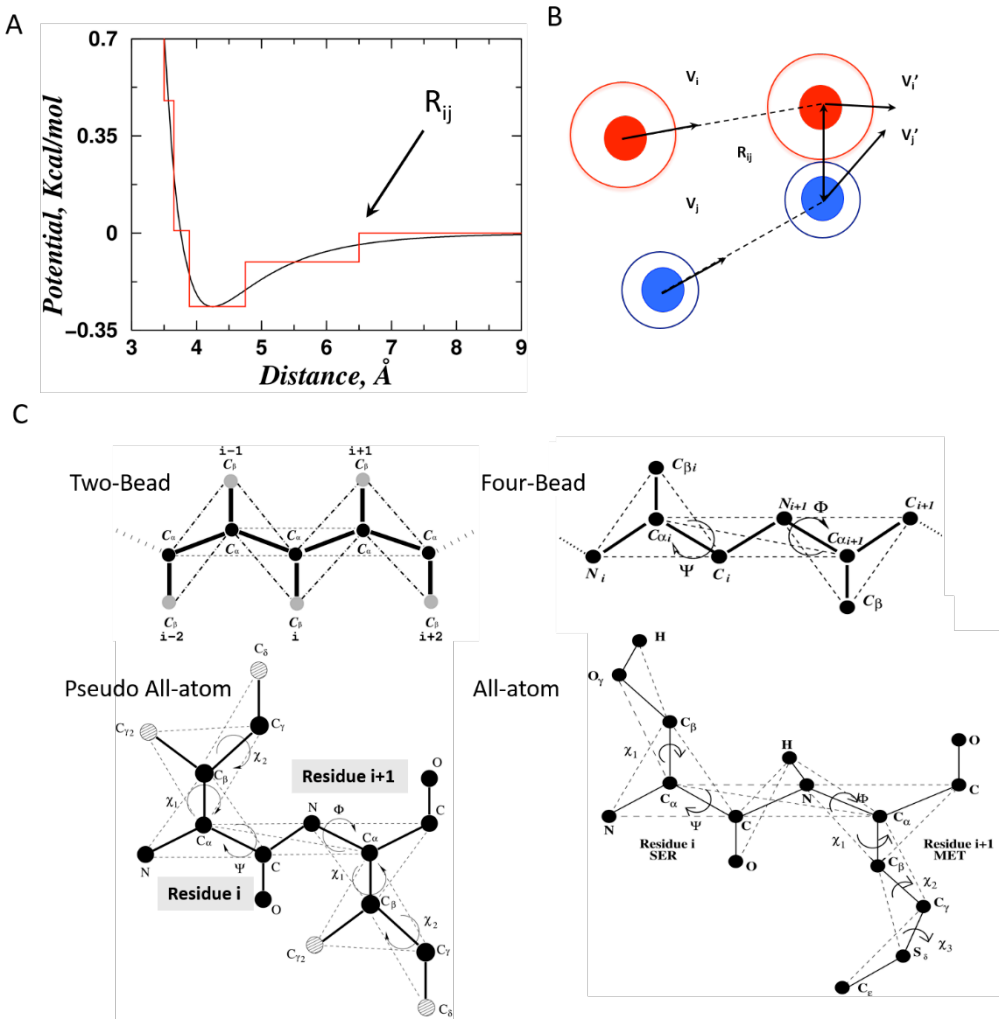

Figure 1.7 A) Approximating the inter-atomic potential between atoms i and j by discrete potential functions and B) one "collision" event happened between atoms i and j, when their statues of motions will be updated[41] C) Two-Bead, Four-Bead, Pseudo All-atom, and All-atom Modeling in DMD.[42,43]

DMD simulations are developed based on the traditional molecular dynamic simulations, where a couple of optimizations have been implemented. In DMD, continues potentials have been replace by discretized potential functions and the statue of motion for each atom is only updated in some special events such as "collision" (Fig. 7A&B). In addition, we applied an implicit solvent model to average the effect from water molecules.

Those features bring a significant improvement in calculation efficiency, which opens opportunities to simulate complicated system on longer time scales at low cost. DMD simulations are able to model molecules in different dimensional approximation from coarse-graining to all-atom (Fig. 7C). The inter-atomic interactions are adapted from the Medusa force field including electrostatic, van der Walls (VDW), H-bond, and solvation. Solvation energy are calculated based Lazaridis-Karplus EEF1 model.[44] The H-Bond was modeled using a reaction-like algorithm.[45] And charge screening effects are modeled from the Debye-Hückel approximation where the values for ionic strength is assigned based on intrinsic properties of simulated system.

DMD simulations have been proved an effective approach in describing the behaviors of proteins[43,46,47], polymer[48], and nanoparticles[49]. In this dissertation, I introduced DMD in investigating dendrimers-biomolecules interactions. Chapter 2 is mainly about dendrimers in environmental applications that includes two closely related studies "Structure-function relationship of dendrimers" and "Mechanisms of dendrimer-small molecules binding". By simulating different dendrimer-ligand systems, the first one serves as a benchmark study showing that DMD simulations recapitulate the structures and dynamics of dendrimers with high accuracy. In the second study, I will reveal another mechanism of dendrimer-ligand association deviated from the popular unimolecular micelles paradigm. Chapter 3 put more emphasis on dendrimers in biomedical applications. It contains two studies, namely, "Dendrimers as surfactants" and "Dendrimers inhibit protein amyloid aggregations". The first study introduced a lot of important concepts about NP-protein interactions since dendrimers could be considered

as polymeric NPs. That hybridizing two or more functional nanoparticles together becomes very popular strategy in the field to achieve an enhanced functionality. In this light, the first study could also taken as a nice example of using dendrimers as surfactants functionalizing metal-based NPs. In the second study, I demonstrate a pioneer work of applying dendrimers in inhibiting self-assembly of human Islet Amyloid Peptide (hIAPP), which is believed closely associating with Type 2 Diabetes (T2D). My studies on dendrimers will be summarized in Chapter 4, where future directions will also be presented. In conclude, I hope my research could help design dendrimers with better functionalities and biocompatibilities.

CHAPTER TWO

DENDRIMERS IN ENVIRONMENTAL APPLICATIONS

Structure-Function relationships of dendrimers

Geitner, N. K.; Wang, B. et al. Structure-Function Relationship of PAMAM Dendrimers as Robust Oil Dispersants. Environ. Sci. Technol. 2014, 48 (21), 12868-12875. Reproduced in part with permission from American Chemical Society

1. INTRODUCTION

Originally proposed by Paul Flory,[50] dendritic polymers are a class of macromolecules consisting of highly branched polymer units. Within this class are dendrons, dendrimers, and hyperbranched polymers.[50] Dendrimers can be precisely synthesized with high order and monodispersion, with well defined branching units emanating from a central core.[50] The number of these branching iterations is termed the Generation of the dendrimer and determines its size, structure, and function. Hyperbranched polymers, in contrast, possess less well-defined branched interiors, resulting in a higher polydispersity at a much lower production cost. Due to their unique physicochemical properties, there are a wide variety of current and potential applications of dendrimers ranging from environment to energy and biomedicine. For example, hydroxyl-terminated PAMAM dendrimers have been shown to remove contaminants such as humic acids[51] and metal ions[52,53] from drinking water or contaminated soils. Dendrimers can be used in light-harvesting applications for superior transduction efficiency in diodes and other photonic devices.[54,55] The surface functionality of PAMAM dendrimers has been altered to include long-lifetime ibuprofen release *in vivo*[56]

and conjugation with partially anionic folate-conjugates has been explored for the delivery of anti-arthritic drugs.[57] The ability of dendrimers to encapsulate small organic molecules has also been studied in terms of dendrimer generations[58] as well as the shape of a guest molecule,[59] demonstrating a wide array of hosting capabilities of dendrimers in aqueous solution.

Given their hosting capabilities, we have previously proposed PAMAM polymers as oil dispersants,[28] and showed that cationic PAMAM dendrimers are capable of hosting both polyaromatic and linear hydrocarbons in water.[28] Conventionally, lipid-like oil dispersants have been in use since at least the 1960s[60] and also during the large scale Deepwater Horizon disaster of 2010. However, concerns over the potential toxicity of conventional oil dispersants have been recently raised.[61–63] There is a renewed and pressing desire for effective yet biocompatible dispersing agents. Our previous work has shown, however, that highly cationic amine-terminated poly(amidoamine) (PAMAM) dendrimers cause acute toxicity in amoebas at a high concentration.[32] Similarly, several other studies have also shown that highly cationic PAMAM dendrimers cause significant charge-induced toxicity *in vitro*[64–67] and rapid blood clotting *in vivo*.[68] It has been suggested that the electrostatic interaction between highly cationic PAMAM and negatively charged cell membrane results in pore formation to trigger cytotoxicity. Therefore, efforts are increasingly being focused on altering dendrimer terminal charges in order to reduce the toxicity or improve the efficacy of dendrimer agents.[27,69]

Many studies have been conducted on the size, structure, and dynamics of dendrimers depending on dendrimer generation[70,71] and environmental conditions such as

solution pH and ionic strength.[70–74] It has been shown that PAMAM dendrimers adopt globular-like structures with the repeating monomers loosely packed in the interior and the surface groups protruding, forming hydrogen bonds with water. Simulations revealed dynamically forming pores in the interior that can bind various guest molecules.[70,75] Solution pH and ionic strength can also affect dendrimer structure by changing the dendrimer protonation states and screening of electrostatic interactions, respectively.[72,73,76] It is not understood, however, how surface modifications of dendrimers, a common strategy in dendrimer design and synthesis, might affect their size, structure, dynamics, and subsequent functionality.

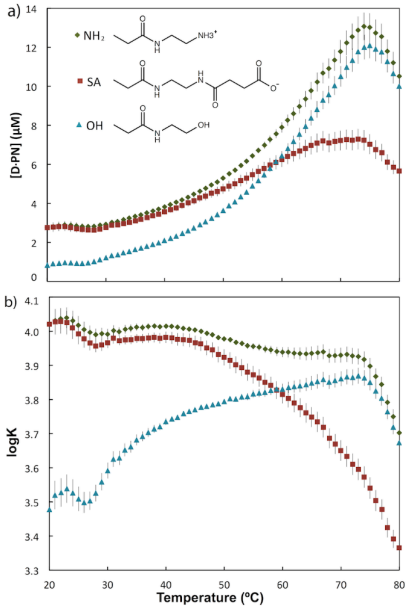

Figure 2.1 The concentration of dendrimer-associated phenanthrene (a) and the corresponding logK association constants (b) for G4-NH_2 (green diamonds), G4-SA (red squares), and G4-OH (blue triangles). Error bars are standard deviations of 3 independent trials. Note clear transition temperatures at 74ºC where binding with phenanthrene becomes much less efficient. The inset in (a) shows the chemical structures of a single terminal chain of G4- NH_2, -SA, and -OH from top to bottom.

Here, we investigate the effects of varying the surface charge and functionality on dendrimers' ability to serve as effective oil dispersants. Specifically, we examine cationic amine-terminated (G4-NH_2), neutral hydroxyl-terminated (G4-OH), and anionic succinamic acid-terminated (G4-SA) PAMAM dendrimers (Fig. 2.1a). Synergistic experiments and molecular dynamics simulations are performed to probe the interactions, limitations, mechanisms, and differences between cationic, anionic, and neutrally charged PAMAM dendrimers with linear, polyaromatic, and hybrid hydrocarbons as well as the combination thereof. These various combinations of hydrocarbon are studied in order to gain a more fundamental understanding of dendrimer oil dispersant interactions with the various hydrocarbon components of crude oil as well as illuminate any potential synergistic dispersion effects of hydrocarbon mixtures. The advantages of model hydrocarbons over whole crude oil include the real-time tracking and accurate quantification for mechanistic studies of the structure-function relationship. Additional studies of dendrimer dispersion efficacy and toxicity with crude oil have been done in a separate work. The implications of this study reach beyond oil dispersion to other biomedical and environmental applications including drug delivery and water purification, noting the differences in dendrimer interactions with aliphatic and aromatic hydrophobic molecules as well as potentially unanticipated effects of altering dendrimer surface functionality. We find that marked differences in hosting capacity for hydrocarbons arise from changes in both the structure and dynamics of the dendrimers with varying terminal functionality.

2. EXPERIMENTAL AND COMPUTATIONAL METHODS

2.1 Materials and Characterization. All dendrimers were purchased from Dendritech, Inc. and were PAMAM G4.0 (generation four) in water solvent and stored at 4°C. Phenanthrene (PN) and octadecylbenzene (ODB) were purchased from Sigma-Aldrich, hexadecane (C_{16}) from Acros Organics and all stored at room temperature. The dendrimer stock solutions were diluted in DI water (18 MΩ cm) to a final concentration of 15 μM, and their pH adjusted to 8.2 to mimic that of seawater using 1M NaOH and 1M HCl. Dynamic light scattering (DLS) and zeta potential characterizations of these prepared stock solutions were carried out on a NanoBrook ZetaPALS.

2.2 UV-vis Spectophotometry and Phenanthrene Affinity. UV-vis spectroscopy absorbance measurements were performed on a temperature-controlled Cary 300 Bio (Thermo Electric Corp.). To normalize the concentration of PN, a known quantity was dissolved in methanol and the intensity of the absorbance peak at 251 nm was measured. This relation was then used to calculate all other PN concentrations. The concentration of dendrimer-associated PN was calculated using Eqn. (1) where $[PN]_T$ is the total observed concentration of PN in the column and $[PN]_S$ is the concentration of free PN in solution.

$$[D \cdot PN]=[PN]_T-[PN]_S \quad (1)$$

A solution of 15 μM dendrimers was used as a control in all measurements of PN with dendrimers. Each sample was prepared with 1 mg of PN added to 2 mL of either water or dendrimer stock solution. Samples were bath sonicated for 5 min (Branson) in order to break PN solids and then rotated overnight to reach equilibrium. We then measured the

affinity of dendrimers for PN in water as a function of temperature by measuring the absorbance of PN over a temperature range from 20-80ºC. The temperature was increased at a rate of 0.1ºC/min, and absorbance was measured every 1.0 ± 0.02ºC. These measurements were made in triplicate in sealed quartz cuvettes. The apparent association constant K was calculated using Eqn. (2) where [D] is the free dendrimer concentration.

$$K=[D\cdot PN]/([D][PN]_S) \quad (2)$$

Solutions of PN dissolved in C_{16} were prepared such that the final solution was 8% PN by weight dissolved in C_{16}. For sample incubations, 20 μL of this stock was added to 2 mL of either water or dendrimer solution and then rotated for 1 h. This ensured that the same total mass of PN was added as in the pure PN experiments. The same temperature ramp as above was then performed, again by measuring the absorbance of PN at 251 nm.

2.3 Fluorescence. Fluorescence measurements were performed on a temperature-controlled Cary Eclipse fluorometer (Thermo Electric Corp.). ODB-doped C_{16} stock was prepared such that the hydrocarbon solution was 2.6% ODB by weight. For all measurements with ODB, 65 µL of stock solution was added to 2 mL of water or dendrimer solution and then rotated gently for 1 h. It was then allowed to settle, and solution was pulled from the middle of each tube to avoid phase-separated oil. Then 20 µL of stock ODB-doped C_{16} was added to each cuvette to ensure a consistent excess of available hydrocarbons. The fluorescence emission was observed at both wavelengths of 290 nm and 299 nm, with an excitation wavelength of 258 nm in both cases. The

fluorescence emission intensities were recorded every 1.0 ± 0.02ºC in the same temperature ramp as described in Section 2.2.

2.4 DMD Simulations. Discrete molecular dynamics (DMD) is a special type of molecular dynamics algorithm, featuring rapid dynamics sampling efficiency. The detailed algorithm and force field parameterization of DMD can be found elsewhere.[43] We used a united atom representation to model the molecular system, explicitly modeling all polar hydrogen and heavy atoms and with implicit solvent. Inter-atomic interactions were modeled by a physical force field adapted from Medusa,[45,77] which included Van der Waals (VDW), solvation, electrostatic and hydrogen bond interactions. The force field parameters for VDW interactions, bond length, angle and dihedrals were taken from CHARMM 19.[78] The solvation energy was included using the Lazaridis-Karplus implicit solvent model.[79] The distance and angular dependant hydrogen bond interaction was modeled using a reaction-like algorithm.[45] We used the Debye-Hückel approximation to model the screened electrostatic interactions between charged atoms. The Debye length was approximately 10 Å by assuming water relative permittivity of 80, and a monovalent electrolyte concentration of 0.1 M.

The starting structures of dendrimers were generated by constructing the idealized 3-dimensional dendrimer structure consisting of a core, branching units, and terminal groups, followed by equilibration and energy minimization. To emulate a solution pH of 8.2, all G4-NH_2 and G4-SA terminal groups were charged (protonated and deprotonated, respectively). All tertiary amines in G4-NH_2 and G4-OH were deprotonated and therefore

uncharged. To model the partial protonation of tertiary amines in the presence of acid terminal groups, the protonation state of the interior tertiary amines of G4-SA was varied, where 0, 10, 20, or 30% of randomly selected tertiary amines were protonated. In our simulations, the net charges of the molecular systems were maintained zero by adding offsetting charges, such as chloride (Cl^-) and sodium (Na^+) ions. After the initialization of dendrimer structures, energy minimization using DMD was carried out for 10,000 time steps (approximately 10 ns) before carrying out further equilibrium simulations.

In DMD simulations, temperature is in the unit of kcals/mol·k_B, where k_B is the Boltzmann constant. Our simulations were conducted for a temperature range of 0.55-0.75 kcal/mol·k_B, corresponding approximately to 275-375 K. The Anderson's thermostat[80] was used to perform constant temperature simulations. At each temperature, energy minimization was first carried out for 10 ns and the simulations were conducted for 2 million time steps (approximately 1 μs), corresponding to an average of approximately 72 CPU hours. We characterized the sizes of all three types of dendrimers by measuring the radius of gyration (R_g) as a function of temperature. The mean and standard deviation of R_g were obtained from 8,000 snapshots evenly distributed throughout the final 800 ns of simulation.

3. RESULTS AND DISCUSSION

Distinctive Physicochemical Properties of Dendrimers with Modified Terminal Groups. Generation 4 PAMAM dendrimers of positively (NH_2), negatively (SA), and neutrally (OH) charged functional groups, all at pH 8.2, were first incubated with PN. We

measured the concentration of saturated PN in water and in dendrimer solution with an excess of PN (see Eqn. (1), section 2.2 in Methods; Fig. A1), and computed the concentration of dendrimer-associated PN [D·PN]. We determined the [D·PN], quantifying the capacity of dendrimer to host PN, as a function of temperature (Fig. 2.1a). The temperature range of 20-80 ºC was chosen to examine the fundamental differences in dendrimer behavior and interactions with hydrocarbons at environmentally relevant temperatures and beyond. Initially, the positively and negatively charged dendrimers have similar hosting capacities, while the neutrally charged dendrimer has lower hosting capacity. As temperature increases in all cases there is an increased hosting of PN by dendrimers, in part due to the increasing availability of PN in solution with increasing temperature. This trend continues until approximately 74ºC for positively and neutrally charged dendrimers, at which point the PN hosting capacity reaches a peak followed by a marked decrease. In contrast, negatively charged dendrimers reach their maximum capacity between 65-74ºC, reaching just 56% the maximum PN hosting of G4-NH_2.

With the measured PN concentrations in water and in dendrimers as well as the concentration of dendrimers in solution, we can calculate the apparent association constants, K (see Eqn. (2), Section 2.2 in Methods) and compute logK as a function of temperature (Fig. 2.1b). For NH_2 and SA-terminated dendrimers, we observe relatively constant, large apparent association constants at low temperatures. In contrast, the neutral OH-terminated dendrimers had a much lower affinity at low temperature, but this affinity surprisingly increases rapidly with respect to increased temperature and becomes nearly identical to the NH_2-terminated affinity near 70ºC. Both G4-NH_2 and G4-OH dendrimer

affinity for PN sharply drop at 74ºC, as expected (see Fig. 2.1a). Despite the more significant and gradual decrease in G4-SA affinity, we note an increase in this rate of decrease at the same 74ºC, indicating the temperature at which it becomes thermodynamically more favorable for PN to dissolve in water than to be partitioned inside of the dendrimers, as PN water solubility increases exponentially with temperature over the observed range (Fig. A1). Therefore, the changes in dendrimer surface charge result in drastic changes in its hosting capacity of PN and the temperature dependences. However, since PN is non-charged and the binding is not governed by electrostatic interactions, it is intriguing as what the molecular mechanism is for such drastic changes in hydrocarbon hosting capacity upon adjusting the dendrimer surface charges.

Table 2.1: Characterization of PAMAM Dendrimers[a]

Functionality	D_H (nm)	ζ (mV)
NH_2	4 ± 1	30.7 ± 2.9
OH	3 ± 1	-0.9 ± 1.0
SA	4 ± 1	-18.5 ± 2.0

a) D_H: Hydrodynamic diameter. ζ:Zeta Potential

We postulated that the changes are mostly in the structure of dendrimer, which in turn affect the hosting function of dendrimer. We first characterized the size and charge properties of all three types of dendrimers in solution (Table 2.1) using DLS and PALS zeta potential measurements, respectively (Methods). The DLS results suggest that the dendrimers are fairly monodisperse and tend not to aggregate in DI water. Second, that the OH-terminated dendrimers have smaller hydrodynamic diameters (D_H) than their

charged counterparts. The zeta (ζ) potential quantifies the dendrimer net electrokinetic potential in solution. We find that, indeed, the OH-terminated dendrimers carry nearly zero net charge and the amine-terminated dendrimers are highly positively charged (+30 mV). Interestingly, the SA-terminated, while negatively charged, carry a net charge with significantly smaller magnitude than the amine-terminated. This reduction of overall net charge suggests that some of the interior tertiary amines in SA-terminated dendrimers may become protonated at this pH. Assuming electric multilayers similar in nature, the measured differences in zeta potential magnitude suggest the protonation of approximately 30% of G4-SA tertiary amines. Such a significant shift in pKa of the tertiary amine compared to neutral and positively charged dendrimers is feasible in the presence of a large number of terminal acidic groups in the vicinity.[81] These characterizations suggest significant physicochemical differences in PAMAM dendrimers caused simply by varying the terminal functionality. Next, we perform molecular dynamics simulations to study the changes of dendrimer size and structure with respect to surface charges at the molecular level.

We performed DMD simulations of all three dendrimer classes (Methods) and measured the radius of gyration (R_g) as a function of temperature (Fig. 2.2a) for each case. For the SA-terminated dendrimers, we studied the effect of partial protonation of their tertiary amines, with levels of protonation ranging from 0-30% protonation, where 30% tertiary protonation corresponds to the experimentally observed zeta potential of G4-SA. In DMD simulations, the dendrimer rapidly reaches equilibrium with *Rg* fluctuating around its average value in a long timescale simulation trajectory (~50 ns;

Fig. A2). Across the simulated temperature range, the R_g of G4-NH_2 increases from 19.4 Å to 21.25 Å, in agreement with small angle neutron scattering (SANS) experiments as well as atomistic molecular dynamics (MD) and coarse-grained (CG) simulations performed elsewhere (Table 2.2, Fig. A3).[20,36,82–85] Because R_g is an averaged single-value measurement, we also calculate the radial density function (RDF) to quantify the internal structure of dendrimers (Figs. A4 & A5). As observed previously in an all-atom MD simulations[36], we find that lower generations G2-G3 exhibit more compact core structures while higher generations G4-G5 are more open due to increased electrostatic repulsion between terminal groups (Fig. A4). We also computed the RDF for the G4-NH_2 dendrimers at different pH values. At high pH, the primary amines are fully deprononated, making the dendrimer neutrally charged. At low pH, the tertiary amines are protonated and the dendrimer is fully charged. Our results confirm the expected transition from dense-core at high pH to dense-shell configuration at neutral and low pH as observed in previous all-tom MD simulations (Fig. A5).[20] These benchmark results validate our DMD simulations efficient and robust for studies of dendrimer structure and dynamics. G4-SA is, across the simulated temperature range, larger than G4-NH_2 due to the slightly longer terminal groups. Their R_g values decrease with increasing tertiary amine protonation, and at the lowest tested temperature it reduces from approximately 22.25 Å at 0% protonation to just 20.0 Å once 30% of the interior tertiary amines have been protonated. This size change is because of the electrostatic attraction between these protonated groups and the negatively charged terminal carboxyl groups. This attraction also limits the expansion of G4-SA with temperature: e.g. G4-SA (30%) swells just 1.25

Å compared to a 1.9 Å growth seen in G4-NH_2, resulting in equal R_g values at the highest temperature in simulations.

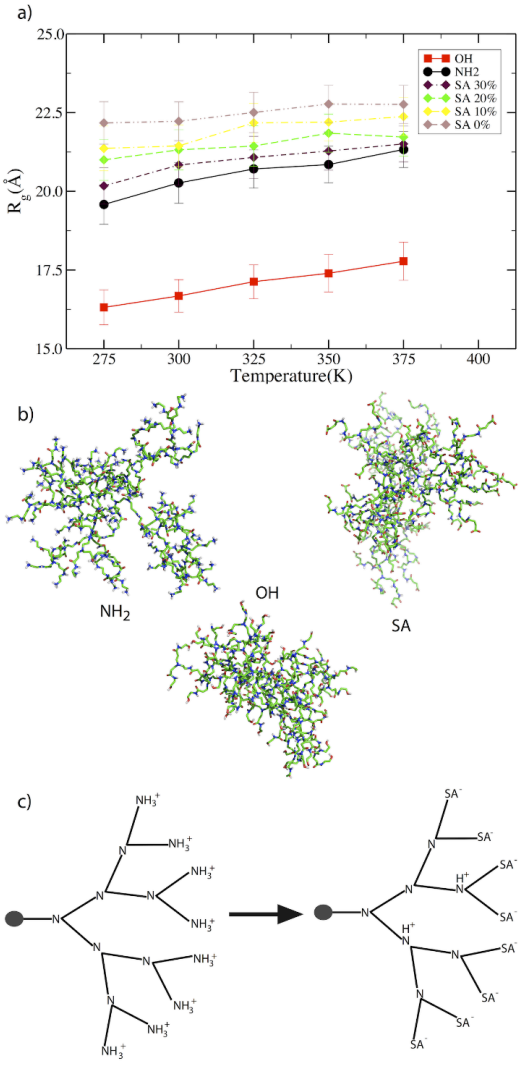

Figure 2.2 Radius of gyration (R_g) for G4-NH_2, OH, and SA for SA tertiary amine protonation fractions of 0-30% (a). Error bars are standard deviations taken across the 800 snapshots used in R_g calculations. Representative DMD snapshots of G4 PAMAM dendrimers at room temperature (b), which illustrates the effect of changing terminal group chemistry on the overall structure of the dendrimer. Differences in structure between G4-NH_2 and G4-SA are due to partial protonation of SA tertiary amines (c), with a portion of the dendrimer structure shown schematically emanating from a central core.

Table 2.2: Comparison of R_g in PAMAM dendrimers from various works

	R_g (Å)		
	G3	G4	G5
Liu et al. - SANS[84]	16.7 ± 1.2	21.4 ± 0.4	26.8 ± 0.4
Lee & Larson- CG[85]	13.1 ± 0.1	---	23.2 ± 0.1
Liu et al. - MD[20]	15.8 ± 0.3	20.6 ± 0.2	25.3 ± 0.1
Yang & da Rocha – MD[36]	15.0 ± 0.9	21.8 ± 0.8	23.8 ± 0.2
This Work (300 K)	15.7 ± 0.6	20.2 ± 0.6	25.7 ± 0.4

While amine- and SA-terminated dendrimers have similar sizes across the entire temperature range, G4-OH is clearly smaller than its charged counterparts, expanding from an R_g of 16.25 to 18.13 Å at the lowest and highest simulation temperatures, respectively. This markedly smaller size is due to the lack of electrostatic repulsion between terminal groups and hydrogen bond formation between the terminal hydroxyl groups, resulting in a much more compact dendrimer structure (e.g. typical snapshot structures in Fig. 2.2b).

These differences in size and how sizes change with temperature in simulations is consistent with the experimentally observed differences in apparent affinity for PN as in Fig. 2.1. G4-OH has a much lower affinity for PN at low temperatures because, at those temperatures, they are significantly more compact than either G4-SA or -NH_2, thus reducing the size and accessibility of the interior voids to host PN as illustrated by the dense-core structure of the neutrally charged dendrimer (Fig. A4). As temperature increases, the G4-OH expands with increased R_g by breaking the hydrogen bonds, thereby granting access to its growing interior cavities. Our zeta-potential characterization of G4-NH_2 and G4-SA suggests that approximately 30% of the G4-SA tertiary amines are protonated (Fig. 2.2c) assuming tertiary amines in G4-NH_2 are not

protonated.[27] This change allows strong electrostatic interaction between terminal groups and the protonated tertiary amines, which causes the dendrimer to contract relative to the less protonated G4-SA dendrimers. Such strong electrostatic interaction also noticeably inhibits size expansion with temperature in contrast to the weaker hydrogen bond interaction in G4-OH (Fig. 2.2a). As a result, the G4-SA features a lower host capacity and apparent affinities for PN compared to G4-NH_2. These differences in swelling behavior highlight why the temperature dependence in PN hosting capacity is different for each dendrimer despite all three functionalizations growing with increasing temperature. Such a dependence on hydrophobic core accessible for hosting small hydrophobic molecules is in agreement with earlier studies by Tomalia *et al* with lipophilic dye encapsulation by dendrimers of various generations.[58] In addition, since the dendrimer volume available for hosting increases rapidly as the cubic power of the size, a small change in *Rg* (Fig. 2.2) leads to large changes in hosting capacity (Fig. 2.1). It is also important to note that, by charging a fraction of the interior groups, the interior voids become slightly less hydrophobic and thus less favorable for hydrocarbon interactions. Another interesting observation in experiments is the sharp decrease of PN binding at 74ºC for all dendrimers (Fig. 2.1). We hypothesize that this phenomenon is due to the intrinsic structural properties of dendrimer at different temperatures. As the dendrimers expand with increasing temperature (Fig. 2.2), the cooperative binding with PN due to interactions among amidoamine monomers is reduced. At high temperatures, the binding is dominated by the interaction between PN and amidoamine monomer. Therefore, the

transition at 74ºC is the result of dissociation of PN from amidoamine monomer to the solution.

Hosting of Various Classes of Hydrocarbons and Their Mixtures. Having examined the differences between dendrimers of different surface charge, we are now interested in binding between PAMAM dendrimers, using G4-NH_2 as our model, and different hydrocarbons. Amine-terminated dendrimers were chosen because they exhibited the strongest binding with hydrocarbons across the tested temperature range, and therefore allowed the best characterization of the differences between PAMAM binding with different classes of hydrocarbons. As crude oils are composed largely of aliphatic hydrocarbons, it is critical to understand dendrimer interactions with such linear hydrocarbons. However, purely aliphatic hydrocarbons are difficult to track quantitatively in solution. To overcome this difficulty, we doped solutions of hexadecane with octadecylbenzene (ODB, 2.5 w/w%), which is an 18-carbon chain with the addition of a benzene ring on one end. The result is a solution with minimal change from a purely aliphatic hydrocarbon mixture but which can be monitored in real time in solution using spectrofluorescence measurements (Fig. 2.3). We characterized the excitation and emission of ODB-doped C_{16} in various conditions: dissolved in 100% methanol, suspended as an oil-in-water emulsion in DI water, and in a DI solution of 15 μM G4-NH_2 dendrimers (Fig. 2.3a). We note that the emission peak redshifts from 281 to 290 nm when suspended in water compared to in methanol, which we attribute to an increased polarity of the fluorophore environment. The ODB emission further redshifts to 299 nm

upon incubation with dendrimers, indicating that a significant fraction of ODB molecules interacted directly with G4-NH_2 rather than simply being suspended in smaller droplets of C_{16}. We measured the kinetics of this fluorescence over time, monitoring ODB emissions at 290 and 299 nm for pure water and dendrimer solution samples, respectively (Fig. 2.3b). While the ODB fluorescence in water and with dendrimers began with nearly identical intensity, there was a marked initial decrease in water-suspended intensity, a loss of approximately 30%. This indicates that many of the emulsion droplets in the water suspensions quickly coalesced before the final stable emulsion was achieved. Even after this relatively stable emulsion was formed, there is a slow (1.4%/h) continued coalescence and a resulting phase separation of the oil-in-water emulsion. Such coalescence is not seen in the dendrimer solution over the observed time period, confirming that such suspensions are more stable than the oil-in-water emulsions. Based on this fluorescence measurement, the stable suspensions formed with G4-NH_2 at room temperature accommodate 57 ± 4% more ODB-doped C_{16} than the oil-in-water emulsion, highlighting the efficiency of dendrimer as oil dispersants. We also note that the nature of the oil dispersion is different from an oil-in-water emulsion (Inset, Fig. 2.3b). The oil-in-water emulsion (left) is cloudy due to light scattering by large oil droplets, while the dendrimer-dispersed oil (right) is clear, indicating the presence of much smaller complexes in agreement with previous results that showed the formation of dispersed C_{16}-dendrimer complexes of approximately 200 nm.[28] This further suggests that nearly all suspended hydrocarbons are dendrimer-associated, since we did not observe any oil-in-

water droplets that would be expected if dendrimers simply added encapsulated hydrocarbons to an oil-in-water emulsion.

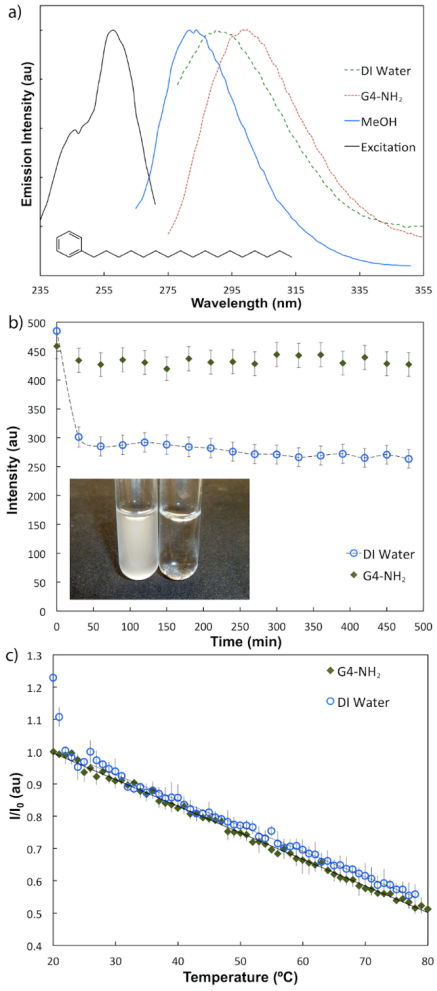

Figure 2.3 The fluorescence excitation and emission spectra (a) of ODB and the kinetics of this fluorescence at room temperature (b). Inset is a photo of pure water and dendrimer solutions incubated with equal quantities of C_{16}+ODB. Oil-in-water emulsions are cloudy suspensions (left); dispersion by dendrimers results in a clear suspension (right). Raising the solution temperature causes thermal quenching with and without dendrimers (c), but no loss of binding to dendrimers at high temperatures. Error bars are standard deviations of 3 independent trials.

We also examined the fluorescence behavior in water and dendrimer suspensions as a function of temperature (Fig. 2.3c), showing normalized fluorescence intensities. Note that the initial drop in water suspension fluorescence intensity is due to the coalescence observed at early times as in Fig. 2.3b, but not due to the increase in temperature. Therefore, normalization for the water curve was performed after this initial drop in intensity. After this point, the water and dendrimer suspensions are statistically identical and both intensities decrease linearly with increasing temperature. This linear decrease in fluorescence intensity with respect to increasing temperature indicates simple thermal quenching as more rotational and vibrational degrees of freedom become accessible, which is different from the molecular quenching observed between cationic dyes and PAMAM dendrimers with organic moieties.[86] We did not observe any transition as was seen in incubation of pure PN with dendrimers. This is primarily due to the fact that C_{16} has near zero water solubility, therefore eliminating the competition with water solvation seen in the case of PN-dendrimer interactions. Because of this lack of competition, the C_{16}-dendrimer interactions are more stable at high temperatures.

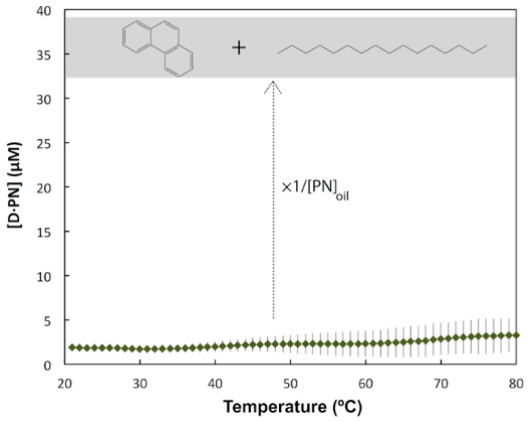

Figure 2.4 The concentration of dendrimer-associated PN (green diamonds) as a function of temperature. Shaded region shows the calculated increase in concentration of hydrocarbons due to dendrimers compared to oil-in water emulsion, including both PN and C_{16}. Error bars are standard deviations of 3 independent trials.

Because crude oil is a combination of aliphatic and aromatic hydrocarbons (among other components), we created a "model crude" by dissolving PN in C_{16} (8% PN) to investigate the interaction between G4-NH_2 dendrimers and hydrocarbon mixtures. By measuring the UV absorbance of PN as described above, the quantity of oil suspended in the water column with and without dendrimers was calculated (Fig. 2.4). In contrast to the trend seen when incubated with pure PN, the dendrimer-associated PN remains approximately constant with temperature across the entire tested temperature range. These results suggest that the aliphatic C_{16} is able to synergistically facilitate stronger, more stable interactions between dendrimers and PN that have little temperature sensitivity. We hypothesize that C_{16} accomplishes this by eliminating the PN partition competition from water solvation, serving as a stronger solvent inside the dendrimer interior for PN. By assuming that the ratio of PN/C_{16} remains constant after interacting

with dendrimers, we calculated the total suspended hydrocarbon concentration. The increase in this total hydrocarbon concentration compared to that in water alone is shown by the shaded area, reaching at least 35 μM hydrocarbon compared to ~10 μM of pure PN (Fig. 2.1a); the total concentration of hydrocarbons with dendrimers in water reached approximately 135 μM. Because of the behavior noted in the ODB-C_{16} study, we expect that virtually all of the suspended PN and C_{16} were directly dendrimer-associated, which indicates a strong hosting capacity of at least 9 hydrocarbons per dendrimer. This capacity for suspending hydrocarbons persisted well beyond environmentally relevant temperatures, and indeed even beyond the dissociation temperature for pure PN to break down hydrophobic interaction and pi stacking.

4. CONCLUSION

In summary, we have shown that aliphatic, aromatic, and hybrid hydrocarbons bind strongly with G4 PAMAM dendrimers at environmentally relevant temperatures. Mixtures of aliphatic and aromatic hydrocarbons in a model crude are synergistically dispersed by PAMAM dendrimers, reaching a highly stable dispersion of at least 9 hydrocarbon molecules per G4 dendrimer over a wide range of temperatures. At environmentally relevant temperatures (*i.e.* less than approximately 32ºC), G4-SA and G4-NH_2 bind much more strongly to hydrocarbons than G4-OH due to this neutral dendrimer collapsing, closing off access to the hydrophobic interior. However, changes in tertiary amine pKa and resulting interior protonation in G4-SA due to the abundance of terminal acidic groups severely limited their hydrocarbon hosting capacities. The

dendrimer oil dispersions were also shown to be significantly more stable and contained 57% more hydrocarbon than simple oil-in-water emulsions. These results demonstrate that, when their versatile physicochemical properties are utilized properly, dendrimers are very robust as oil dispersants; we have also illuminated potentially unanticipated or unintended effects of varying dendrimer surface functionality on hosting applications including dispersion but also drug delivery and water purification that usually deal with hydrophobic or charged ligand species. Future work will include studies examining the effects of pH, ionic strength and ions of different valences in solution.

Mechanisms of dendrimer-small molecules binding

Wang, B. et al. Deviation from the Unimolecular Micelle Paradigm of PAMAM Dendrimers Induced by Strong Interligand Interactions. Journal of Physical Chemistry C, 119, 19475-19484. Reproduced in part with permission from American Chemical Society

1. INTRODUCTION

Dendrimers are a class of synthetic, highly controlled macromolecules with a fractal-like structure. Well-defined branching units emanate from the central core, while the number of branching iterations defines the "generation" of the dendrimer.[87] The central core, interior branching units and terminal units of the dendrimer can be individually chosen, allowing for great design flexibility.[87] As a result, the size, hydrophobicity and surface functionalities of the dendrimer can be tailored for a wide variety of applications. PAMAM (polyamidoamine) dendrimers are one of the most commonly studied dendrimers.[5,10,18,87] At neutral pH the PAMAM dendrimers are comprised of a hydrophobic interior terminated by hydrophilic surface amines, which are protonated under physiological conditions to render a so-called "unimolecular micelle" stucture.[17,88–93] Due to their unique physicochemical properties, PAMAM dendrimers have potential applications impacting many fields. In biomedicine, for example, PAMAM dendrimers can serve as carriers by either linking drug molecules to their surface or encapsulating the drugs inside their interior cavity.[1] For weakly acidic drugs, the main driving forces for noncovalent binding with dendrimers are electrostatic interactions and hydrogen bonding.[5,94,95] For example, generation-four (G4) PAMAM dendrimers with 64 surface amines are able to encapsulate as many as 78 ibuprofen

molecules.[96] PAMAM dendrimers have also been used to encapsulate and deliver small hydrophobic pharmaceutical molecules for enhanced water solubility and biodistribution.[5] Solvent conditions such as polarity, ionic strength, and pH affect the conformation of PAMAM dendrimers[97,98] and thus their encapsulation efficiency, as the dendrimer maximum loading capacity is directly related to the shape, size, and conformation of the dendrimer.[11,37] However, the density of dendrimer surface groups rapidly increases with generation, which may sterically block guest molecules from partitioning into the dendrimer interior.[11] At generation 7 or higher, the surface groups reach the de Gennes dense packing limit to seal the interior.[5]

In addition to drug delivery, the hosting capability of dendrimers can also be utilized in environmental applications such as water purification, desalination, and pollution remediation.[99–101] Commercially available oil dispersants including Corexit have been in use for treating oil spills worldwide.[102,103] However, the potential toxicity of oil dispersants has recently become a great concern, particularly after their large-scale deployment in the 2010 Deepwater Horizon Spill.[103–106] It is therefore imperative to identify an alternative oil dispersant with high biocompatibility while still maintaining a relatively high efficiency. We have previously proposed and verified in lab-scale studies that cationic PAMAM dendrimers can act as efficient oil dispersants[99] for both polyaromatic and linear hydrocarbons, two key components of crude oil. In our previous experiment, linear hexadecane (C16) and polyaromatic phenanthrene (PN) were used as model hydrocarbons, both of which were hydrophobic while their size difference was negligible relative to that of a G4-PAMAM dendrimer. When the model hydrocarbons

were associated with the dendrimers in water, the average hydrodynamic sizes of the aggregates were significantly different: 200 nm for G4-C16 and 9 nm for G4-PHe complexes, respectively, indicating that PAMAM dendrimers dispersed linear and aromatic hydrocarbon through drastically different mechanisms.[99] Specifically, the hydrodynamic radius of G4-PHe was comparable to that of G4 dendrimer[99], suggesting a single PAMAM dendrimer encapsulating multiple PN molecules while retaining a unimolecular micelle structure. In contrast, the size of G4-C16 was two orders of magnitude larger than that of a single G4-PAMAM, indicating that a large multiple-molecular complex was formed. It was hypothesized that when a linear C16 molecule was encapsulated there remained one end protruding out of the G4 molecule.[99] This enabled bridging with surrounding G4 molecules to create the complexes.[99] However, the experimental data were insufficient to clearly validate the hypothesis, so the structure of these supramolecular complexes and the mechanism for such clear deviation from PAMAM acting as a unimolecular micelle in ligand encapsulation remains unknown.

There have been numerous studies including both experiments and computations on the mechanisms of dendrimers encapsulating single target molecules.[1,5,10] Electrostatic interactions, hydrophobic effects, or hydrogen bonding typically account for the formation of host-guest structures.[5,94–96] Almost ubiquitously, the structures are described as dendrimer hosts with molecular guests forming unimolecullar micelles that do not bind with surrounding micelles; however, as mentioned above, experimental evidence with PAMAM dendrimers and C16 suggest that the formation of supramolecular complex containing multiple dendrimers and ligands could occur.[20]

To elucidate the molecular mechanisms of dendrimers as dispersants, computational modeling has been applied to bridge the gap between experimental observations and actual molecular systems.[37] Due to computational limitations, interactions of ligands with a single dendrimers were usually modeled previously. Recently, in the absence of ligands inter-molecular interaction between two PAMAM dendrimers has been studied using umbrella sampling molecular dynamics (MD), where effective repulsion between cationic PAMAM and weak attraction between neutrally-charged PAMAM were found.[107] We hypothesize that, in addition to the dendrimer-ligand interactions, ligand-ligand interactions are important to overcome the repulsion between cationic PAMAM dendrimers in forming the supramolecular complexes observed experimentally.[99] Hence, in order to fully understand the mechanisms governing dendrimer's function as an oil dispersant as well as a host for catalysts and drug molecules, it is necessary to examine both dendrimer-ligand and ligand-ligand interactions.

Here, we applied atomistic discrete molecular dynamics (DMD) simulations to study the dispersion mechanisms of G4-PAMAM dendrimers with C16 and PN. DMD is a special type of molecular dynamics algorithm, which features rapid sampling efficiency, and has been recently shown to recapitulate the structures and dynamics of PAMAM dendrimers of different generations, surface groups, and pH conditions.[37] We systematically studied the binding of a single PAMAM dendrimer with single and multiple ligands, as well as two PAMAM dendrimers interacting with multiple ligands. From DMD simulations, we found that both C16 and PN displayed a high cooperativity

in binding dendrimers. Difference in structural, dynamic and energetic properties between these two types of hydrocarbons led to drastically different clustering behaviors in the absence and presence of dendrimers. Compared to the rigid PN molecule, strong inter-ligand interaction between the flexible C16 resulted in weaker solubility, i.e. the association and condensation of the ligands in water. We found that the same physicochemical properties also led to the formation of multi-dendrimer micelles in the presence of PAMAM dendrimers, thereby revising the unimolecular micelle paradigm of PAMAM dendrimer as a host agent. As drug molecules usually possess hydrophobic and aromatic moieties the results of this study may be extended beyond the scope of environmental remediation to studies of dendrimers for drug delivery, catalysis and biosensing.

2. EXPERIMENTAL AND COMPUTATIONAL METHODS

2.1 Discrete molecular dynamics simulation. Discrete molecular dynamics (DMD) is a special type of molecular dynamics algorithm where inter-atomic interactions are modeled by square-well potential functions instead of continuous potentials. A more detailed description of the DMD algorithm can be found elsewhere.[41,46] DMD has been proved to be a powerful method in simulating biomacromolecules such as proteins.[47,108,109] Recently, we have successfully applied DMD in simulating dendrimers with various structures.[37] We used a united-atom representation for the dendrimer-hydrocarbon systems in which all heavy atoms and polar hydrogens were explicitly modeled. Inter-atomic interactions including van der Waals (VDW), solvation,

electrostatic and hydrogen bond interactions were modeled by a physical force field adapted from Medusa.[45,110] Bond length, angle and dihedrals were taken from CHARMM 19.[78] The solvation energy was included using the Lazaridis-Karplus implicit solvent model, EEF1.[79] The distance and angular dependent hydrogen bond interaction was modeled using a reaction-like algorithm.[45] We used the Debye-Hückel approximation to model the screened electrostatic interactions between charged atoms. The Debye length was approximately 1 nm by assuming water relative permittivity of 80, and a monovalent electrolyte concentration of 0.1 M.

The periodic boundary condition was used in DMD simulations. We adopted the Anderson's thermostat to perform constant temperature simulations. In DMD simulations, the temperature has the unit of kcal/(mol•k_B), where k_B is the Boltzmann constant. Our simulations were conducted across a temperature range of 0.50 − 0.80 kcal/(mol•k_B), corresponding to 250 − 400 K with a scaling factor of ~500. We note that our implicit solvent approach could not capture the temperature-dependence of the hydrophobic interactions mediated by water molecules. On the other hand, we expect that the extrapolated enthalpy and entropy values from DMD simulations at a wide range of temperatures were good approximations near the room temperature where the parameters of implicit solvent model were tabulated.[79] At each temperature, energy minimization was first carried out for 1,000 time steps (approximately 0.05 ns).

2.2 PAMAM dendrimer model. Generation-four poly(amidoamine) (PAMAM) dendrimers are highly positively charged polymers comprised of a central core, branching

units and 64 amine surface groups. To emulate a solution pH of 8.2, all the amine groups of dendrimers are fully protonated while all interior amine groups remained deprotonated. Due to the high number charges of PAMAM dendrimer molecules, the local salt concentration near PAMAM is higher than that of the bulk and consequently the screening effect near the surface is stronger than the bulk. It has been suggested[111] that in highly charged systems Debye-Hückel approximation with neutralizing counterions can be used to account for the increased screening effect. Therefore, the net charges of the molecular systems were maintained at zero by adding offsetting counterions (Cl-). We computed the radial density distribution of charged atoms, including Cl^- ions and primary amines (-NH3+) (Fig. B2). We found that the counterions (Cl-) indeed mostly stayed near the protonated primary amines as expected. In each simulation, energy minimization was first performed, followed by further equilibration. In equilibrium simulations, simulations with two dendrimers were carried out through 0.5 million time steps (~ 25 ns) while all others were carried out for 1 million steps (~ 50 ns), all of which corresponded to an average of approximately 72 CPU hours.

2.3 Simulations of one dendrimer with one ligand system. For each type of ligand, we performed DMD simulations at different temperatures (from 250K to 400K). At each temperature, we performed twenty independent simulations with different initial configurations, where hydrocarbons were positioned with random orientations and distances to the dendrimer.

2.4 Umbrella sampling of one dendrimer with one C16. The inter-molecular distance between a central carbon of the PAMAM core and the center atom of C16 (i.e., the 8th carbon), r_C, was chosen as the reaction coordinate. We performed ten replicas of DMD simulations, each of which had an infinite square-well bias potential as the function of r_C. The upper and lower bounds of the biased potentials were assigned to overlap with each other: {0, 10.5}, {9.5, 14.5}, {13.5, 18.5}, {17.5, 22.5}, {21.5, 26.5}, {25.5, 30.5}, {29.5, 34.5}, {33.5, 38.5}, {37.5, 42.5}, and {41.5, 137.5} Å. The first and last bias potentials had wider ranges because the ligand were either completely bound or unbound, correspondingly. All simulations were carried out for 1 million steps (~ 50 ns) at T=300K. We utilized 5,000 snapshots evenly distributed throughout the final 25 ns of the simulations to compute the inter-molecular distances, r_C. The weighted histogram analysis method (WHAM)[112] was applied to estimate the one-dimensional (1D) potential of mean force (PMF) with respect to the inter-molecular distance r_C.

2.5 Simulations of one dendrimer with twenty ligands. Twenty ligands (20 C16 or 20 PN) were first assigned with random orientations and distances to the dendrimer. Then we let the system run at the lowest simulation temperature (T=250K) until equilibrium was reached (2 million steps, approximately 100 ns). At this temperature, all ligands were eventually encapsulated by the dendrimer. Then, we chose snapshots of the equilibrium states as our starting state for the dissociation simulations. The dissociation simulations (as well as all the following simulations) were performed at the same temperature range

(250K to 400K). At each temperature, we performed ten independent simulations with different initial velocities assigned according to the Maxwell-Boltzmann distribution.

2.6 Simulations of hydrocarbons clusters. We followed the same protocol as above where 20, 40, 60 or 80 ligands (C16 or PN) were first assigned with random orientations and distances to each other. Then we let the system run at T=250K until equilibrium was reached (1 million steps, approximately 50 ns). Those hydrophobic ligands assembled quickly to become a single cluster. Ten snapshots of hydrocarbons clusters along the association simulations were chosen as the initial structures for the dissociation simulations.

2.7 Preparation of the two dendrimers binding with eighty ligands. Two dendrimers were first positioned away from the 80 ligands cluster (obtained from the previous simulation). Then we let the system run at T=300K for 0.5 million steps, approximately 25 ns. Two dendrimers were bound to the cluster eventually. To initialize the structures for the following dissociation process, we repeated the above approaching process at lower temperature (T=250K) and ten final snapshots of the simulation were chosen separately so that simulations could start from ten different configurations. The dissociation processes were performed for another 0.5 million steps until an equilibrium of the system was reached.

2.8 Contact definition and the clustering analysis. A contact between two molecules was defined when at least one pair of heavy atoms from each molecule is within 5.0 Å. We used the single-linkage criterion to define a molecular cluster, where a molecule belonged to an existing cluster if it made any contacts with members of the cluster. The size of a cluster is defined as the number of member molecules. The mean and standard deviation of contacts and cluster size at each temperature were obtained from system snapshots in equilibrium. In the case of two G4-NH2 dendrimers with multiple hydrocarbons, we collected 1,000 snapshots evenly distributed along the final 5 ns of the simulations. In all other simulations, we utilized 5,000 snapshots evenly distributed throughout the final 25 ns of the simulations.

2.9 Structural analysis of PAMAM dendrimer. We used two structural parameters to capture the structure information of dendrimer, including radius of gyration, *Rg*, to quantifies dendrimer size, and ellipticity, e, to quantify the shape of dendrimer. Both *Rg* and ellipticity can be obtained from the momentum of inertia tensor, *I* (diazotization of 3x3 matrix results into three eigen-values, $I_x < I_y < I_z$):

$$Rg = \sqrt{(I_x + I_y + I_z)/m}\,, \qquad (1)$$

and

$$e = \sqrt{1 - (I_x / I_z)}\,. \qquad (2)$$

Here, *m* is the total mass of the dendrimer.

3. RESULTS AND DISCUSSION

We used united-atom representations to model both PAMAM and hydrocarbon molecules in our atomistic DMD study (Methods). We modeled inter-atomic interactions with van der Waals, solvation, electrostatic, and hydrogen bonds. We used the EEF1 implicit solvent model[113] in CHARMM[79] to estimate the solvation energy. To ensure sufficient sampling, multiple independent DMD simulations for each molecular system – e.g. one ligand with one dendrimer, multiple ligands with one dendrimer, multiple ligands with multiple dendrimers, as well as multiple ligands alone in solution – were performed with different initial conditions.

Aromatic PN has a stronger binding to a single G4 PAMAM dendrimer than linear C16. We first studied the simple case of a single cationic G4 PAMAM dendrimer interacting with a single hydrocarbon, including C16 and PN. For each type of ligand, we performed DMD simulations at different temperatures to study the binding thermodynamics. At each temperature, we performed twenty independent simulations with different initial configurations, where hydrocarbons were positioned with random orientations and distances to the dendrimer and each simulation lasted 50 ns (Methods). In DMD simulations, a ligand was able to bind the dendrimer after random diffusion (Fig. 2.5A). Because of the small size of a single ligand, the energy difference between the bound and unbound state was small compared to fluctuations. We computed the number of inter-molecular atomic contacts between ligand and dendrimer to characterize their binding (Fig. 2.5B). The two molecules were counted as bound if they made any inter-molecular contacts between heavy atoms. For each type of hydrocarbon ligand, we

calculated its binding probability, $P_{bind,}$ to the dendrimer as a function of temperature (Fig. 2.5C). We used the final 25 ns of each simulation and calculated the averages and standard deviations over twenty replicates. At low temperatures, the hydrocarbons stayed bound with P_{bind}~1 and the ligands were encapsulated inside the dendrimer. As temperature increased, P_{bind} decreased due to thermal fluctuations. Assuming a canonical ensemble with the bound and unbound states, we can estimate the binding free energy, $\Delta G_{bind} = -K_B T \ln P_{bind} /(1- P_{bind})$. For each temperature, we obtained the ΔG_{bind} of C16 and PN (Fig. 2.5D). To verify our above approach of ΔG_{bind} estimation, we performed umbrella sampling to study the binding of a C16 with a single dendrimer at T = 300 K (Methods). We estimated the PMF as a function of the inter-molecular distance, *r*, using WHAM[112] (Fig. B3). The 1D PMF had two minima, the one with a shorter *r* corresponding to the bound state and the other corresponding to the unbound state. The PMF barrier related to the dissociation between C16 and the G4 PAMAM dendrimer was smaller compared to previous computational results between polar drugs and a G5 PAMAM dendrimer, where the binding was governed by strong inter-molecular hydrogen bond and electrostatic interactions.[114] A lower density of amidoamine monomers in a G4 PAMAM than a G5 dendrimer may also contribute to the smaller PMF barrier. The binding free energy, estimated as the PMF difference between two minima was ~ -1.56 kcal/mol, in agreement with the estimation from our unbiased simulations ~ -1.19±0.52 kcal/mol. The discrepancy was due to the fact that the actual binding free energy corresponds to the integral of the 1D PMF:

$$k_B T \ln \int_{d^*}^{\infty} \exp[-\beta PMF(r)]dr - k_B T \ln \int_{0}^{d^*} \exp[-\beta PMF(r)]dr \,, \qquad (3)$$

where distance $d^{\neq}$ corresponds to the free energy barrier separating bound and unbound states in the PMF plot, and β denotes $1/k_BT$ (Fig. B3). Since the unbound basin was wider compared to the bound basin, the difference of PMF between bound and unbound basins was an over estimation. Therefore, the comparison with umbrella sampling validated our approach to estimate ΔG_{bind} from unbiased DMD simulations.

The estimated ΔG_{bind} has linear temperature dependence for a wide range of temperatures in simulations and the deviation at low temperatures is probably due to the insufficient sampling of binding/unbinding events. Based on the temperature dependence of binding free energy, we can estimate the changes of enthalpy (ΔH) and entropy (ΔS) associated with ligand-PAMAM binding, $\Delta G_{bind} = \Delta H - T\Delta S$. Using linear regression, we estimated ΔH and ΔS for both single C16 and PN binding to a single PAMAM (Table 2.3). Compare to C16, PN had a stronger gain of enthalpy but also a higher loss of entropy upon binding PAMAM. A higher ΔH for PN was due to its planar, aromatic structure, which had stronger van der Waals interactions with the PAMAM dendrimer than the linear C16. Also because of the rigid planar geometry of PN, binding with PAMAM had a stronger confinement effect than the flexible C16, which resulted in a higher entropy loss ΔS for PN upon binding with PAMAM.

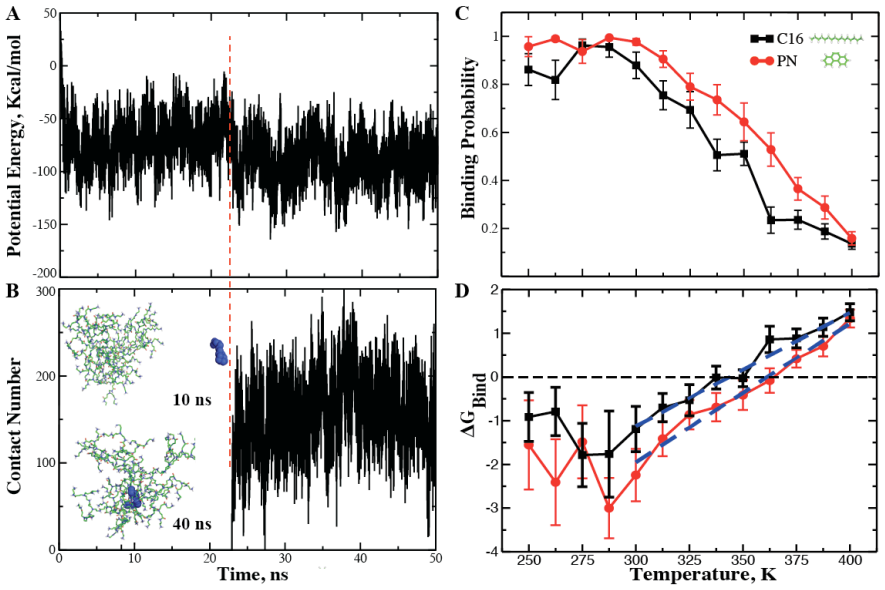

Figure 2.5 Binding simulations of one hydrocarbon ligand interacting with a single dendrimer. (A) The total potential energy and (B) the number of inter-molecular contacts were plotted as functions of simulation time from a typical DMD simulation of one dendrimer interacting with one C16 ligand at T = 300 K. Two snapshots at 10 ns and 40 ns were shown as the insets in panel B. The vertical dashed line corresponds to the time when two molecules bound to each other. (C) The binding probabilities, P_{bind}, of C16 and PHe with dendrimer were computed as functions of temperature. (D) The binding free energy, ΔG_{bind} of C16 and PN with dendrimer were estimated using P_{bind}. The blue dashed lines in (D) correspond to linear fits from T=300K to T=400K. The slope and intercept of the fitting line correspond to ΔS and ΔH, respectively.

Table 2.3 Enthalpy and entropy changes for various dendrimer-ligand systems. The values were obtained by fitting ΔG_{bind} as a function of temperature (standard error of linear regression in bracket). The fitting temperature range was from 300K to 400K except the case of C16 × 20 (from 350K).

Ligands		ΔH, kcal/mol	ΔS, kcal/(mol*Kelvin)
x1	C16	-9.08 (0.61)	-0.0265 (0.0017)
	PN	-11.48 (0.67)	-0.0317 (0.0019)
x20	C16	-14.85 (3.61)	-0.0326 (0.0096)
	PN	-11.47(0.51)	-0.0306 (0.0014)

C16 has a higher binding cooperativity to a PAMAM dendrimer than PN. To evaluate the effect of inter-ligand interactions on hydrocarbons binding to a dendrimer, which arises from a large number of ligands encapsulated within a dendrimer, we performed DMD simulations of twenty C16 or PN molecules interacting with one dendrimer. As in the above single hydrocarbon study, we were interested in the average binding probability P_{bind} of each ligand. In principle, if equilibrium is reached in DMD simulations, the calculated P_{bind} should be independent of the initial condition, e.g. all hydrocarbon ligands initially positioned outside or encapsulated inside the dendrimer. As a simple test, we performed control association simulations starting with all C16 outside of the dendrimer and found that the results were consistent with the dissociation simulations starting from all ligands encapsulated by the dendrimer, with the only difference being the association simulations took more time to reach equilibrium in the former configuration (Fig. 2.6A). Therefore, in each molecular system, we initially placed all hydrocarbons encapsulated inside the dendrimer and performed DMD simulations to equilibrate the system. At each temperature, we computed the average number of ligands bound to the dendrimer (Fig. 2.6B). We noted that the number of bound ligands per PAMAM in DMD simulations was higher than that reported in previous experiments.[37] The difference between simulations and experiments is possibly because of the fact that temperatures in simulations cannot exactly correspond to the experimental temperatures and that the experimental value was estimated as a lower limit. We computed the average binding probability P_{bind} as a function of temperature by normalizing with the total number of ligands added to the system (Fig. B1). Compared to

the results of a single ligand binding to the dendrimer, the increased binding probablitiy, P_{bound}, implied a cooperative effect for both C16 and PN. Following the same strategy of single ligand binding, we calculated the effective binding free energy ΔG_{bind} for each ligand (Fig. 2.6C). We also estimated ΔS and ΔH (Table.2.3). In the case of PN, ΔH and ΔS remained approximately identical for single and multiple ligands, but the interactions among the PN ligands did decrease the system energy leading to a slightly stronger ΔG_{bind} over a wide range of temperatures, suggesting a weak cooperativity. When the system had multiple C16 molecules, cooperative binding was so strong that we only observed partially dissociations at high temperatures (Fig. 2.6). Fitted with only a few temperature points, the estimated ΔH and ΔS featured larger standard errors than other cases. Nevertheless, compared to single C16, we observed a significant increase in enthalpy gain ΔH for multiple ligand binding, while changes in ΔS are within error bars. The significant decrease in ΔG_{bind} for multiple C16 binding suggests a strong binding cooperativity. Such cooperativity can be explained by the increased hydrophobicity of the dendrimer core after binding to hydrocarbons, which in turn effectively enhanced the binding of additional hydrophobic ligands (Figs. 2.6D and E).

Taken together, although PN showed higher binding affinity than C16 in the case of a single dendrimer interacting with one ligand, as more ligands were added to the simulation system the relative binding strength of those two ligands reversed (Fig. 2.6C,D). For PN, the binding free energy ΔG_{bind} as well as ΔH and ΔS were strikingly similar in both the one and multiple ligand binding simulations. But for C16, ΔG_{bind} and

ΔH were significantly increased in the case of multiple ligand binding. So, what was the origin for the much stronger binding cooperativity of C16 than PN (Fig. 2.6)?

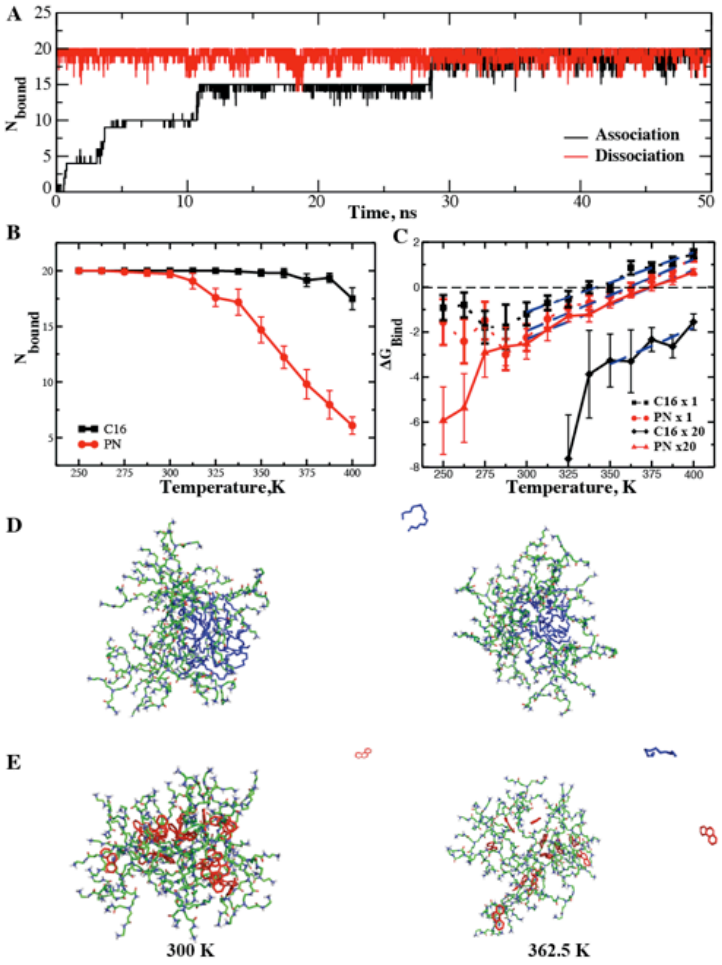

Figure 2.6 Simulations of twenty hydrocarbons interacting with a single dendrimer. (A) The number of C16 ligands bound to the dendrimer, N_{bound}, as the function of simulation time was computed from both association (black line) and dissociation (red) simulations at T = 300 K. It took approximately 30 ns for the association process to reach equilibrium. (B) Averaged over independent simulations at each temperature, the average N_{bound} was computed for both C16 and PHe. (C) The binding free energy change per ligand, ΔG_{bind}, was computed from the normalized binding probability (Fig. B1). For comparison, ΔG_{bind} for single hydrocarbon binding simulations was also included. The blue dashed lines correspond to linear fits from T=300K to T=400K (except for C16×20 simulations which started from T=350K). Snapshot structures at T = 300 and 362.5 K were taken from DMD simulations for both C16 (D) and PN (E).

C16 features strong inter-ligand interaction. We next determined whether the cooperativity of hydrocarbons encapsulated by a dendrimer was due to the intrinsic physicochemical properties of each hydrocarbon species. For both C16 and PN, we performed DMD simulations to evaluate the association dynamics of ligands alone. As described above, we performed dissociation studies in DMD simulations where we generated hydrocarbon clusters with different sizes (i.e., comprising 20, 40, 60, and 80 C16 or PN molecules) as initial states and observed the dynamics of dissociation at different temperatures (Methods). At low temperatures, the initial clusters were stable during the course of the simulations. As temperature increased, the size of initial clusters shrank by releasing surface hydrocarbons due to thermal fluctuations. Therefore, we computed the average size of the largest cluster in simulations as a function of temperature (Fig. 2.7A). A hydrocarbon ligand with stronger inter-ligand interaction is expected to have greater thermo-stability, preserving its initial cluster. We found that the size of C16 clusters did not change significantly within the range of simulated temperatures. In contrast, PN clusters were less stable and all sizes of the simulated clusters broke into many smaller clusters at high temperatures. Since our simulations modeled the association of hydrocarbons in water implicitly, our results are consistent with the observation that PN has higher solubility in water than that of C16.[37]

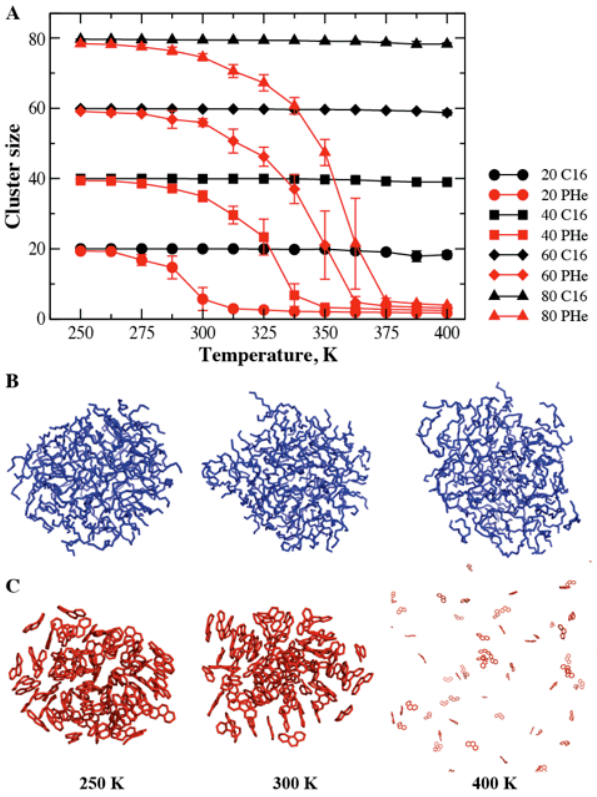

Figure 2.7 Thermostability of hydrocarbon clusters. (A) The size of hydrocarbon clusters as a function of simulation temperature. For both C16 and PHe, DMD simulations of hydrocarbon clusters with initial sizes of 20, 40, 60 and 80 ligands were performed at different temperatures. The number of ligands in the largest cluster was calculated to quantify the corresponding thermo-stability. Snapshots structures at temperatures T = 250, 300, and 400K were taken from DMD simulations for both C16 (B) and PN (C). The systems were in equilibrium at each sampling temperature.

The linear C16 molecule is flexible, while the planar aromatic PN molecule is rigid. Examination of the snapshots at different temperatures (Fig. 2.7B) revealed that C16 molecules in its clusters were mostly unstructured and thus C16 clusters were liquid-like. On the other hand, PN had a preferred aggregation orientation, i.e. pi-pi stacking due to their planar aromatic structure. Compared to the solid-like PN clusters, the higher entropy of C16 clusters contributed to their higher thermostability. Taken together, C16

featured stronger inter-ligand interactions than PHe, which resulted in their higher binding cooperativity to PAMAM.

Strong inter-ligand interactions give rise to the deviation from the unimolecular micelle paradigm of PAMAM dendrimer. To test whether strong inter-ligand and ligand-PAMAM interactions were able to overcome the repulsion between cationic PAMAM to form large molecular complexes, we next modeled the binding of multiple hydrocarbons interacting with two G4 dendrimers simultaneously. We first generated a large hydrocarbon cluster, consisting of 80 C16 (or PN) to mimic an oil droplet. Two dendrimers were initially positioned away from the oil droplet. From above discussion, we noted that the 80 hydrocarbon system was quite stable below T=300K. We performed association simulations at T=300K. We monitored both *Rg* and ellipticity (Methods) to characterize the dynamic properties of dendrimers (Fig. 2.8A.B). As a control, we performed DMD simulates of G4 PAMAM dendrimer alone at the same temperature and computed *Rg* and ellipticity (see Table B1 where we also compared our results by comparing them to the previous experimental and computational studies). The decrease of center-of-mass (CM) distances between the oil droplet and the dendrimer indicated the association. Compared to isolated PAMAM alone, binding with the hydrocarbon droplet resulted in increased *Rg* due to conformational changes of the soft polymer nanoparticle. The final CM distance was smaller for PN (15 Å) compared to C16 (20 Å) because of relatively smaller size of the PN droplet. The size difference of droplet can also lead to differences in *Rg* and ellipicity of dendrimers upon droplet binding. When attached to a

larger droplet like C16, dendrimers tended to undergo a larger conformational change in order to maximize their contact with the droplet, losing structural symmetry in the process with overall larger ellipticity.

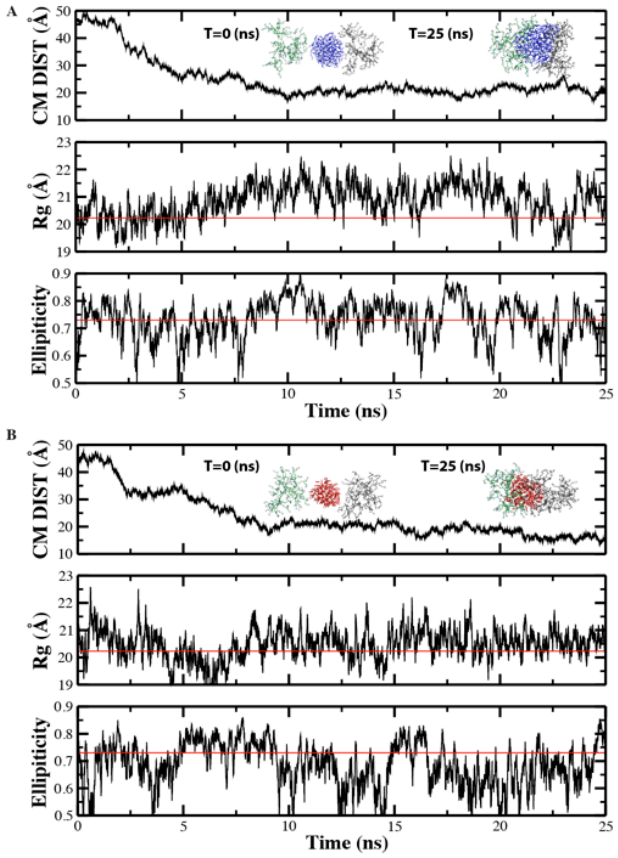

Figure 2.8 Association simulations of droplet binding with two dendrimers. CM distance, radii of gyration and ellipiticity of (A) Dendrimer-C16 (B) Dendrimer-PN association. The red lines denote corresponding values of G4-PAMAM dendrimer alone. Snapshot structures at the beginning (0 ns) and ending (25 ns) are shown as inset.

Starting from the complex structures, we performed dissociation simulations at different temperatures (Methods). We computed the number of hydrocarbon ligands, N_L,

each dendrimer encapsulated (or was in contact with) at equilibrium as a function of temperature (Fig. 2.9A). N_L corresponded to 80 if both dendrimers bound to the initial cluster (e.g. inset snapshot at T=250K in Fig. 2.9A). The number drastically reduced if the two dendrimers did not bind to the same cluster, reflecting the average of cluster sizes bound to each dendrimer. For C16, we can see the N_L value was approximately 80 across the entire temperature range, suggesting that both dendrimers were bound to the initial hydrocarbon cluster without observed dissociation. The branching units of dendrimers formed multiple hydrophobic interactions with the cluster, rendering the binding very robust. In contrast, we observed a completely different behavior for the PN cluster interacting with two dendrimers. As the temperature increased, the average loading for each dendrimer decreased. Base on snapshot structure (e.g. T=250K, 270K), we noted that the cluster became thinner with increasing temperature and eventually split (T=300K). At temperatures higher than 300K, the average N_L became approximately a half of the initial cluster size, ~ 40, suggesting an initial dissociation of the two dendrimers with additional loss of PN molecules occurring with increasing temperature. As observed in previous simulations (Fig. 2.6E), the PN were partially dispersed inside the dendrimer rather than as the stable clusters observed with C16. Therefore, our results suggest that the supramolecular complexes formed in the experimental study[99] of C16 dispersion by PAMAM resembled a multi-molecular micelle structure, where the hydrocarbons in the core were stabilized by multiple dendrimers binding in periphery. Such a multi-molecular micelle structure of PAMAM was mainly the result of strong

inter-ligand interactions instead of ligand-dendrimer interactions (e.g., PN featured a stronger ligand-dendrimer interaction than C16).

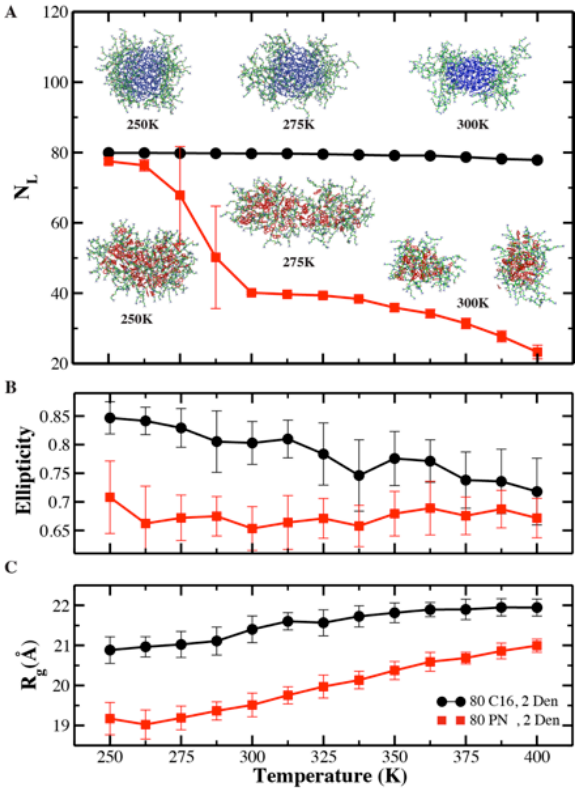

Figure 2.9 Simulations of multiple hydrocarbons interacting with two dendrimers. (A) The number of hydrocarbon ligands, N_L, each dendrimer encapsulated (or was in contact with) as a function of temperature. The snapshot structures in the inset were taken from DMD simulations at T = 250, 275, and 300K for both C16 and PN. (B) Ellipiticity and (C) Radius of gyration illustrated the contrasting structures of PAMAM while binding to C16 and PN. The systems were in equilibrium at each sampling temperature.

The ellipiticity (Fig. 2.9B) and *Rg* (Fig. 2.9C) have also been computed to quantify the structural deviation of dendrimers binding to various ligands. In the case of C16, dendrimers bound to the cluster periphery and displayed notably larger *Rg* and ellipiticity values compared to PN. As temperature increased, higher thermal fluctuations

resulted in increased *Rg* and symmetry (i.e. reduced ellipticity). As for PN, ligands were partitioned inside the dendrimers both in the multi-molecular (at low temperatures) and unimolecular (at high temperatures) states, which resulted in more symmetrical structures with lower ellipticities than simulations with C16.

4. CONCLUSION

We applied DMD simulations to examine the molecular mechanisms of dendrimers as oil dispersants using two representative hydrocarbons, C16 and PHe. Our previous experimental study indicated that G4 PAMAM dendrimers dispersed linear and aromatic hydrocarbons quite differently, as evidenced in measurements of hydrodynamic size,[99] loading capacity, and stability[37] of the resulting complexes formed between the dendrimer and the hydrocarbons. Based on simulations of single dendrimers interacting with single and multiple hydrocarbons, we revealed a cooperativity in both C16 and PN dispersion by dendrimers. Such cooperativity arose from the increased hydrophobicity of the PAMAM interior upon ligand binding, which in turn facilitated binding of additional ligands. Such a cooperative binding of polyaromatic naphthalene with PAMAM has also been observed in recent all atom MD simulations with explicit solvent.[29] Although PN displayed a stronger binding to PAMAM than C16, stronger inter-ligand interactions led to a higher binding cooperativity for C16 to PAMAM than PHe. Our simulations of multiple hydrocarbons interacting with each other suggest that the same strong inter-ligand interaction between C16 molecules also attributes to their lower solubility than PHe. In actual applications of PAMAM as dispersants, the targeted ligands are usually

mixtures of different types of ligands. For example, in our previous experiments,[37] the mixture of C16 with 8% PN ligands was used as a "model crude", which displayed a higher binding cooperativity than PHe. Although we did not model the mixture of C16 and PN in the current study, we expect that C16 will be a "good" solvent for PN and PAMAM can disperse the hydrocarbon mixtures in the same manner as C16 alone.

Based on the traditional unimolecular micelle paradigm of PAMAM dendrimer, the binding of ligands is saturated once the dendrimer core is filled up and the maximum loading is reached. The unusually large size of molecular complexes formed by PAMAM dendrimers when dispersing C16 suggested a deviation from such an accepted scheme of PAMAM. By further simulating two dendrimers interacting with multiple hydrocarbons we found that C16 and G4 dendrimers formed a highly stable micelle structure across the simulated temperature range (275–400K), in which a small C16 cluster was stabilized by multiple dendrimers on the periphery; the system of PN and dendrimers, however, consisted primarily of multiple PN molecules dispersed in the interior of single dendrimers. These results not only explain the phenomena observed in our earlier experimental studies[37,99] but also illuminate the contrasting mechanisms of dendritic polymers for oil dispersion, where both ligand-ligand and ligand-dendrimer interactions contribute to conjure the dendrimer hosting capacity. Such dynamic capacity may serve as a basis for a range of dendrimer applications in environmental remediation, water purification, catalysis, and gene and drug delivery.

CHAPTER THREE

DENDRIMERS IN BIOMEDICAL APPLICATIONS

Dendrimers as surfactants

*Wang, B. et al. Thermostability and reversibility of silver nanoparticle-protein binding. Phys. Chem. Chem. Phys., 2015, **17**, 1728. Reproduced in part with permission from Royal Society of Chemistry*

1. INTRODUCTION

Recently, understanding the biological responses to engineered nanomaterials has become an area of research focus, driven by the crucial need of addressing the transformation, function and safety of nanomaterials introduced into living systems through intentional administration or accidental exposure.[115,116] Compared with the rapidly growing literature on the electronic, photonic and catalytic applications of nanomaterials, fundamental interactions involving nanoparticles (NPs) and biomolecular species are less studied and understood, partly due to the myriad and complex nature of such interactions, and partly due to the lack of effective methodologies for capturing atomic- and molecular-level nano-bio interactions.[117] Nonetheless, it is generally recognized that understanding fundamental NP-biomolecular interactions is vital to delineating and predicting the cellular and organism responses to NPs, and is essential for enabling the bottom-up design of nanobiotechnology and nanomedicine.[118]

Proteins are a major class of macromolecules that carry out all biological functions *in vivo*. Upon exposure to NPs, the adsorption of proteins, nucleic acids, ions and lipids gives rise to a generic NP-protein "corona".[118,119] On one hand, the formation

of the NP-protein corona reflects the thermodynamic nature of NP-biomolecular interactions towards a minimized surface energy of the NPs in a biological milieu. On the other hand, the protein corona shields the physicochemical properties of the NPs to elicit their biological identity.[118] Collectively, the combined NP-protein corona entity is believed to play a central role in determining the transformation, fate and toxicity of NPs in biological systems.

The formation, dynamics and biological identity of the protein corona has been studied intensively in recent years.[49,119–126] Specifically, the adsorption of the protein corona has been shown highly dependent on the physicochemical properties of the NPs (size, shape, surface coating, charge, hydrophobicity and chemical composition), the structure of the proteins and the composition of the biological medium.[118–120] The residence time of the proteins on the NP surface varies according to the affinities of the protein species for the NPs, as prescribed by the Vroman effect,[127] to give rise to a "soft" or a "hard" corona.[118] Using discrete molecular dynamics (DMD) simulations, we have recently revealed rapid exchanges between the citrate capping agent of a silver nanoparticle (AgNP) and ubiquitin, especially during the onset of the AgNP-ubiqutin corona formation.[49] By adjusting the surface hydroxylation of a fullerene, we have demonstrated the feasibility of a role reversal in rendering a ubiquitin core confined by the NP.[128] Furthermore, corona-free zwitterionic gold NPs have been synthesized by Moyano et al. by tailoring the hydrophobicity of the synthesized NPs, and cell uptake of such covalently functionalized NPs has been shown to depend upon the chemical motifs of the NP surface.[129] With regard to the biological responses to the protein corona,

unfolding of fibrinogen by poly(acrylic acid)-conjugated gold NPs promoted Mac-1 receptor activation and inflammation,[123] while transferrin-functionalized SiO_2 NPs displayed a compromised *in vitro* targeting capability as a result of the corona formation.[122] Despite these efforts, however, the thermodynamics[130,131] and reversibility of NP-protein interactions, two important aspects which underlie the transformation, function and toxicity of NPs in biological systems, have been little studied and hence constitute the motivation of the present work.

The two protein species used in this study are hen egg-white lysozyme and bovine milk alpha lactalbumin (ALact). Lysozyme (129 residues, 41% helical and 9% beta sheets) and ALact (120 residues, 41% helical and 9% beta sheets) are viewed as homologs due to their strong resemblance in molecular weight and percentage distribution of secondary structures. However, these two classes of proteins possess entirely opposite net charges. Functionally, lysozyme is responsible for the breakage of peptidoglycans in bacterial cell wall, while the globular metalloprotein of ALact is present in the milk of all mammals serving as a regulator for lactose biosynthesis. Lysozyme and ALact are selected as model proteins in this study because of their biological abundance and contrasting physicochemical properties, including their similarities in molecular weight and globular size, but disparity in sequence and charge.

AgNPs represent a major class of nanomaterials that are produced in large quantities by commercial sources and research laboratories, taking advantage of their antibacterial property[132,133] and their superb capacity in inducing surface plasmon resonance for biological and chemical sensing and DNA hybridization. The synthesis as

well as storage of AgNPs usually involves the use of citrate, polyvinylpyrrolidone (PVP) and, more recently, branched polyethyleneimine (bPEI) polymers,[134] that are adsorbed onto the NP surface through van der Waals (VDW) and electrostatic forces to render water solubility and steric separations to the NPs. Due to the increasing application of bPEI-coated AgNPs (bAgNPs in short) and paucity of information on the transformation and behavior of bAgNPs within the biological context,[135] we examined the thermodynamic interactions between bAgNPs and the protein species of lysozyme and ALact. We further evaluated the effects of these physical interactions on the structural stability of the proteins.

This paper is organized as follows: the surface charges of lysozyme, ALact and bAgNPs are first determined and the formation of the NP-protein coronas is visualized by transmission electron microscopy (TEM). As a central component of the study, the hydrodynamic size and stability of the proteins in the presence of the NPs are characterized using an automated, high-throughput and temperature-controlled dynamic light scattering (DLS) device. To evaluate the biophysical effects of NPs, changes in the secondary structures of lysozyme and ALact upon their interactions with bAgNPs are quantified by circular dichroism (CD) spectroscopy. In addition to the experimental studies, the structural stability of single proteins resulting from their interactions with bAgNPs at elevated temperatures is examined by the state-of-the-art DMD simulations. This study offers a new molecular insight into the little known thermodynamics and reversibility of NP-protein interactions and provides a synergic experimental-

computational strategy for facilitating our comprehension of the biological and toxicological implications of engineered nanomaterials.

2. EXPERIMENTAL AND COMPUTATIONAL METHODS

2.1 Sample preparations. BioPure bAgNPs of 20 nm in nominal diameter (0.67 mg/mL, in water) were purchased from NanoComposix. The stock NP suspension appeared homogeneous and free from precipitation when stored at 4°C or diluted in phosphate buffered saline (PBS, pH 7.4) at room temperature. Hen-egg white lysozyme (MW 14,307 Da; isoelectric point 11.35) and bovine milk ALact (MW 14,178 Da; isoelectric point 4.5) were purchased in lyophilized powder form from Sigma-Aldrich. The proteins were then dissolved in PBS to stock solutions of 3 mg/mL, or 210 μM, prior to use.

2.2 Zeta potential. The zeta potentials of lysozyme, ALact, bAgNPs, and NP-protein mixtures were determined using a DLS device (Zetasizer Nano S90, Malvern Instruments) at room temperature. For this measurement the NP and protein stocks were first diluted in Milli-Q water to 0.5 mg/mL for the bAgNPs and 0.11 mg/mL for the proteins. The use of Milli-Q water excluded the complications introduced by the ions in buffer. The NP-protein mixtures were obtained by mixing bAgNPs with lysozyme or ALact at a 1:1 volume ratio followed by a 2 h incubation, which ensured a complete coating of the NPs by the proteins based on geometrical estimations.

2.3 TEM. The sample solutions/suspensions for TEM imaging were prepared as predescribed for the zeta potential measurement. Conventional TEM does not result in clear visualization of polymers or proteins, as such soft matter are subject to shrinkage or severe radiation damage under the electron beam. Negative staining is a technique commonly used for the imaging of biological specimens, and has been applied here to image both the polymer coating and the protein coronas of bAgNPs.

Carbon-coated 300-mesh copper grids were glow-discharged in nitrogen to render the carbon film hydrophilic. A 4 μL aliquot of each sample was pipetted onto a grid. After 30 s of adsorption excess samples were drawn off using Whatman 541 filter paper, followed by staining with 10 μL 2% aqueous potassium phosphotungstate at pH 7.2, for 10 s. Excess stains were drawn off as described before and the grids were air-dried until needed. The samples were examined using a Tecnai 12 Transmission Electron Microscope (FEI, Eindhoven, The Netherlands) at an operating voltage of 120 kV. Images were recorded using a Megaview III CCD camera and AnalySIS camera control software (Olympus). Under TEM the polymer coating and protein coronas appeared as a bright region around the dark central AgNPs, as the regions occupied by the organic material excluded the electron-dense stain, which otherwise appeared as a uniform background of intermediate electron density.

2.4 Temperature-controlled DLS. The hydrodynamic sizes versus temperature were acquired for lysozyme, ALact, bAgNPs, and NP-protein mixtures using an automated, high-throughput, temperature-controlled DLS device (DynaPro Plate Reader, Wyatt) and

black 384-well plates (Thermo Fisher). Prior to mixing, the NP and the protein concentrations were prepared at 0.22 mg/mL and 3 mg/mL respectively in PBS. For each NP-protein mixture, the volume of the proteins was fixed at 6 µL while the volume of the bAgNPs was varied from 4 µL to 8 µL and 14 µL. The selection of these concentrations ensured good scattering signals for the DLS device. For the controls the volume of the bAgNPs was 8 µL while that of the proteins was 6 µL, respectively. The total volume of each sample well was topped up to 20 µL by adding PBS. Prior to the DLS measurements the samples were incubated for 2 h and spun for 1 min at 1,000 rpm/164 RCF (Centrifuge 5804, Eppendorf) to ensure good mixing. Each sample well was then topped with glycerol of 10 µL to prevent volume loss and concentration variations through heating. The thermal cycler of the DLS device was programmed to an increment rate of 0.52°C/min during heating from room temperature to 50°C (actual temperature recorded: 53.4°C) or 70°C (actual temperature recorded: 71.4°C), respectively, followed by a decrement rate of 0.52°C/min back to room temperature. The selection of 50°C as one upper limit for heating ensured a temperature range relevant to biological systems, while the selection of 70°C exploited the full temperature range when lysozyme is not yet denatured. At the end of each heating or cooling step of 5s, the optical module collected data, which was automatically processed and displayed using the Dynamics 7.1.7 software. To ensure repeatability and statistics each sample condition was measured with triplicates or quadruplicates.

2.5 Circular dichroism spectroscopy. To access the effects of NP binding on the secondary structure of the proteins, spectra were recorded using a J-815 circular dichroism spectrometer (JASCO) for a quartz cuvette of 3 mm path length over a wavelength range of 195~300 nm at room temperature. Data were collected every 0.1 nm with a bandwidth of 1 nm at a scanning speed of 50 nm/min and averaged over three measurements. The proteins (10 μg/mL or 0.7 μM, in PBS) were incubated with bAgNPs (2 μg/mL, in PBS) for 2 h at room temperature before each measurement. The final spectra were baseline-corrected and the data were measured in mean residue ellipticity (θ) and converted to the standard unit of $deg \cdot cm^2 dmol^{-1}$ using equation $[\theta]=(\theta \times M_0)/(10{,}000 \times C_{soln} \times L)$, where M_0 denotes the mean residue molecular weight (114 g/mol), C_{soln} is the protein concentration (g/mL) and L is the path length through the buffer (cm).

2.6 DMD simulations. DMD is a special type of molecular dynamics algorithm with high sampling efficiency, which has been extensively used to model biomolecules. Detailed descriptions for DMD algorithm can be found elsewhere.[138,144] We used a united atom representation to model the molecular system, explicitly modeling all polar hydrogen and heavy atoms and with implicit solvent. Inter-atomic interactions were modeled by a physical force field adapted from Medusa,[45,77] which included VDW, solvation, electrostatic and hydrogen bond interactions. The force field parameters for VDW interactions, bond length, angle and dihedrals were taken from CHARMM 19.[78] The solvation energy was included using the Lazaridis-Karplus implicit solvent model, EEF1.[79] The distance and angular dependant hydrogen bond interaction was modeled

using a reaction-like algorithm.[45] We used the Debye-Hückel approximation to model the screened electrostatic interactions between charged atoms. The Debye length was approximately 1 nm by assuming water relative permittivity of 80, and a monovalent electrolyte concentration of 0.1 M.

We adopted the recently developed AgP molecular mechanics force field[136] to model the AgNP surface. We used the (111) surface with 10 layers of atoms to model the NP surface. The AgP force field included both physical and chemical absorptions, aromatic, and "image" charge interactions. The physical and chemical absorptions as well as aromatic interactions were modeled with Lennard-Jones potentials. The "image" charge interaction was modeled with polarizable dipoles, where a freely-rotatable dipole is attached to each metal atom. We simply attached a charged virtual atom (-0.3e) to each metal (0.3e) atom with a fixed bond length (1.0 Å) as implemented in the AgP force field. Except the electrostatic interaction, the virtual atoms did not have any other interaction. In order to use the AgP force field in our implicit DMD simulations, we also needed to include the solvation interaction, the solvation energy ΔG_{solv} in the EEF1 model. To determine the optimal ΔG_{solv}, we scanned the value and performed DMD simulations of AgNP binding with various amino acids. We computed the binding energies of various amino acids with an AgNP surface in DMD simulations and compared them with the values obtained from MD simulations using AgP[136]. We estimated the binding energy in DMD simulations as the difference of the averaged potential energy of the bound state with respect to the unbound states. We obtained the

best correlation between DMD and MD derived binding energies when ΔG_{solv}=8.0 kcal/mol.

The X-ray crystallography structures of lysozyme (PDB code: 1hen) and ALact (PDB code: 1f6s) were used as the reference structures. The dimension of Ag(111) surface was set as ~8×8 nm^2. For the replica exchange simulations, we used 12 replica with temperatures ranging from 275K to 365K. For the constant-temperature DMD simulations, 20 independent simulations with different initial conditions of relative distance and orientations were performed in order to reduce any bias of initial configurations and improve sampling statistics. Counter ions (Cl^-, Na^+) were added to render the net charge of the molecular system zero.

3. RESULTS AND DISCUSSION

Zeta potentials of bAgNPs and proteins. The zeta potentials of the proteins and the NPs in Milli-Q water were determined as +12.1 (±1.6) mV for lysozyme, -14.6 (±3.3) mV for ALact and +25.8 (±1.5) mV for bAgNPs. In comparison, the zeta potentials were +16.5 (±0.8) mV for the mixture of bAgNP-lysozyme and -13.2 (±1.1) mV for the mixture of bAgNP-ALact, respectively. The similarity of the zeta potentials of ALact and bAgNP-ALact suggests a comprehensive coating of the negatively charged protein onto the positively charged NPs through electrostatic attraction, a feature not shared by the positively charged lysozyme and bAgNPs due to their mutual repulsion. This observation

was further corroborated by the TEM and DLS measurements as well as DMD simulations, as detailed in the following sections.

TEM imaging of NP-protein corona. The TEM imaging showed that the bAgNPs were of ~20 nm in diameter and each NP was coated by a thin bPEI polymer layer of ~1.7 nm (Fig. 3.1A), in agreement with the manufacturer's specifications. Both the lysozyme and ALact controls appeared globular of 5 nm or less in size (Figs. 3.1B and 3.1C). In comparison, the mixture of bAgNP-lysozyme (Fig. 3.1D) after 2 h of incubation displayed a size distribution similar to that of bAgNPs alone, implying the lack of corona formation for the like-charged NPs and protein, in agreement with the zeta potential measurement. The mixture of bAgNP-ALact (Figs. 3.1E and 3.1F), in contrast, rendered protein coronas of approximately 3~11 nm in thickness, indicating the strong binding between the oppositely charged species and coating of single- to multi-layer proteins on the NP surfaces.

Hydrodynamic size of bAgNP-protein. As shown in Fig. 3.2A, the hydrodynamic radius of lysozyme remained at ~2.1 nm (±0.3 nm of standard deviation) for the entire temperature range of 18~53.4°C. This is understandable considering that melting of lysozyme occurs at ~73°C.[131] The hydrodynamic radius of bAgNPs was 14.7 (±0.2) nm throughout the same temperature range (Fig. 3.2B), indicating the thermal stability of the polymer-coated NPs. In contrast, when bAgNPs and lysozyme were mixed at respective concentrations of 0.088 mg/mL and 0.9 mg/mL, to ensure an abundance of the protein for a hypothetical NP-protein corona based on a geometrical estimation,[130,131] heating from

room temperature to 53.4°C induced an increase from 14.7 (±0.5) nm to 16.7 (±0.2) nm in the hydrodynamic radius of the mixture, while cooling caused a reversed process characterized by a distinct hysteresis (Figs. 3.2C and 3.2D). The 13.6% increase in the hydrodynamic radius over elevated temperatures suggests a swelling induce by thermal agitation in the radius of gyration (Rg) of lysozyme. The hysteresis points to a reversible process of bAgNP-lysozyme interactions, probably resulting from the electrostatic repulsion between the like-charged NPs and the protein. Consistently, the histograms of the bAgNP-lysozyme hydrodynamic radius in Figs. 3.2E and 3.2F display a strong resemblance, with the cooling process inducing a slightly broader but still similar distribution compared with the heating process. Since the hydrodynamic radius of the bAgNP-lysozyme mixture mirrors that of the bAgNPs alone, and in consideration of the principle of DLS that the intensity of light scattering is proportional to the sixth power of the particle diameter, we infer that there was no substantial formation of a NP-protein corona for the mixture of bAgNP-lysozyme. This prognosis is consistent with the TEM observations (Fig. 3.1D).

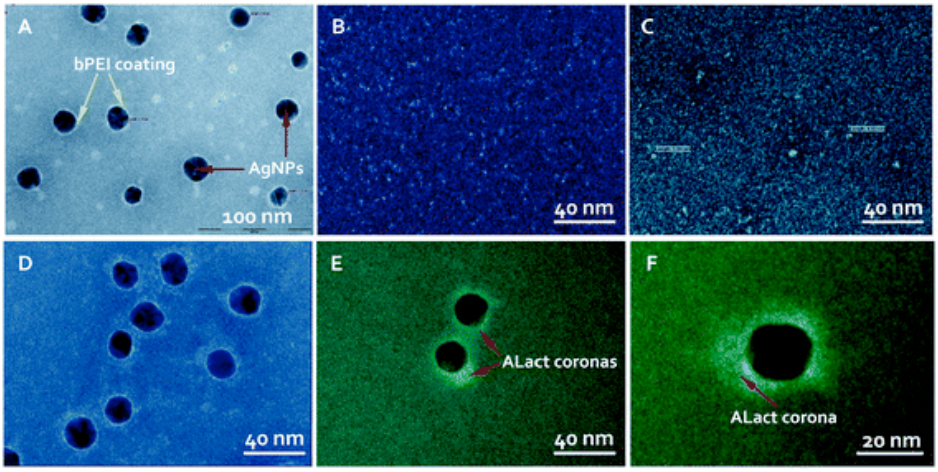

Figure 3.1 TEM images of bAgNPs (A), lysozyme (B), ALact (C), bAgNP-lysozyme (D), and bAgNP-ALact (E, F). The thin white layer of ~1.7 nm surrounding each bAgNP (yellow arrows) is presumably the bPEI polymer coating (A, D). Both lysozyme and ALact appear as small white globules of 5 nm or less. The arrows in (E) and (F) indicate ALact coronas of ~3-11 nm in thickness on the bAgNP surfaces.

In contrast to the bAgNP-lysozyme interactions, the binding between bAgNPs and ALact induced marked increases in the hydrodynamic radius of the bAgNP-ALact mixture. As shown in Figs. 3.3A and 3.3B the hydrodynamic radius of the ALact control increased from 2.1 (±0.2) nm to 6.4 (±2.2) nm during heating from room temperature to 53.4°C and scaled back to 3.3 (±0.7) nm during cooling, suggesting the role of thermal agitation in compromising the structural stability of ALact. In comparison, the hydrodynamic radius of the bAgNP-ALact mixture rose rapidly to 54 nm at room temperature and increased further to as high as 247.7 nm at 53.4°C, further characterized by a pronounced broad distribution (±144.1 nm at 53.4°C, Fig. 3.3C) to indicate cross linking between the bAgNPs through ALact. Upon cooling, the hydrodynamic radius of the mixture decreased back to 113.9 (±19.7) nm at room temperature, which is still

significantly larger than the value of 53.6 nm prior to heating. Compared with the small hydrodynamic radius of the protein (Figs. 3.3A and 3.3B) and the intermediate size of the NPs (Fig. 3.2B), and in connection with the TEM imaging (Figs. 3.1E and 3.1F), such large hydrodynamic radii reflect the formation of NP-protein coronas (indicated by the multiple peaks in Fig. 3.3E) and NP-protein aggregation mediated by electrostatic attraction, hydrophobic interaction and hydrogen bonding between NP-protein and protein-protein. Unlike the bAgNP-lysozyme interactions (Fig. 3.2C), no clear and repeatable hysteresis was observed for the hydrodynamic radius of bAgNP-ALact through heating and cooling (Figs. 3.3C and 3.3D). Since the hydrodynamic size distributions expand up to three orders of magnitude in the histograms of Figs. 3.3E and 3.3F that are dissimilar in either peak positions or relative intensities, also since there is a lack of prominent peaks around the hydrodynamic radius of bAgNPs (Fig. 3.3E), we infer that the binding between AgNPs and ALact was strong and irreversible. In addition, formation of NP-protein aggregation appeared more pronounced with increased NP concentrations, as evidenced by a comparison of Figs. 3.3G and 3.3H, where the slope of hydrodynamic radius/temperature was elevated from 8.7 nm/°C to 14.3 nm/°C when the NP concentration was increased from 0.044 mg/mL to 0.154 mg/mL, with the protein concentration fixed at 0.9 mg/mL.

Although both bAgNPs and lysozyme remained stable up to 71.4°C (Fig. 3.2B and Fig. C1A in Supporting Information), the interactions between bAgNPs and lysozyme prompted their mutual aggregation at or above 70°C, as shown by the sharp departure of the NP-protein hydrodynamic radius from those at lower temperatures in

Figs. C1B and C1C (Supporting Information). This phenomenon differs from that in Fig. 3.2, where heating and cooling of bAgNP-lysozyme was confined between room temperature and an upper limit of 53.4°C. This implies that the presence of bAgNPs triggered an earlier onset of lysozyme melting, which consequently induced protein-protein and NP-protein aggregations. Notably, cooling from 71.4°C down to room temperature did not recover the original hydrodynamic radius of 14.7 (±0.2) nm as assumed by the NP-protein mixture at low temperatures (Fig. C1D vs. Figs. C1B and C1C), indicating the irreversible process of bAgNP-lysozyme interactions once the protein had undergone melting and aggregation. Comparatively, the binding of bAgNPs and ALact appeared irreversible for heating and cooling up to 71.4°C (Fig. C2), characteristically similar to that observed for heating and cooling of bAgNP-ALact up to 53.4°C (Fig. 3.3).

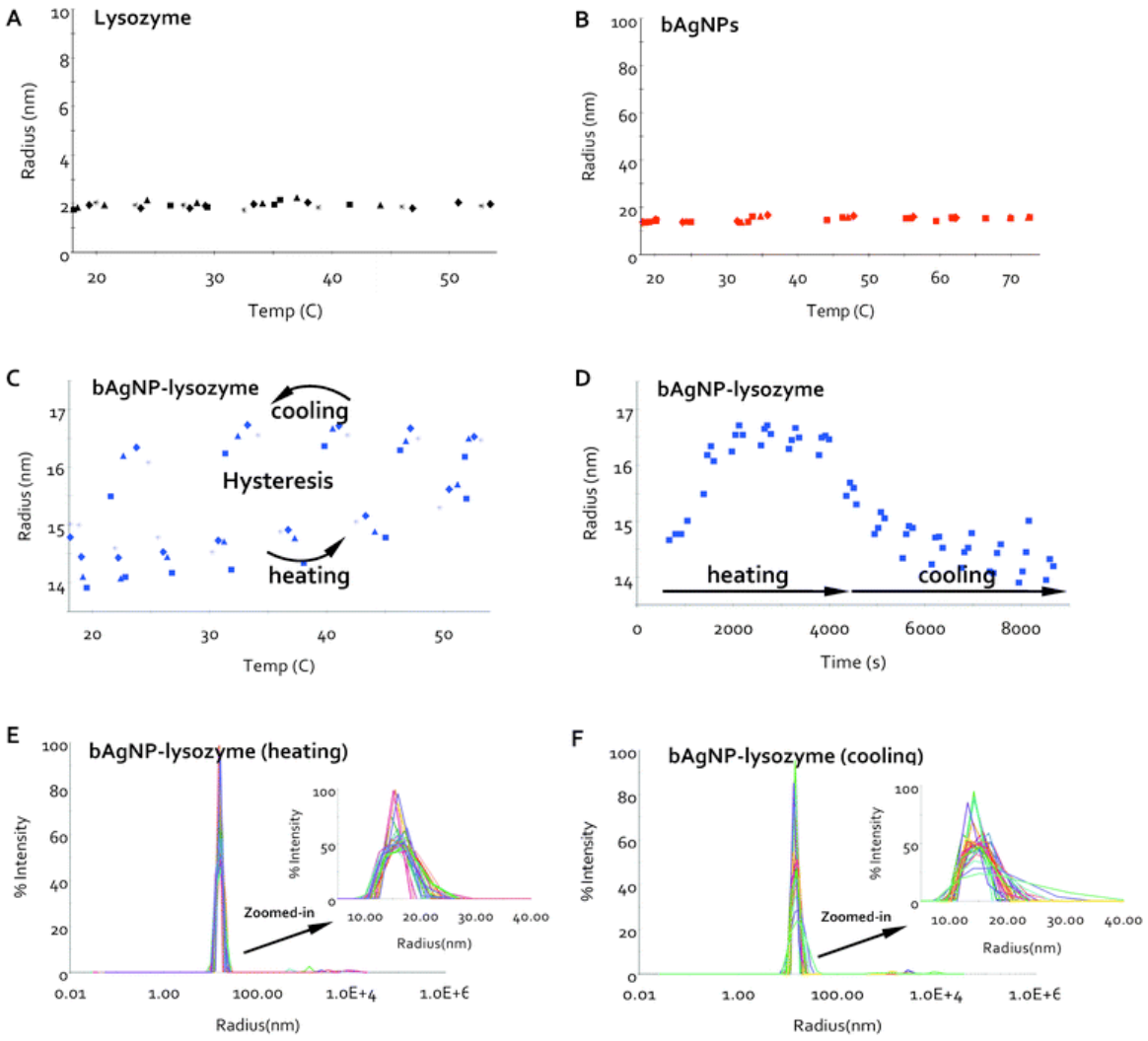

Figure 3.2 DLS measurement of bAgNP-lysozyme heated to 53.4°C (except for (B), where heating extends to 71.4°C) and cooled back to room temperature. (A) Hydrodynamic radius of the lysozyme control. (B) Hydrodynamic radius of the bAgNP control. (C) Hydrodynamic radius of bAgNP-lysozyme versus temperature, displaying a hysteresis between heating and cooling. (D) Corresponding to (C), hydrodynamic radius of bAgNP-lysozyme versus time. (E, F) Histograms of bAgNP-lysozyme hydrodynamic radius during heating and cooling, with their zoomed-in views shown in insets for more detail. (A-F) Lysozyme: 0.9 mg/mL and (B-F) bAgNPs: 0.088 mg/mL, all in PBS. The diamond, triangles, squares and stars represent data points obtained from different sample wells of the same conditions.

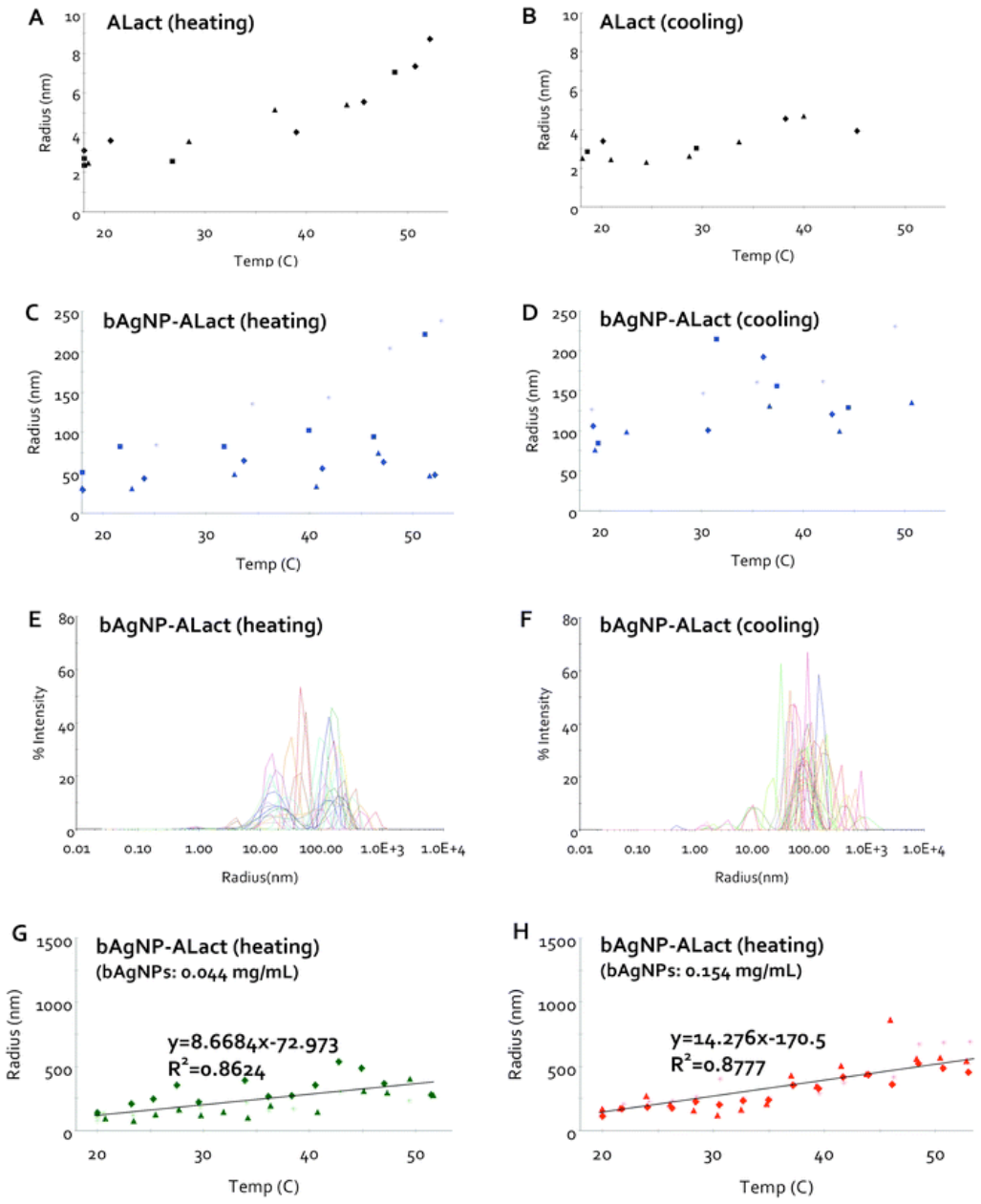

Figure 3.3 DLS measurement of bAgNP-ALact heated to 53.4°C and cooled back to room temperature. (A, B) Hydrodynamic radius of ALact during heating and cooling. (C, D) Hydrodynamic radius of bAgNP-ALact during heating and cooling. (E, F) Histograms of bAgNP-ALact hydrodynamic radius during heating and cooling. (G, H) Hydrodynamic radius of bAgNP-ALact during heating for different NP:protein ratios. The slopes of the fitted linear trendlines are 8.7 and 14.3 nm/°C, respectively. ALact: 0.9 mg/mL (A-H). bAgNPs: 0.088 (B-F), 0.044 (G) and 0.154 mg/mL (H). All samples in PBS. The diamond, triangles, squares and stars represent data points obtained from different sample wells.

Changes in protein secondary structure induced by bAgNPs. A CD experiment was performed to provide an insight into the effects of bAgNPs on the secondary structure of the proteins. As shown in Fig. 3.4 (raw data see Fig. C3), the presence of bAgNPs caused a reduction in the beta sheet component but minimal changes overall in the secondary structure of lysozyme. In comparison, binding with bAgNPs yielded a 20% reduction in the alpha helical content coupled with a 36% increase in the turns of ALact, indicating a stronger impact on the structure of ALact than lysozyme when exposed to bAgNPs, consistent with the TEM and DLS observations.

DMD simulations of bAgNP-protein binding. We performed DMD simulations to examine the binding of a bAgNP with the two types of proteins *in silico*. The AgNP was modeled by a (111) silver surface with ten atom layers. The major physical interactions considered include VDW, solvation energy, and the electrostatic interaction of "image" charges. The interaction parameters were adopted from a recently developed AgP molecular mechanics force field[136] (Methods). We first modeled the binding of capping molecules to the NP surface. We used the generation-3 PEI dendrimer to model the bPEI molecule. As a reference, we also studied citrate coating of the NP by DMD simulations. We found that both PEI and citrate bound to the AgNP surface (Figs. C4B and C4C) via charge-"image" charge interactions. In addition, PEI showed a stronger binding to the AgNP than citrate, as reflected by the higher dissociation temperature of the PEI (Fig. C4A). This stronger binding of PEI and AgNP was due to the large number of charged

amine groups of the polymer. This result is consistent with the visual observation that citrate-capped AgNPs display a slightly higher propensity for aggregation than bPEI-capped AgNPs. We also performed DMD simulations of multiple PEI binding with an AgNP. Due to the high number of charges of PEI molecules bound to the NP surface, the local salt concentration near the surface is higher than that of the bulk, and consequently, the screening effect near the NP surface is stronger than the bulk. Indeed, in DMD simulations the counter-ions (Cl^-) added to neutralize the system were able to account for the increased screening of the electrostatic repulsion between the highly charged PEI molecules and the strong PEI-AgNP binding allowed a high density of PEI molecules covering the NP surface (Fig. C5). For example, eight generation-3 PEI molecules were able to cover a surface area of ~8×8 nm^2 with the surface distances between adjacent PEI molecules within or equal to the bulk Debye length, ~1 nm.

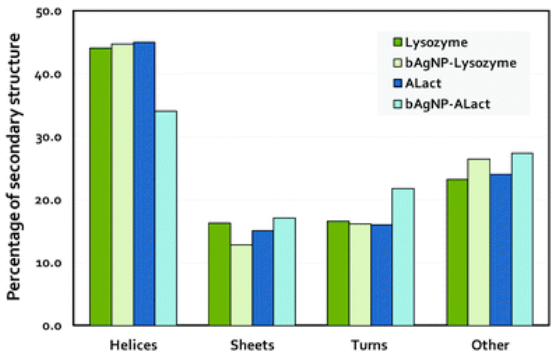

Figure 3.4 Changes in the secondary structures of lysozyme and ALact upon binding with bAgNPs. The proteins (10 µg/mL or 0.7 µM in PBS) were pre-incubated with the bAgNPs (2 µg/mL in PBS) for 2 h at room temperature. The percentages of the secondary structures were calculated by the CDSSTR and CONTIN/LL algorithms of the CDPro package, using SMP56 and SP43 protein reference datasets.

Prior to the study of bAgNP-protein binding, we simulated lysozyme and ALact alone in order to evaluate their corresponding folding thermodynamics. We applied the replica exchange DMD simulation method for efficient conformational sampling[137,138]. Using the weight histogram analysis methods, we computed the specific heat as a function of temperature for both types of proteins (Fig. 3.5A). Different from ALact, the specific heat plot of lysozyme displays more than one peak within the temperature range of 300K to 370K, indicating the population of folding intermediates. The observation of lysozyme folding intermediates has been reported previously.[139,140] Examination of our simulations indicated that the folding intermediates of lysozyme corresponded to the partial unfolding of the beta-sheet in the native structure (Fig. C6), which is consistent with the unfolding pathway identified with all-atom MD simulations.[141] The high temperature peak in the lysozyme specific heat, T_m, corresponds to the global unfolding where the protein loses its helical content (Fig. 3.5B). Therefore, lysozyme has a higher melting temperature and better thermostability than ALact, consistent with the experimental observations (Figs. 3.2A vs. 3.3A).

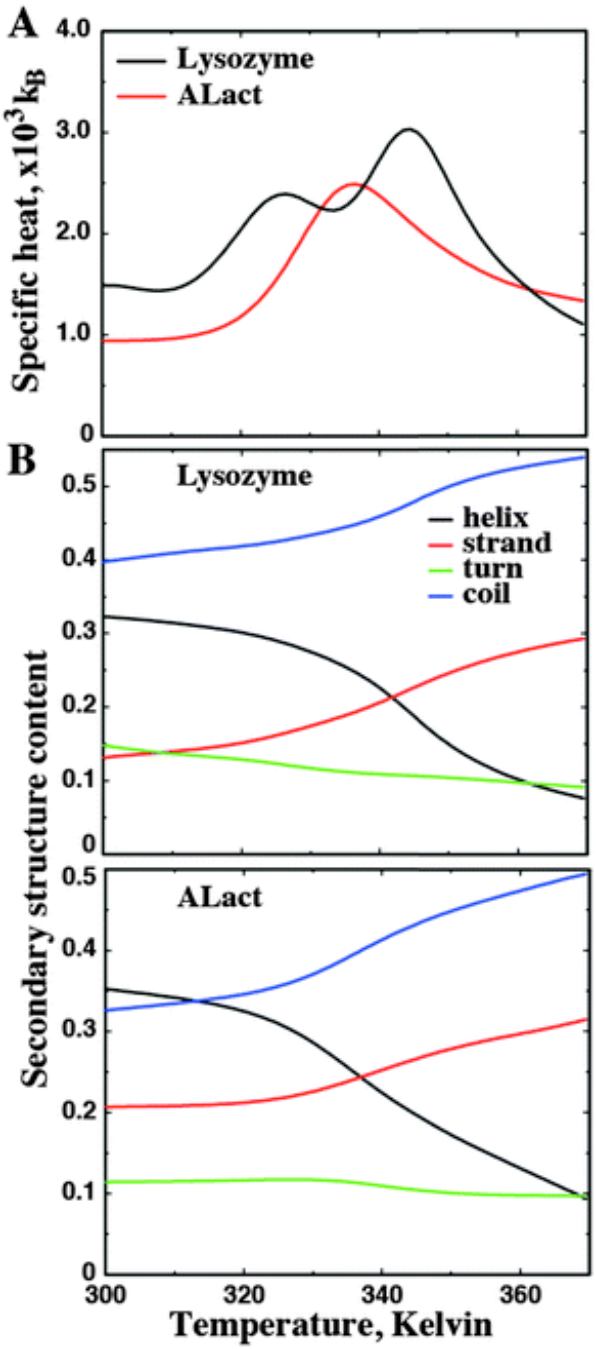

Figure 3.5 The folding thermodynamics of lysozyme and ALact derived from DMD simulations. (A) The specific heat as a function of temperature. (B) The secondary structure content of alpha helices, beta strands, turns and coils as functions of temperature.

Next, we performed DMD simulations of protein binding with an AgNP surface covered by multiple PEI molecules (Fig. 3.6). For each type of the protein species, we performed binding simulations at a wide range of temperatures from 260K to 360K. To ensure sufficient sampling at each temperature, we performed multiple independent DMD simulations (×20) with different initial configurations, including both relative distances and orientations. In all simulations, PEI molecules stayed bound to the AgNP surface. We then calculated the number of inter-molecular atomic contacts between a protein and the PEI-capped AgNP, $NC_{protein\text{-}NP}$. The histogram of intermolecular contacts between lysozyme and bAgNP had only one peak near zero (Fig. 3.6A), while the same histogram of ALact displayed an additional peak with a large number of inter-molecular contacts (Fig. 3.6B). The binding with a small number of inter-molecular contacts corresponds to diffusive non-specific interactions that are transient (Fig. 3.6C). In the case ALact, once the strong binding took place the protein stayed bound to the NP during the entire course of the simulations (e.g. Fig. 3.6D). Therefore, lysozyme showed only weak and transient binding to the bAgNPs, while ALact bound to the positively-charged bAgNPs with a high affinity.

To evaluate the driving force in protein binding, we computed the average number of inter-molecular contacts of protein binding with the AgNP and PEI separately (Figs. 3.7A and 3.7B). We found that the binding was dominated by the interaction between the protein and PEI molecules for both lysozyme and ALact. Due to the electrostatic repulsion between PEIs (+32e) and lysozyme (+7e), lysozyme binding with bAgNP was weak. Similarly, the strong ALact-bAgNP binding was dominated by the

electrostatic attraction between PEI and ALact (-7e). Interestingly, in the case of ALact, we did not observe competitions among the capping PEIs for the NP surface, unlike our previous observation of ubiquitin binding with a citrate-capped AgNP.[49] This discrepancy is consistent with the difference in NP-binding affinities between citrate and PEI (Fig. C4A). As the temperature increased within the sampled range, we did not observe any changes in the NP-binding probability of ALact (Fig. 3.7B). The increasing thermo-fluctuations only reduced the average number of inter-molecular contacts. Therefore, the ALact corona remained stably bound to the AgNP at elevated temperatures.

Table 3.1 The secondary structure contents of ALact at $T = 300K$. The results without (w/o) NP binding are obtained from the replica exchange simulations. The results with NP are derived from multiple independent DMD simulations.

	Lysozyme		**ALact**	
	w/o NP	with NP	w/o NP	with NP
Helix	0.34±0.01	0.34±0.01	0.35±0.01	0.31±0.03
Strand	0.17±0.01	0.16±0.01	0.21±0.01	0.17±0.01
Turn	0.13±0.01	0.14±0.01	0.11±0.01	0.12±0.01
Coil	0.36±0.01	0.36±0.01	0.33±0.01	0.40±0.03

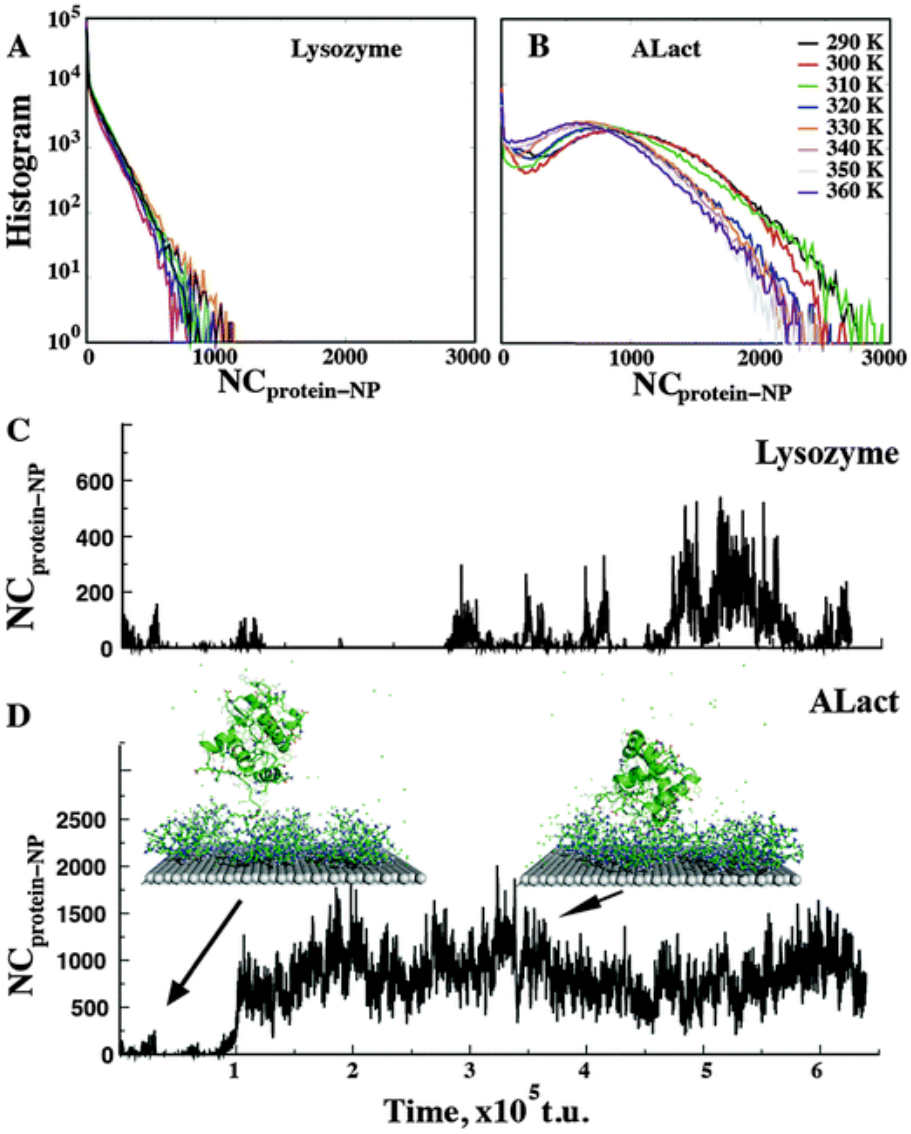

Figure 3.6 The binding between a bAgNP and lysozyme (A, C) and ALact (B, D). The histogram of inter-molecular atomic contacts between protein and NP, $NC_{protein-NP}$ for lysozyme (A) and ALact (B) are derived from DMD simulations. Results from different temperatures are included. (C) A representative trajectory of lysozyme and bAgNP binding at $T = 300K$ indicates that the binding is transient and weak. (D) A trajectory of intermolecular contacts between ALact and bAgNP at $T = 300K$ demonstrates both the weak and strong binding modes. The strong binding with an extensive number of inter-molecular contacts is long lasting.

To evaluate the conformational changes of the proteins due to their binding to a bAgNP, we computed the protein secondary structure contents with and without the bAgNP in DMD simulations (Table 3.1). We found no significant impact on the lysozyme secondary structure due to its weak binding with the bAgNP. In comparison, binding with the bAgNP exerted a strong effect on ALact, where the alpha-helix and beta-strand contents decreased while the coil content increased. The computational results of changes in protein secondary structures upon bAgNP binding are qualitatively consistent with the CD experiment (Fig. 3.4), although the exact numbers are not directly comparable due to the different sample conditions in the two cases. We also calculated other structural parameters of the bAgNP-bound ALact, including the secondary structure contents, root-mean-square deviation (RMSD) and Rg, as functions of temperature (Fig. 3.7C). As temperature increased, the NP-bound protein lost their compact secondary structures like the helices and turns, while the amount of extended conformations of stands and coils increased. The proteins also significantly lost their tertiary structures with increased RMSD and Rg, consistent with the observed increases in the hydrodynamics radius of bAgNP-ALact corona upon heating (Fig. 3.3C). Due to the well-known challenges in computational modeling of protein refolding, we did not perform the refolding simulations. However, our computational study suggests that the strong binding of ALact with bAgNPs may trap the protein in the unfolded states, resulting in the experimentally observed irreversibility of binding.

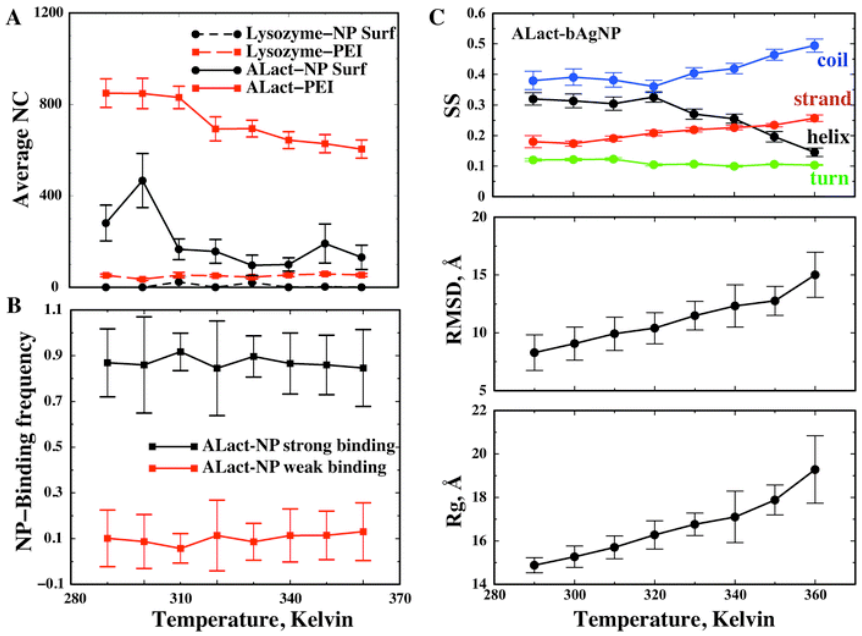

Figure 3.7 The thermodynamics of bAgNP binding with proteins. (A) The binding of the proteins with the AgNP surface and with PEI was calculated separately as the function of temperature. (B) The frequency of binding between ALact and bAgNP was computed as the function of temperature. The weak and strong binding was identified separately. (C) The structural properties of ALact bound to bAgNP, including secondary structure contents (SS), root-mean-square deviation (RMSD), and Rg, were computed as the function of temperature. The error bars correspond to standard deviations computed from independent simulations at each temperature.

4. CONCLUSION

This study has examined the thermodynamics and reversibility of NP-protein interactions, two important aspects which underpin the transformation, function and toxicity of NPs in living systems. Specifically, our combined experimental and computational approach demonstrated that lysozyme and ALact, two homologous proteins with similar structures but distinct sequences and net charges, displayed

drastically different binding affinities for bAgNPs (Figs. 3.2, 3.3, 3.6, 3.7). The negatively charged ALact (-7e) exhibited a strong and irreversible binding to bAgNPs, while the positively charged lysozyme (+7e) showed only a weak and transient binding characterized by a distinct hysteresis, as reflected by the contrasting trends in the hydrodynamic radius (Figs. 3.2 and 3.3) and average number of contacts of the NP-protein mixtures (Figs. 3.6 and 3.7).

Both the CD measurement and DMD simulations (Fig. 3.4 and Table 3.1) revealed that binding to bAgNPs had a minimal impact on the secondary structure of lysozyme but a strong effect on the secondary structure of ALact. When compared with free ALact molecules, binding to AgNPs induced significant losses in its secondary structure. As temperature increased, ALact did not dissociate from the AgNP (Fig. 3.7B) while kept losing its structures (Fig. 3.7C), contributing to the increased hydrodynamics radius of the NP-protein corona as observed in the DLS experiment (Fig. 3.3C). The increase of the ALact hydrodynamics radius could also be induced by the protein-mediated corona-corona binding. Taken together, protein denaturation in a corona and inter-corona protein association resulted in the observed irreversibility of bAgNP-ALact binding upon cooling.

In addition, due to the charge-“image” charge electrostatic attractions, the AgNP surface can bind either positively or negatively charged molecules (Fig. C4), so that both bPEI and citrate can be used as the capping agents. Our DMD simulations revealed that PEI molecules with a high number of cationic primary amines bound to AgNP stronger

than citrate. PEI molecules did not dissociate from the AgNP within a wide range of temperatures while citrates already dissociated (Fig. C4A). Such strong binding allowed a high capping density of PEIs on the AgNP surface, efficiently stabilizing the AgNP from agglomeration (Fig. C5). With a high number of PEI molecules covering the AgNP surface that did not dissociate, protein binding with the AgNP was determined by the physicochemical properties of the PEI capping agent, allowing the oppositely charged ALact to bind to the AgNP favorably. This observation differs from the case of protein binding with a citrate-capped AgNP,[49] where weakly-bound citrates were rapidly replaced by ubiquitin molecules upon competitive binding to the AgNP. Therefore, both the surface chemistry and dynamic properties of ligands play an important role in protein binding and, thus, the corona formation. This new insight may prove valuable for guiding nanomaterials design and synthesis.

Methodologically, we were able to develop an all-atom DMD model for AgNP based on the recently published AgP molecular mechanics force field. Due to limitations in computational sampling efficiency, molecular dynamics simulations with silver and gold particles[136,142,143] have been mostly focused on NP-binding with small organic ligands, amino acids and peptides. The efficient sampling of DMD allowed us to study the structure, dynamics and thermodynamics of the large systems of AgNP-proteins in the presence of capping agents. The recapitulation of various experiments, including differential NP-ligand binding (citrates vs. PEI), bAgNP-protein binding (lysozyme vs. ALact) and changes in protein secondary structure upon bAgNP binding, highlights the

predictive power of the DMD approach in studying the nano-bio interface for advancing the fields of nanotoxicology, nanobiotechnology and nanomedicine.

Dendrimers inhibit protein amyloid aggregations

Gurzov, E. N.; Wang, B. et al. Inhibition of hIAPP Amyloid Aggregation and Pancreatic β-Cell Toxicity by OH-Terminated PAMAM Dendrimer. Small, 12(12):1615-1626 (2016). Reproduced in part with permission from John Wiley and Sons

1. INTRODUCTION

Islet amyloid polypeptide (IAPP, a.k.a. amylin) is a 37-residue peptide hormone, co-synthesized, co-stored and co-secreted with insulin by β-cells, which plays an important role in the glycemic control by slowing down gastric emptying.[145] IAPP is one of the most amyloidogenic protein sequences known and amyloid deposits of IAPP are found in ~90% type-2 diabetes (T2D) patients.[146] Despite the debate of whether islet amyloid is the cause or result of β-cell dysfunction, accumulating experimental evidences suggest that amyloid aggregation of IAPP contributes to the β-cell loss in T2D.[147,148] IAPP aggregates — either insoluble amyloid fibrils or soluble oligomers — are found toxic to β-cells.[149,150] IAPP variants from diabetes-prone primates and cats form aggregates readily *in vitro*, while those from diabetes-free rodents feature significantly weak aggregation propensities.[151] A naturally occurring S20G mutation renders human IAPP (hIAPP) more aggregation-prone, while an Asian subpopulation carrying this mutation is subjected to early T2D onset.[152,153] Moreover, transgenic mice expressing hIAPP start to develop diabetes.[154] Therefore, as in many other amyloid diseases,[155,156] inhibition of IAPP aggregation is an attractive therapeutic strategy to treat T2D.[157]

Stored inside β-cell granules at millimolar concentrations, hIAPP is natively inhibited due to interactions with other granule components, such as high concentrations

of insulin, zinc, and proinsulin c-peptide.[158] Disruption of the natively inhibiting cellular environment may contribute to the formation of amyloid aggregations in diabetes.[154] In order to reduce the aggregation-induced cytotoxicity, anti-amyloid aggregation approaches – such as peptides, peptide-mimetics,[159–162] and small molecules[163–170] – have been exploited. Non-amyloidogenic sequence variants of hIAPP have been found to inhibit the fibril formation of hIAPP,[159,160] and the inhibition efficacies can be improved by synthesizing peptide mimetics with conformational restraints.[161,162] Several small polyphenol molecules, such as epigallocatechin gallate (EGCG),[163,164] morin hydrate,[165] myricetin,[166] resveratrol,[167,168] and curcumin,[169,170] have also been found to inhibit the amyloid fibril formation of hIAPP. Compared to peptide inhibitors, small molecule inhibitors have greater therapeutics advantages.[171] However, many of these IAPP aggregation-inhibiting polyphenols, e.g. myricetin, resveratrol[167,168] and curcumin, have poor water solubility and therefore limited accessibility. On the other hand, recent advances in nanotechnology have opened up new possibilities for nanomedicine-based delivery of these anti-amyloid compounds.

PAMAM (polyamidoamine) dendrimers are a class of polymeric nanoparticles (NPs) with branching units iteratively emanating from a central core, adopting a unimolecular micelle structure in water with a hydrophobic interior and hydrophilic surface groups.[87,93] The number of branching iterations corresponds to the "generation" of the dendrimer, which dictates the NP size and shape. Usually, PAMAM dendrimers have primary amines as the terminal groups, which are positively charged at neutral pH and may induce toxic effects, such as blood clot[172] and depolarization of the cell

membrane.[173] One advantage of PAMAM dendrimers is the straightforward modifications of their surface groups, including replacement of the dendrimer primary amines with hydroxyl groups to minimize the dendrimer toxicity and enhance its resemblance to polyphenols in surface properties, while maintaining the dendrimer high flexibility, small size and good water solubility.

PAMAM dendrimers can host a wide range of ligands,[5,94–96] including several polyaromatic compounds,[174,175] and have been used to encapsulate and deliver small hydrophobic pharmaceutical molecules for enhanced water solubility and biodistribution.[5] Poly(propyleneimine) (PPI) glycodendrimers have been employed for the prevention of A-beta aggregation.[176] Phosphorous dendrimer, maltose-based glycodendrimer (mPPI), PPI and poly(ethyleneimine) hyperbranched polymer have demonstrated anti-prion activity.[177–182] Within the scope of T2D research, cationic PAMAM dendrimer has shown effectiveness in insulin aggregation inhibition.[183] Generation-4 (G4) PAMAM dendrimer has shown the capacity to control blood glucose levels and mitigate hyperglycemia in diabetic rat models.[184] In addition, a competitive binding scheme between fluorescently tagged Concanavalin-A and glycosylated PAMAM dendrimer has been demonstrated, which may be potentially developed into a minimally invasive glucose sensor for diabetics.[185]

In this work, we study the effect of generation-3 (G3) hydroxyl-terminated PAMAM (PAMAM-OH) on the amyloid aggregation of hIAPP and investigated their corresponding cytotoxicities using experimental biophysical characterizations combined

with mechanistic *in silico* investigations and *in vitro* and *ex vivo* assays. We show that the presence of the dendrimer significantly and consistently reduced the cytotoxicity of hIAPP in MIN6 and NIT-1 cell lines as well as in mouse islets. This finding was supported by our high-throughput dynamic light scattering (DLS) experiment and thioflavin T (ThT) spectroscopic assay, where the aggregation of hIAPP was halted by the addition of the dendrimer over time courses of up to 8 h. Our discrete molecular dynamics (DMD) simulations revealed that the dendrimer had a strong binding to hIAPP monomers, especially the amyloidogenic sequence (residues 22-29).[186] Moreover, simulations of hIAPP dimerization revealed that binding with the PAMAM-OH dendrimer significantly reduced the formation of inter-peptide contacts and inter-peptide hydrogen bonds, thereby prohibiting peptide self-association and amyloid formation. Overall, our multi-scale and multi-disciplinary approaches converge on the discovery that polymeric PAMAM-OH dendrimers may act as a promising T2D nanomedicine, and may find additional use in dealing with neurological disorders that are also characterized by amyloid fibrillation.

2. EXPERIMENTAL AND COMPUTATIONAL METHODS

Sample preparations: Human islet amyloid polypeptide (hIAPP) (KCNTATCATQRLANFLVHSSNNFGAILSSTNVGSNTY; disulfide bridge: 2-7; MW: 3,906) was obtained from AnaSpec in lyophilized powder form. The hIAPP was weighed on a Cubis MSE balance (Sartorius, 0.01 mg resolution) and dissolved in Milli-Q water to

form a 0.25 mg/mL (64 μM) stock solution immediately prior to the measurements. Generation-3 (G3) PAMAM-OH dendrimer (stock concentration: 6.25% in water; MW: 6,941) was acquired from Dendritech (Midland, Michigan) and was diluted in Milli-Q water to 0.78 mg/mL (112 μM). Each PAMAM-OH dendrimer constituted an ethylenediamine core and 32 amidoethanol surface groups.

Zeta potential: The zeta potentials of hIAPP (64 μM), PAMAM-OH dendrimer (112 μM) and hIAPP-dendrimer (1:1 molar ratio) in Milli-Q water were determined using a DLS device (Zetasizer Nano S90, Malvern Instruments) at room temperature.

TEM*:* Copper grids (300-mesh, carbon coated) were glow-discharged in nitrogen to promote hydrophilicity. Aqueous hIAPP (0.1 mg/mL or 26 μM), PAMAM-OH dendrimer (0.31 mg/mL or 45 μM), and a hIAPP-dendrimer mixture (of equal volume, or 26:45 molar ratio), all incubated overnight at 4°C, was pipetted onto the grids and allowed 20s of adsorption. Excess samples were then drawn off using filter paper and the grids washed using Milli-Q water. Staining was undertaken using 2% uranyl acetate for 20 s, with excess stain drawn off as previously described. The grids were dried under heated airflow for 20-30 s or as needed. The samples were then examined using a Tecnai G2 F30 Transmission Electron Microscope (FEI, Eindhoven, The Netherlands), operating at a voltage of 300 kV. Images were recorded using Gatan UltraScan 1000 (2k×2k) CCD camera (Gatan, California, USA).

High-throughput DLS: The hydrodynamic diameters of the hIAPP (stock: 64 μM), PAMAM-OH dendrimer (stock: 112 μM) and hIAPP-dendrimer mixtures were measured

using an automated, high-throughput DLS device (DynaPro Plate Reader, Wyatt; resolution: 0.5 nm) and black 384-well plates (Thermo Fisher).[200] For each hIAPP-dendrimer mixture, the volume of the hIAPP was fixed at 6 μL while the volume of the PAMAM-OH dendrimer was increased from 2 μL to 4 μL and 8 μL, rendering a final hIAPP concentration of 19 μM and a hIAPP/dendrimer molar ratio of 12:7, 6:7 and 3:7, respectively. For the controls both the hIAPP and the dendrimer were fixed at 6 μL. The volume of each sample well was topped up to 20 μL by Milli-Q water. Prior to the DLS measurement the samples were spun for 1 min at 1,000 rpm/164 RCF (Centrifuge 5804, Eppendorf) to ensure uniform mixing. An optical module collected data at 20 acquisitions per sample well at room temperature, which was then automatically processed and displayed using the Dynamics 7.1.7 software. To ensure repeatability and statistics each sample condition was measured with quadruplicate. The DLS experiment ran for 470 min in total.

ThT assay: To study the binding kinetics of hIAPP amyloid fibrils formation, the hIAPP stock was diluted to a final concentration of 10 μM in 100 mM Tris-HCL (pH = 7.5), 100 mM NaCl buffer and mixed with 25 μM ThT (Sigma) and varied concentrations of PAMAM-OH dendrimer. Then 100 μL of the each prepared samples was added to a 96 well plate and changes in ThT fluorescence intensity in the control and the hIAPP-dendrimer mixtures were recorded every 5 min over 8 h at a constant temperature of 25 $^{\circ}$C using a BioTek Synergy H1 Hybrid Reader (Excitation: 440 nm; Emission: 485 nm). The time course data were fitted using an empirical equation:

$$I(t) = I_0 + (I_{max}\text{-}I_0)/\{1 + \exp\,[\text{-}k(t\text{-}t_0)]\}$$

Where I_0 and I_{max} are the initial and maximum fluorescence intensity, k is the apparent rate constant of fibrillation, and t_0 is the time required to reach a half of the maximum intensity changed.

Discrete molecular dynamics (DMD): DMD is a special type of molecular dynamics (MD) technique where inter-atomic interactions are modeled by step-wise potential functions instead of continuous potentials. Without frequent calculations of forces at a short time step (~*femtosecond*), the computational efficiency of DMD is increased. The detailed description of the DMD algorithm can be found elsewhere.[41,46] By following the same physical laws and with discretized inter-atomic potential functions mimicking molecular mechanics-based force field,[108,110] the dynamics in DMD is equivalent to continuous potential MD at timescales larger than *picoseconds* with differences mainly at short timescales within the sub-*picosecond range* (i.e., the average time step between two consecutive inter-atomic collisions where a potential energy step is encountered). The predictive power of the atomistic DMD simulations has been demonstrated by observing *ab initio* folding (i.e., without the tertiary structure information in the force field) of a set of small proteins,[108] recapitulating the relative folding rates of different proteins,[201] and capturing the coupled conformational dynamics of large proteins that have been used to engineer allosterically regulated kinases.[202] Recently, we also showed that DMD simulations could recapitulate the experimentally-determined radius of gyration (*Rg*) of PAMAM dendrimers of different generations. In addition to the *Rg* values, the atomic

distributions and the corresponding dynamics of PAMAM dendrimers in DMD simulations were consistent with all-atom MD simulations.[175] Therefore, we applied DMD simulations to study the binding of PAMAM dendrimers with hIAPP peptides.

In our simulations, all molecules were represented by the united-atom model, where all heavy atoms and polar hydrogen atoms were explicitly modeled. We used implicit solvent in the simulations. Inter-atomic interactions considered included van der Waals (VDW), solvation, electrostatic interaction and hydrogen bond. The solvation energy was estimated using the Lazaridis-Karplus implicit solvent model, EEF1.[44] The distance and angular dependent hydrogen bond interaction was modeled using a reaction-like algorithm.[203] We used the Debye-Hückel approximation to model the screened electrostatic interactions between charged atoms. The Debye length was approximately 1 nm by assuming water relative permittivity of 80 and a monovalent electrolyte concentration of 0.1 M.

The coordinates of hIAPP were obtained from the protein data bank (PDB code 2L86).[204] G3 PAMAM-OH was generated as described previously.[175] Basic and acidic amino acids of the hIAPP were assigned charges according to their titration states at physiological pH=7.4. The Arg and Lys residues were assigned +1, the Asp and Glu were assigned -1, while the His was neutral. Tertiary amines in the PAMAM-OH dendrimer were uncharged. The net charges of the molecular systems were maintained at zero by adding offsetting charges (Cl^-) to account for possible counterion condensation.[111] In DMD simulations, temperature had the unit of kcal/(mol•k_B), where k_B is the Boltzmann

constant. Our simulations were conducted at 0.60 kcal/(mol•k_B), corresponding to room temperature T=300 K, with a scaling factor of ~500. The Anderson's thermostat was used to maintain constant temperature.

We simulated one dendrimer interacting with one hIAPP monomer and also with two hIAPP monomers. In each case, we initialized the molecular system by assigning hIAPP monomers away from the dendrimer with random orientations. We also performed simulations of a single hIAPP monomer and two hIAPP monomers as the controls. To ensure sufficient sampling and avoid potential bias of initial conditions, we performed ten independent simulations for each molecular system starting with different initial configurations, including randomized velocities, different inter-molecular distances and orientations. For each independent simulation, energy minimization was first carried out for one thousand time steps (approximately 0.05 ns with 1 DMD time step corresponding to ~50 fs), followed by production simulations. Each production run lasted two million steps (approximately 100 ns), corresponding to an average of approximately 144 CPU hours.

A contact between a residue of hIAPP and PAMAM-OH dendrimer (or two residues of hIAPP) was defined with at least one heavy-atom contact (A 5Å cutoff was used). We computed the content of secondary structures – helix, strand turn and coil – using the backbone dihedral angles.[205,206] All the quantitative calculations, including the mean and standard deviation of contacts and secondary structure contents, were obtained from the latter half of production runs where the molecular systems were found in

equilibrium. For each simulation, we used 10,000 snapshots evenly distributed along the final 50 ns for analysis.

Cell culture and viability: C57BL/6 mice were maintained at St. Vincent's Institute and experiments were approved by the institutional animal ethics committee. Mouse islets were isolated and cultured as described previously.[207] Islets were dispersed into single cells with trypsin and DNA fragmentation was analyzed by staining with propidium iodide.[208] The insulin producing MIN6 and NIT-1 cell lines were cultured in DMEM (Invitrogen, UK) supplemented with 10% fetal calf serum. The percentage cell death of MIN6 and NIT-1 cells was determined in at least 600 cells per experimental condition by inverted fluorescence microscopy after staining with the DNA dyes Hoechst-33342 (10 μg/mL) and propidium iodide (5 μg/mL). The cells and islets were cultured in Opti-MEM (Life Technologies) for treatment with hIAPP (10 μM), PAMAM-OH (6 μM) or 10 μM hIAPP pre-treated for 16 h with 36 μM PAMAM-OH. hIAPP and PAMAM-OH concentrations were selected according to published data and our own dose response[209]. The cells were treated for 24 h and the islets for 48 h before the viability assessment.

Statistical analysis: Data are represented as means ± SEM. Given the paired nature of the experimental design, comparisons between treated groups were made by analysis of variance (ANOVA). A p value <0.05 was considered statistically significant.

3. RESULTS AND DISCUSSION

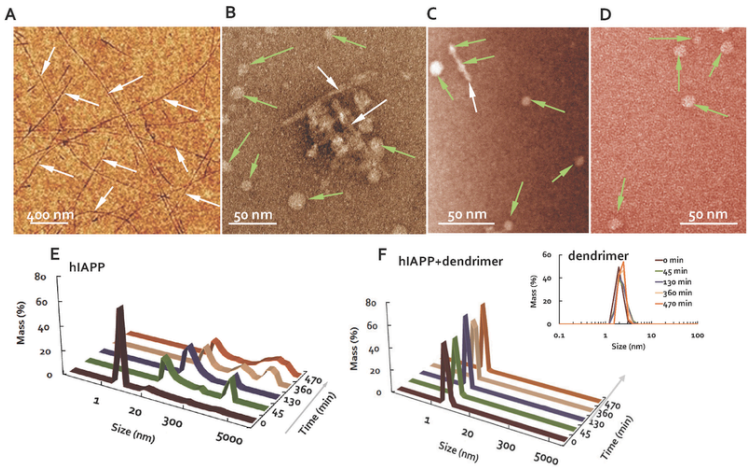

Figure 3.8 TEM (A-D) and high-throughput DLS (E, F) characterizations of hIAPP aggregation and its inhibition by G3 PAMAM-OH dendrimers. A: TEM image of hIAPP amyloid fibrils, mostly at 1 μm or longer, indicated by white arrows. B, C: TEM image of much shortened and sparsely distributed hIAPP amyloid fibrils (exemplified by white arrows) induced by PAMAM-OH dendrimer. B-D: The spherical particles (exemplified by green arrows), a few nanomaters in size, are inferred to be hIAPP-dendrimer clusters as they were entirely absent in the dendrimer (Figure S1) or hIAPP control images (A). This is further corroborated by the co-localizations of such spherical particles with the fibrils in B and C indicating binding between the dendrimer and peptide species. Incubation times for A-D: overnight. hIAPP concentrations in A-C: 0.1 mg/mL (25 μM) and 0.05 mg/mL (12.5 μM), respectively. Dendrimer concentration in B-D: 0.16 mg/mL (23 μM). E, F: Time evolutions of the hydrodynamic diameters of hIAPP (19 μM) and hIAPP-dendrimer mixture at a 6 μL:4 μL volume ratio (or 6:7 in molar ratio), respectively. Inset of F: Size distribution of PAMAM-OH dendrimer (33 μM) over time.

3.1 Experimental evidences of hIAPP fibrillation inhibition by G3 PAMAM-OH dendrimer

The zeta potentials of hIAPP and PAMAM-OH dendrimer were first determined to be +4.71 (±0.39) mV and -10.5 (±1.51) mV in Milli-Q water at room temperature. In

comparison, hIAPP-dendrimer mixture at a 1:1 molar ratio rendered a zeta potential of -4.85 (±0.38) mV. TEM imaging showed the occurrence of abundant amyloid fibrils after overnight incubation of hIAPP at 0.1 mg/mL (26 μM), which were usually ranged over 1 μm in length (Figure 3.8A) and 7~14 nm in width. This is consistent with the literature[187] and the understanding that hIAPP at micromolar concentrations is prone to fibrillation through molecular assembly.[188] In the sample where hIAPP and dendrimer were mixed with equal volumes, short (tens of nm) fibrils were occasionally spotted and associated with small spherical objects of less than 10 nm in size (Figures 3.8B, C). These spherical objects were prevalent regardless of the presence of fibrils (Figures 3.8B-D), and are inferred to be hIAPP-dendrimer clusters as they were absent in either the dendrimer (Figure D1) or the hIAPP control images (Figure 3.8A). Co-localization of such spherical particles with fibrils in Figures 3.8B&C further vindicates binding between the dendrimer and the peptide species. Similar spherical nanostructures were reported for G5 PAMAM dendrimers complexing with linear zwitterionic chitosan.[189] This result suggests that PAMAM-OH dendrimer could act as an inhibitor for hIAPP polymerization in the aqueous phase.

Amyloid aggregation of hIAPP was evident from the high-throughput DLS measurement (Figures 3.8E, F). At the initial time point (Figure 3.8F, 0 min), hIAPP displayed a single major peak of hydrodynamic diameter (by mass percentage) centered at 2.2 nm (±0.7), corresponding to the size of a peptide monomer. As time progressed, the single peak of the peptide evolved into more irregular and broader distributions, characterized by double or multiple peaks at significantly larger sizes of tens of

nanometers to micrometers. Specifically, two prominent peaks were seen for hIAPP aggregates at the time points of 45th min and 130th min, while three major peaks were recorded at the time point of 360th min, centered at 56.5 nm, 767.8 nm and 4,590.8 nm, respectively. At the last registered time point of 470th min, two major peaks occurred at 58.1 nm and 3,583.4 nm (Figure 3.8E). The dendrimer controls, in comparison with the hIAPP samples, displayed little variations in hydrodynamic size over time, at a highly monodisperse value of 2.2 nm (±0.1) (Figure 3.8F inset). Here the size of G3 PAMAM was averaged over 20 data points, with each trace ranging between 2-4 nm in Figure 3.8F inset. These are reasonable hydrodynamic sizes of the G3 dendrimer and hIAPP monomers, especially considering the instrument resolution (0.5 nm) and ultrasmall scattering sample volumes (20 μL) of the high-throughput DLS technique. A direct comparison between the TEM and DLS sizes of the dendrimer or hIAPP was not feasible due to the different samples conditions (dehydrated vs. hydrated state) and different working principles and sensitivities of the two techniques. Consistently with the TEM imaging, when the peptide and the dendrimer were mixed together at a molar ratio of 6:7, the process of amyloid aggregation of hIAPP was largely stalled (Figure 3.8F), yielding a single major peak at 2.6 nm (±0.3) in hydrodynamic size. In consideration of the 6^{th} power size dependence of DLS we exclude the presence of traceable hIAPP fibrils in the sample mixture. Comparable results were seen for hIAPP-dendrimer of two other molar ratios of 12:7 and 3:7 (data not shown), indicating effectiveness of using PAMAM-OH dendrimer for the inhibition of hIAPP aggregation.

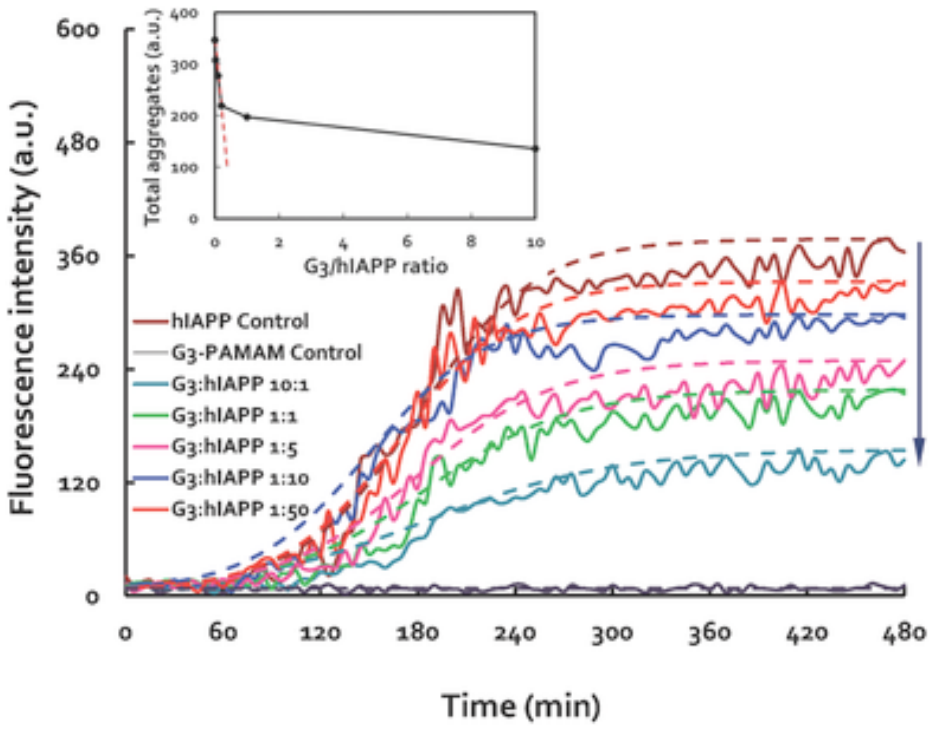

Figure 3.9 ThT assay showing the effect of G3 PAMAM-OH dendrimer on hIAPP aggregation. The inhibition effect of the dendrimer on hIAPP aggregation is evidenced by the monotonic decrease of the ThT fluorescence intensity with increased dendrimer concentration, indicated by the arrow to the right. The dendrimer control showed negligible fluorescence. hIAPP: 10 μM. PAMAM-OH dendrimer: 0.2~100 μM. The assay was run for 8 h. Excitation/Emission: 440/485 nm. (Inset) Total amount of aggregates, corresponding to the maximum fluorescence intensities obtained by the sigmoidal fitting (Methods; dashed lines), is shown as a function of dendrimer/hIAPP ratio. At relatively low dendrimer/hIAPP ratios (≤0.2), a linear decrease of the total aggregates was observed (red lashed line). Such linear decrease levelled off at higher dendrimer/hIAPP ratios.

Thioflavin T (ThT) is a commonly used assay for the visualization and quantification of amyloid fibrillation induced by protein misfolding and aggregation.[190] Specifically, binding of ThT dye to cross-beta architecture induces an enhanced fluorescence intensity, sometimes accompanied by a redshift in the peak fluorescence

wavelength. Changes in the ThT fluorescence intensities are used to indicate the amount of amyloid aggregates. Figure 3.9 shows the time-course data of hIAPP with the empirical sigmoidal fitting (dashed lines). Upon excitation of the ThT-stained samples at 440 nm, the control hIAPP displayed the highest change in fluorescence intensity indicating a rapid amyloid formation of pure hIAPP over time. Addition of PAMAM-OH dendrimer resulted in a significant decrease in the fluorescence intensity signifying inhibited amyloid aggregation. Specifically, the maximal inhibition of aggregation was observed at the highest dendrimer to hIAPP molar ratio (10:1) with the fluorescence signal being 2.3 folds less than it was for the control hIAPP at the plateaus. ThT at 25 μM, which is significantly above its critical micelle concentration of 4 μM,[191] assumed micelles in the sample mixtures. Compared to H-bonding and electrostatic interactions that are favorable between ThT micelles and amyloids,[191] the interaction between ThT micelles and PAMAM-OH dendrimer could only play a minimal role judging from the absence of complete fluorescence quenching at high dendrimer concentrations (10~100 μM).

Fitted with the empirical sigmoidal function (Experimental Section), the amount of amyloid aggregates corresponding to the maximum ThT fluorescence intensity can be obtained as a function of relative dendrimer/hIAPP ratio (Figure 3.9 inset). At relatively low dendrimer/hIAPP ratios (≤0.2), a linear decrease of total aggregates with increasing dendrimer/hIAPP ratio was observed. Such linear dependence suggests an inhibition scenario, where the PAMAM-OH dendrimer inhibited hIAPP amyloid aggregation by sequestering hIAPP monomers. The linear decrease of amyloid aggregations slowed

down at higher dendrimer/hIAPP ratios, likely a result of the self-association of dendrimers via their hydrophobic interiors exposed through constant thermal fluctuations. Nevertheless, the total amount of amyloid aggregates continued to decrease monotonically with increased dendrimer, highlighting strong amyloid inhibition by the polymeric NPs. Specifically, the time t_0 taken for the reaction to reach the half intensity maximum was delayed from 170 min for the hIAPP control to 191 min at the highest dendrimer/hIAPP molar ratio of 10:1, while the apparent rate constant of fibrillation k was reduced from 0.037 min^{-1} to 0.026 min^{-1}.

3.2 Molecular details of hIAPP fibrillation inhibition by g3 PAMAM-OH dendrimer

To understand the mechanisms of hIAPP aggregation inhibition by PAMAM-OH, atomistic discrete molecular dynamics (DMD) simulations were conducted (Experimental Section). We studied the binding of generation-3 PAMAM-OH dendrimer with a hIAPP monomer as well as the effect of PAMAM-OH dendrimer on hIAPP dimerization, an important step toward amyloid aggregation.[186,192] Since the binding of multiple macromolecules is highly stochastic (e.g., Figure D2), we performed ten independent simulations for each molecular system to ensure sufficient sampling. Each simulation started with different initial conditions, including randomized velocities, different inter-molecular distances and orientations. With each simulation ~100 ns long, we obtained an accumulative 1 μs simulation for each studied molecular system.

3.2.1 Dendrimer binds to the amyloidogenic sequence of individual hIAPP

Simulation on dendrimer binding to individual hIAPP was initialized by assigning a hIAPP monomer near a PAMAM-OH dendrimer with random orientations. In order to examine the possible conformational changes of the hIAPP while interacting with the dendrimer, we also simulated the hIAPP monomer itself as a control. We calculated the contact frequency (Figure 3.10A) and number of atomic contacts (Figure 3.10B) between each individual hIAPP residue and the dendrimer. Hot-spot residues with peaks in the number of contact and relative high binding frequency were observed, which implied strong inter-molecular binding. Interestingly, many of hot-spot residues located near the c-terminal, corresponding to the amyloidogenic residues (residues 22-29).[186] Examination of the molecular complex in simulations (e.g., a snapshot structure in Figure 3.10C) suggests that the hIAPP was embraced by the flexible dendrimer, especially near the amyloidogenic region. A comparison of the peptide secondary structures between hIAPP alone and in the presence of dendrimer (as illustrated in Figure 3.10D) indicates that no significant difference was induced, which can be explained by the flexible nature of low-generation dendrimers.[11]

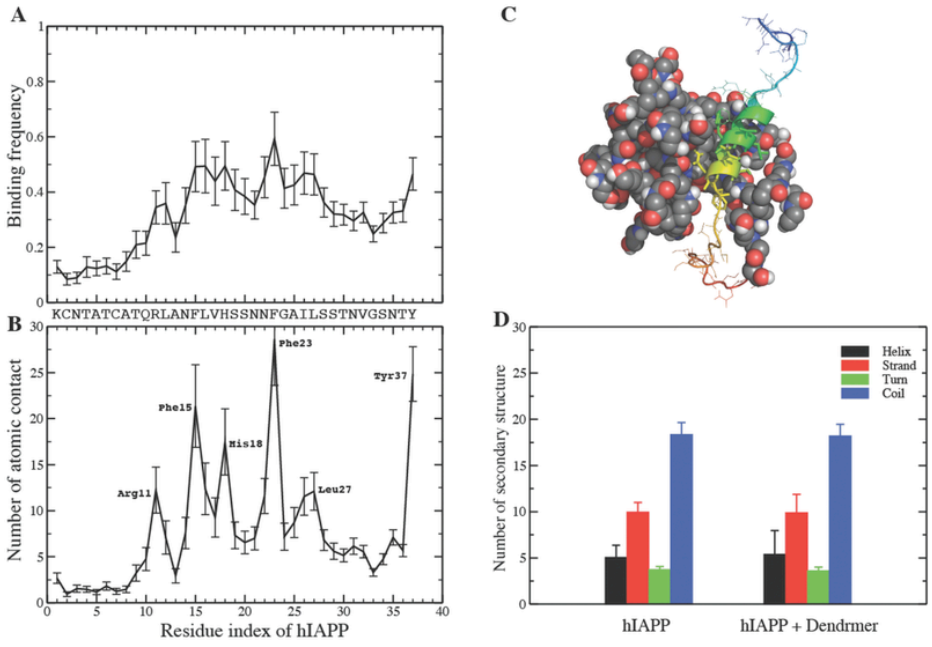

Figure 3.10 (A) Binding frequency and (B) number of atomic contacts between a G3 PAMAM-OH dendrimer and individual hIAPP residues. (C) A snapshot from DMD simulations, where the dendrimer is shown in spherical representation in gray. The peptide in cartoon representation is colored rainbow, where blue corresponds to the N-terminal and red denotes the C-terminal. (D) Secondary structure contents for simulations of hIAPP alone and in the presence of PAMAM-OH dendrimer.

3.2.2 Binding with dendrimer inhibited inter-hIAPP interactions

We further simulated one dendrimer with two separated hIAPP monomers, where each hIAPP monomer was positioned away from the PAMAM-OH dendrimer with random inter-molecular distances and orientations. For comparison, we performed simulations of two hIAPP monomers. We first calculated the average number of hIAPP peptides bound to the dendrimer as a function of time (Figure 3.11A). Despite the initial fluctuations, the number was close to ~1.2 near the end of the simulations, consistent

with the DLS observations of peptide aggregation inhibition at hIAPP/dendrimer molar ratios of 12:7, 6:7 and 3:7. The effect of the dendrimer on inter-hIAPP interactions was evaluated by computing the histograms of the number of inter-peptide contacts (Figure 3.11B) and hydrogen bonds (Figure 3.11C). In the presence of the dendrimer, the probability of observing a higher number of inter-peptide contacts, P_{nc}, was reduced. Similarly, the number of inter-peptide hydrogen bonds, N_{hbond}, was also significantly reduced. Especially, in the presence of the dendrimer, the exponential decrease of the probability of observing a given number of inter-chain hydrogen, P_{hbond}, with increased N_{hbond} suggests no formation of stable β-sheet like structures between the two peptides. In contrast, peaks (shoulders) of the P_{hbond} profile in the hIAPP dimer simulations corresponded to the formation of stable (meta-stable) β-sheets.

To further characterize the structural properties of hIAPP dimers, we computed the inter-monomer contact frequency for all residue pairs with and without the dendrimer. In the case of hIAPP dimer alone, high frequency areas were mostly along the diagonal near the amyloidogenic regions (Figure 3.12A), consistent with the formation of a parallel β-sheets conformation between the amyloidogenic regions (Figure 3.12B) as observed previously.[186] In the presence of the dendrimer, we observed a more scattered pattern (Figure 3.12C). The relatively strong inter-peptide binding occurred in the hydrophobic region near the N-terminal (residues 15-17, $F^{15}LV^{17}$) as illustrated by a snapshot structure with the dendrimer bound to both hIAPP peptides (Figure 3.12D), while the amyloidogenic region of one of the peptides (corresponding to the yellow region in Figure 3.12D) were protected by binding with the dendrimer. It should be noted

that in the aqueous phase, unlike *in silico*, there is little control for hIAPP to assume the monomer or dimer state due to its rapid fibrillation kinetics. In this sense DMD simulations are advantageous over experiments in revealing the mechanisms of hIAPP-dendrimer interaction. Extrapolating the current observation from hIAPP dimer to oligomers and fibrils, we conclude that PAMAM-OH dendrimer inhibited amyloid aggregation of hIAPP by binding to and encapsulating the amyloidogenic sequences, thus preventing their self-association and formation of inter-peptide hydrogen bonds toward amyloid fibrillation.

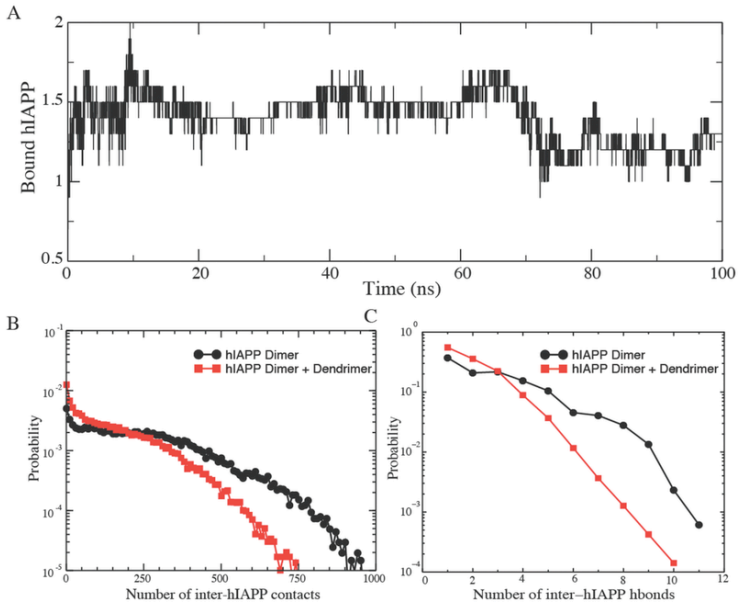

Figure 3.11. (A) The number of hIAPP peptides bound to a G3 PAMAM-OH dendrimer as a function of the simulation time, which was averaged over ten independent simulations (e.g., Fig. S1). (B) The probability densities of the number of inter-hIAPP contacts, P_{nc}, and (C) the number of inter-hIAPP hydrogen bonds, P_{hbond}, for simulations of both hIAPP dimer and hIAPP dimer interacting with a single PAMAM-OH dendrimer.

3.3 PAMAM-OH dendrimer protects β-cells from hIAPP-induced cell death

Next, we determined whether inactivation of hIAPP aggregation by PAMAM-OH can prevent the peptide toxicity in pancreatic β-cells. For this purpose, the mouse β-cell lines MIN6 and NIT-1 were treated with 10 μM hIAPP, 6 μM PAMAM-OH, or combination of both. After 24 h treatment, the cells were exposed to the DNA binding dyes Hoechst 33342 and propidium iodide. Hoechst 33342 freely diffuses and enters cells with intact or damaged membranes, staining DNA blue. Propidium iodide, a highly polar dye, is impermeable to cells with preserved membranes and only stains DNA of death cells as red. Viable cells were identified by their intact nuclei with blue fluorescence, whereas cell death was quantified by blue-red fluorescence or by fragmented blue nuclei.[193]

As a control we first treated NIT-1 cells with PAMAM-OH (6 μM) for 24 h, stained them with Hoechst-33342, and performed immunofluorescence and light microcopy. The dendrimers did not interfere with nuclear DNA staining, as clearly shown in Figure 3.13. We then observed that culture of the mouse β-cell lines with 10 μM hIAPP for 24 h resulted in 50-90% cell death (Figures 3.14A, B), as previously reported.[194] However, pre-treatment of hIAPP with 36 μM PAMAM-OH inhibited fibril formation and prevented hIAPP-induced cell death (Figures 3.14A, B). Consistent results were observed for pre-treatment of hIAPP with equal molar concentration of PAMAM-OH (both at 10 μM) in NIT-1 cells (Figure D3). Importantly, we confirmed this result in

primary cells. Uniformly sized mouse islets from C57BL/6 mice were handpicked into 1-cm Petri dishes containing 1.1 mL of 10 μM hIAPP, 6 μM PAMAM-OH or combination of both, and cultured for 48 h. At the end of the culture period, islets were dispersed with trypsin, and resuspended in 250 μL of hypotonic buffer containing 50 μg/mL propidium iodide, which stained nuclear DNA. The cells were analyzed by fluorescence-activated cell sorter (FACS), and cell death was identified by their subdiploid DNA content as previously described.[195] Dispersed mouse islets incubated with hIAPP for 48 h showed 25% viability, whereas pre-incubation with PAMAM-OH reduced hIAPP-mediated cell death by more than 50% (Figure 3.14C). These *in vitro* and *ex vivo* assays consistently point to the direction that PAMAM-OH dendrimer is an effective inhibitor of hIAPP-induced cytotoxicity.

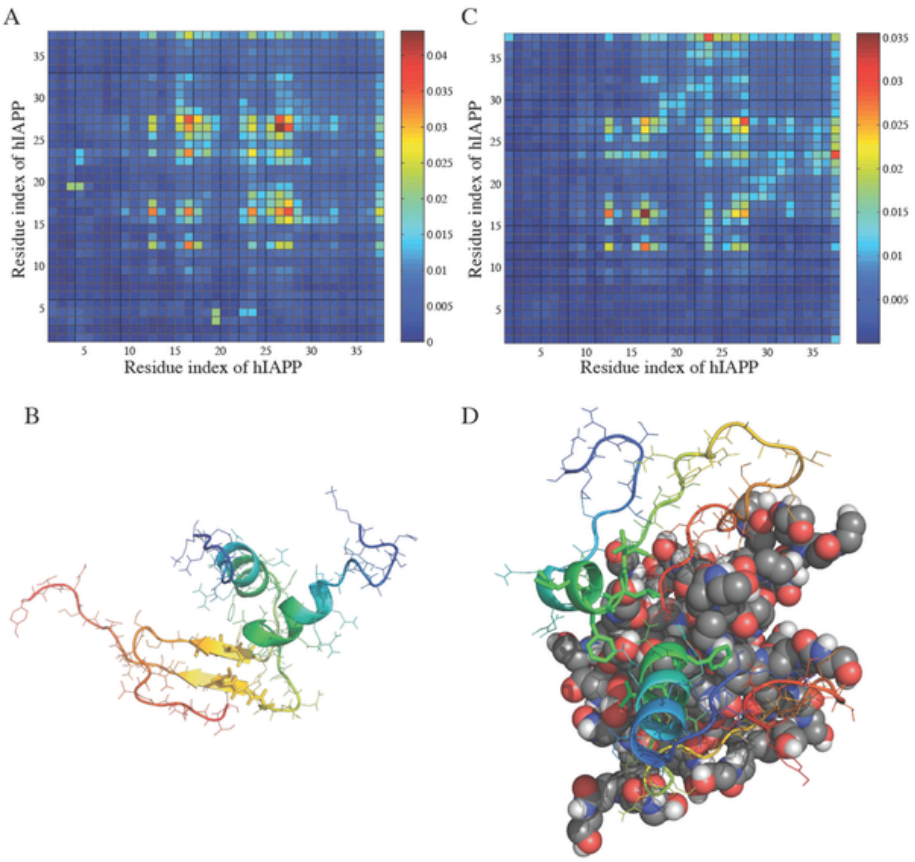

Figure 3.12. Dimerization simulations of hIAPP with and without a G3 PAMAM-OH dendrimer. The residue-wise contact frequencies between two hIAPP peptides were obtained from DMD simulations of two hIAPP monomers alone (A) and interacting with a PAMMA-OH dendrimer (C). We note the difference in the scale of color bars, where the hIAPPs alone case show a higher binding frequency. For the hIAPP dimer alone, the interactions between the two peptides are mostly between the amyloidogenic regions (residues 22-29) of each chain. In the presence of the PAMAM-OH dendrimer, the interactions are more scattered. (B) A typical snapshot structure from the hIAPP dimer simulation. The peptide in cartoon representation is colored rainbow, where blue corresponds to the N-terminal and red denotes the C-terminal. A beta-sheet is formed between the amyloidogenic regions (the yellow regions), while the N-termini remain helical. (D) A snapshot structure from the hIAPP dimer simulation in the presence of the PAMAM-OH dendrimer (in spherical representation). The amyloidogentic region of one peptide was buried by binding with the dendrimer. The hydrophobic region around residues 15-17 ($F^{15}LV^{17}$), which formed inter-peptide interactions, was highlighted in sticks.

A number of mechanisms have been proposed in the literature concerning hIAPP-induced cytotoxicity: disruption of membrane fluidity and the subsequent intracellular hemostasis, generation of reactive oxygen species (ROS) which results in cell death, and apoptosis.[196] Due to its hydrophilicity and weakly negative charge, PAMAM-OH dendrimer alone is not expected to show notable cell uptake. On the other hand, although hIAPP is weakly positively charged (4.71 mV), binding of hIAPP with PAMAM-OH dendrimer rendered a slightly negative zeta potential of -4.85 mV, thereby reducing propensity of the peptide for negatively charged cell membranes to discourage membrane adsorption and cell uptake. Furthermore, encapsulation of hIAPP monomers and their small structural derivatives (i.e., dimers and oligomers) by G3 PAMAM-OH dendrimer prevented the peptides from evolving into hydrophobic fibrils, further minimizing hIAPP perturbation to cell membranes and cell uptake.

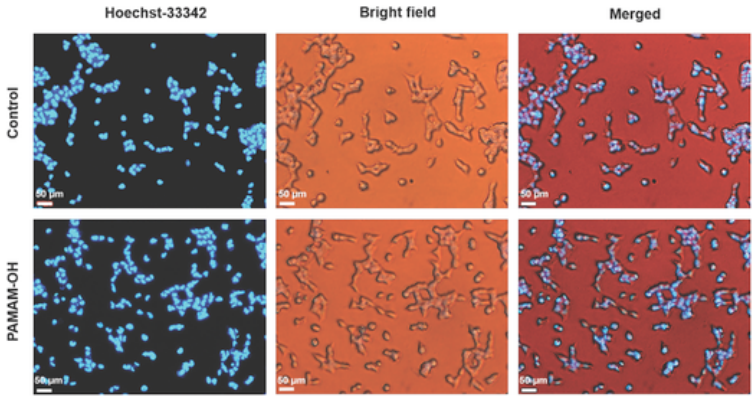

Figure 3.13. 7.5x104 NIT-1 cells were treated with PAMAM-OH (6 μM) for 24 h and nuclear DNA staining evaluated by Hoechst-33342 (blue) and cell morphology by light microscopy. The blue staining corresponds to nuclear DNA in the cells, indicating that PAMAM-OH did not interfere in the viability assay of Figure 7. Images are representative of 5 different fields taken for each sample, Scale bars: 50 μm.

Using the CM-H_2DCFDA assay, Feliu et al. showed that G4 PAMAM-OH dendrimers at concentrations lower than 50 μM elicited no ROS in primary human bronchial epithelial cells.[197] It is conceivable that G3 PAMAM-OH dendrimer used in our study, due to its much reduced numbers of surface groups (32 per G3 vs. 64 per G4 dendrimer) and branches for a given molar concentration, would be comparably or less active in ROS production. Furthermore, binding with the dendrimer could also reduce ROS production by the peptides and their aggregates, as electron-donor peptide residues could be partially buried inside the dendrimer to become less accessible to oxygens and free radicals in the cellular environment. Specifically, all the oxidation-prone residues[198] of hIAPP, including Phe15, His18, Phe23 and Tyr37, showed strong binding with the dendrimer (Figures 3.10A, B) and thus were buried inside the dendrimer upon interactions (Figure 3.10C). A similar phenomenon was observed for the case of hIAPP dimer interacting with the dendrimer (Figures D4, 5D).

Although limited data is available in literature with regard to the apoptotic potential of dendrimers, G3 PAMAM-OH dendrimers at concentrations up to 500 μM – one to two orders of magnitude higher than those employed in our cellular studies – have been shown none apoptotic in MCF7 and MDA-MB-231 breast cancer cells.[199] In short of above analysis, it is plausible that the presence of G3 PAMAM-OH dendrimer physically or physicochemically screened and mitigated the cytotoxicity of hIAPP.

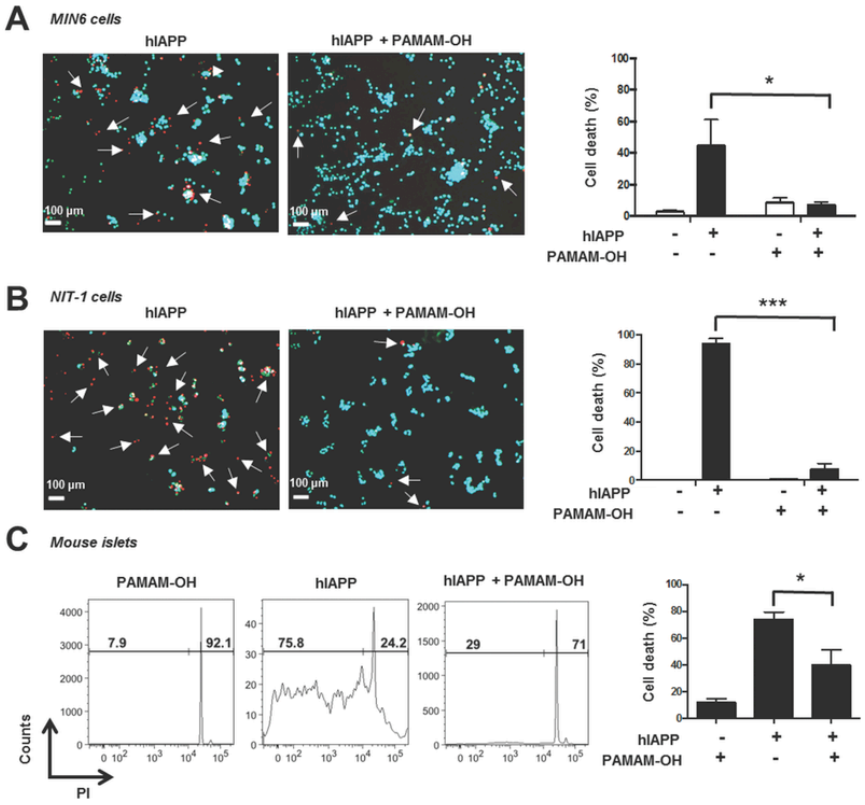

Figure 3.14. G3 PAMAM-OH dendrimer protects β-cells from hIAPP-induced cell death. (A) MIN-6 cells were left untreated (control) or incubated with PAMAM-OH, hIAPP or combination for 24 h. Cell death was evaluated by Hoechst-33342 (blue)/propidium iodide (red). White arrows indicate propidium iodide positive cells. Data shown are means ± SEM of 3 independent experiments. **P* < 0.05. Scale bar: 100 µm. (B) NIT-1 cells were untreated (control) or incubated with PAMAM-OH, hIAPP or combination for 24 h. Cell death was evaluated by Hoechst-33342 (blue)/propidium iodide (red). White arrows indicate propidium iodide positive cells. Data shown are means ± SEM of 3 independent experiments. ****P* < 0.001. Scale bar: 100 µm. (C) DNA fragmentation was measured by flow cytometry in islets from C57BL/6 mice cultured in medium containing PAMAM-OH, hIAPP, or combination for 48 h (n=4). Data shown are means ± SEM, **P* < 0.05.

4. CONCLUSION

We have demonstrated the remarkable effect of G3 PAMAM-OH dendrimer on the inhibition of hIAPP aggregation. While hIAPP of micromolar concentrations

underwent rapid nucleation and elongation in aqueous (Figures 3.8A, C; Figure 3.9), the presence of the dendrimer effectively halted hIAPP polymerization (Figures 3.8B, D; Figure 3.9). The molecular details of such peptide-dendrimer interactions and their induced inhibition of peptide aggregation were further revealed by DMD simulations, where the dendrimer bound to the amyloidogenic regions of hIAPP monomers and impaired the formation of inter-peptide hydrogen bonds and hydrophobic interactions between hIAPP dimers toward amyloid fibrillation (Figures 3.10-3.12).

When hIAPP-dendrimer were introduced to MIN6 and NIT-1 cells and mouse islets, all cell lines and primary cells consistently exhibited significantly reduced cytotoxicity compared with those exposed to hIAPP alone (Figure 3.14). This phenomenon was attributed to the decreased zeta potential (and hence declined affinity) and stalled fibrillation (and hence reduced perturbation) of the peptide for cell membranes upon dendrimer binding, as well as reduced cellular exposure of the oxidation-prone peptide residues that were buried in the dendrimer. Taken together, G3 PAMAM-OH dendrimer not only effectively hindered hIAPP aggregation in aqueous and *in silico*, but also significantly mitigated the toxic effects of the peptides and their aggregates *in vitro* and *ex vivo*. In practice, the high cost of G3 PAMAM-OH dendrimer may be circumvented by the use of its analogue that is comparable in both structural and physicochemical properties, the G3 hyperbranched bis-MPA polyester-32-hydroxyl polymer. This research offers a novel strategy for targeting T2D as well as neurological disorders, and opens the door to the screening and development of other classes of NPs and nanomedicines for amyloid inhibition.

CHAPTER FOUR

CONCLUSION

This dissertation has explored the interactions between dendrimer and a variety of biomolecules including small carbon-based NPs, metal-based NPs, and proteins/peptides. While my investigations were mostly through a computational approach i.e. discrete molecular dynamics (DMD) simulation, a lot of experimental measurements such as UV-vis spectrophotometry, fluorescence, TEM, DLS, Circular dichroism spectroscopy (CD), were also implemented providing supplementary measurements. As current studies of dendrimer-biomolecules interactions are mostly phenomenological based, I believe understanding structure-function relationship of dendrimers from a molecular level would provide profound knowledge to better design and apply dendrimers in the future.

This work has been divided into two portions corresponding two major directions of using dendrimers, namely, environmental applications and biomedical applications. Under each direction, two closely related studies were presented. More specifically, studies of "Structure-function relationships of dendrimers" and "Mechanisms of dendrimer-small molecules binding" were under the Chapter 2 of "Dendrimer in environmental applications". Studies of "Dendrimers as surfactants" and "Dendrimers inhibit protein amyloid aggregations" were under the Chapter 3 of "Dendrimers in biomedical applications".

Structure-function relationships of dendrimers

In this study, I have shown the behaviors of model oil molecules including aliphatic, aromatic, and hybrid hydrocarbons associating with PAMAM-based dendrimers. A lot of interesting results have been observed from experimental measurements. More specifically, model oil molecules could be stably dispersed by PAMAM-based dendrimers over a wide range of temperatures. However, dendrimers with different surface chemistries i.e. G4-NH_2, G4-OH and G4-SA are varied in dispersion efficiency especially at varied environmentally relevant temperatures. To achieve a molecular explanation for those experimental observations, I performed DMD simulations. It revealed that G4-SA and G4-NH_2 bind much more strongly to hydrocarbons than G4-OH due to this neutral dendrimer collapsing, closing off access to the hydrophobic interior. However, changes in tertiary amine pKa and resulting interior protonation in G4-SA due to the abundance of terminal acidic groups severely limited their hydrocarbon hosting capacities.

Another significance of this study was that DMD simulations was benchmarked in modeling dendrimer systems. I simulated dendrimers with different generations and surface chemistry and compared my atomistic characterization with existing experimental measurements. And I found that DMD was similar or better in describing the structure and dynamics of dendrimers than other computational methods. Thus, it was proved to be an effect tool in studying dendrimer system.

Mechanisms of dendrimer-small molecules binding

From the previous study, I learnt that the physicochemical properties of dendrimers are important factor that determining dendrimer-ligands association. As a back-to-back study, I would like to know how the physicochemical properties of ligands affecting the encapsulating paradigm. This study was of great significances considering dendrimers were designed to be delivery vehicles or nanocontainer.

We applied DMD simulations to examine the molecular mechanisms of dendrimers as oil dispersants using two representative hydrocarbons, C16 and PHe. Our previous experimental study indicated that G4 PAMAM dendrimers dispersed linear and aromatic hydrocarbons quite differently, as evidenced in measurements of hydrodynamic size,[99] loading capacity, and stability[37] of the resulting complexes formed between the dendrimer and the hydrocarbons. Based on simulations of single dendrimers interacting with single and multiple hydrocarbons, we revealed a cooperativity in both C16 and PN dispersion by dendrimers. Such cooperativity arose from the increased hydrophobicity of the PAMAM interior upon ligand binding, which in turn facilitated binding of additional ligands. Such a cooperative binding of polyaromatic naphthalene with PAMAM has also been observed in recent all atom MD simulations with explicit solvent.[29] Although PN displayed a stronger binding to PAMAM than C16, stronger inter-ligand interactions led to a higher binding cooperativity for C16 to PAMAM than PHe. Our simulations of multiple hydrocarbons interacting with each other suggest that the same strong inter-ligand interaction between C16 molecules also attributes to their lower solubility than PHe. In actual applications of PAMAM as dispersants, the targeted ligands are usually mixtures of different types of ligands. For example, in our previous experiments,[37] the

mixture of C16 with 8% PN ligands was used as a "model crude", which displayed a higher binding cooperativity than PHe. Although we did not model the mixture of C16 and PN in the current study, we expect that C16 will be a "good" solvent for PN and PAMAM can disperse the hydrocarbon mixtures in the same manner as C16 alone.

Based on the traditional unimolecular micelle paradigm of PAMAM dendrimer, the binding of ligands is saturated once the dendrimer core is filled up and the maximum loading is reached. The unusually large size of molecular complexes formed by PAMAM dendrimers when dispersing C16 suggested a deviation from such an accepted scheme of PAMAM. By further simulating two dendrimers interacting with multiple hydrocarbons we found that C16 and G4 dendrimers formed a highly stable micelle structure across the simulated temperature range (275–400K), in which a small C16 cluster was stabilized by multiple dendrimers on the periphery; the system of PN and dendrimers, however, consisted primarily of multiple PN molecules dispersed in the interior of single dendrimers. These results not only explain the phenomena observed in our earlier experimental studies[37,99] but also illuminate the contrasting mechanisms of dendritic polymers for oil dispersion, where both ligand-ligand and ligand-dendrimer interactions contribute to conjure the dendrimer hosting capacity. Such dynamic capacity may serve as a basis for a range of dendrimer applications in environmental remediation, water purification, catalysis, and gene and drug delivery.

Dendrimers as surfactants

From this study, we were entering the topic of dendrimers in biomedical applications. Dendrimers are polymeric nanoparticles (NPs). Before discussing their potential applications, we are starting with some basic concepts about NP-biomolecules interactions. It is well established that NPs possess the capacity to interact with a myriad of biomolecules, especially with proteins.[31] And the NP-protein complex is terms as nanoparticle-protein "corona". Depending on the binding affinities, NPs may render a "soft" or "hard" corona, which may be modulated by the environments. Exploring NP-protein interactions are critical to elucidate the origin of cytotoxicity.

This study served as nice example to demonstrate those concepts. Here, I investigated the thermodynamics and reversibility of NP-protein interactions, two important aspects which underpin the transformation, function and toxicity of NPs in living systems. Specifically, our combined experimental and computational approach demonstrated that lysozyme and ALact, two homologous proteins with similar structures but distinct sequences and net charges, displayed drastically different binding affinities for bAgNPs. The negatively charged ALact (-7e) exhibited a strong and irreversible binding to bAgNPs, while the positively charged lysozyme (+7e) showed only a weak and transient binding characterized by a distinct hysteresis, as reflected by the contrasting trends in the hydrodynamic radius and average number of contacts of the NP-protein mixtures. Both the CD measurement and DMD simulations revealed that binding to bAgNPs had a minimal impact on the secondary structure of lysozyme but a strong effect on the secondary structure of ALact. When compared with free ALact molecules, binding to AgNPs induced significant losses in its secondary structure. As temperature increased,

ALact did not dissociate from the AgNP while kept losing its structures, contributing to the increased hydrodynamics radius of the NP-protein corona as observed in the DLS experiment. The increase of the ALact hydrodynamics radius could also be induced by the protein-mediated corona-corona binding. Taken together, protein denaturation in a corona and inter-corona protein association resulted in the observed irreversibility of bAgNP-ALact binding upon cooling.

Besides drug delivery, dendrimers could be applied as surfactants, which featured another significance of this study. Due to the charge-"image" charge electrostatic attractions, the AgNP surface can bind either positively or negatively charged molecules, so that both bPEI and citrate can be used as the capping agents. Our DMD simulations revealed that PEI molecules with a high number of cationic primary amines bound to AgNP stronger than citrate. PEI molecules did not dissociate from the AgNP within a wide range of temperatures while citrates already dissociated. Such strong binding allowed a high capping density of PEIs on the AgNP surface, efficiently stabilizing the AgNP from agglomeration. With a high number of PEI molecules covering the AgNP surface that did not dissociate, protein binding with the AgNP was determined by the physicochemical properties of the PEI capping agent, allowing the oppositely charged ALact to bind to the AgNP favorably. This observation differs from the case of protein binding with a citrate-capped AgNP,[49] where weakly-bound citrates were rapidly replaced by ubiquitin molecules upon competitive binding to the AgNP. Therefore, both the surface chemistry and dynamic properties of ligands play an important role in protein

binding and, thus, the corona formation. This new insight may prove valuable for guiding nanomaterials design and synthesis.

Dendrimers inhibit protein amyloid aggregations

Many neurodegenerative diseases such as Alzheimer's disease (AD), type 2 diabetes (T2D) and Parkinson's disease (PD), are correlated with the cytotoxic aggregation of a particular amyloidogenic protein or peptide.[210]. Inhibiting the self-assembly of those amyloidogenic protein or peptide may open opportunities to combat those diseases.

In this study, I have demonstrated the remarkable effect of G3 PAMAM-OH dendrimer on the inhibition of hIAPP aggregation. While hIAPP of micromolar concentrations underwent rapid nucleation and elongation in aqueous, the presence of the dendrimer effectively halted hIAPP polymerization. The molecular details of such peptide-dendrimer interactions and their induced inhibition of peptide aggregation were further revealed by DMD simulations, where the dendrimer bound to the amyloidogenic regions of hIAPP monomers and impaired the formation of inter-peptide hydrogen bonds and hydrophobic interactions between hIAPP dimers toward amyloid fibrillation.

When hIAPP-dendrimer were introduced to MIN6 and NIT-1 cells and mouse islets, all cell lines and primary cells consistently exhibited significantly reduced cytotoxicity compared with those exposed to hIAPP alone. This phenomenon was attributed to the decreased zeta potential (and hence declined affinity) and stalled fibrillation (and hence reduced perturbation) of the peptide for cell membranes upon

dendrimer binding, as well as reduced cellular exposure of the oxidation-prone peptide residues that were buried in the dendrimer. Taken together, G3 PAMAM-OH dendrimer not only effectively hindered hIAPP aggregation in aqueous and *in silico*, but also significantly mitigated the toxic effects of the peptides and their aggregates *in vitro* and *ex vivo*. In practice, the high cost of G3 PAMAM-OH dendrimer may be circumvented by the use of its analogue that is comparable in both structural and physicochemical properties, the G3 hyperbranched bis-MPA polyester-32-hydroxyl polymer. This research offers a novel strategy for targeting T2D as well as neurological disorders, and opens the door to the screening and development of other classes of NPs and nanomedicines for amyloid inhibition.

Future Directions

In this dissertation, we has seen great potentials of applying dendrimers in biomedical applications. There are a lot of challenges still need to be addressed. For instance, although we investigated dendrimers associating some proteins species, the actual behavior of dendrimers in a biological body is largely unknown. In addition, we may achieve some nice results from a lab condition, but further testing dendrimers in an actual biological body might be leading to another story. Even we presume dendrimers will be functional, we need to consider their degradations.

So my ongoing and future work related to this dissertation will primarily focus on the immune response and in-body circulation of dendrimers. In particular, I will investigated how dendrimers associating with serum proteins or enzymes such as human serum albumin. Due to the system complexity, the current studies on the interactions

between dendrimers and those large biomolecules are still far from satisfactory either lacking molecular details or asking for a new models to better explain curtain experimental observations.[5,178,211–218] On the other hand, new dendrimers or dendritic polymers with enhanced functionality and biocompatibility have been kept inventing. So it is worthwhile to further testing them with biomolecules. As DMD simulations have proven predictive power in modeling complicated molecular system, I will further develop and applied DMD simulations to continue my dendrimer studies.

APPENDICES

Appendix A

Supporting Information for the study of

"Structure-Function relationships of dendrimers"

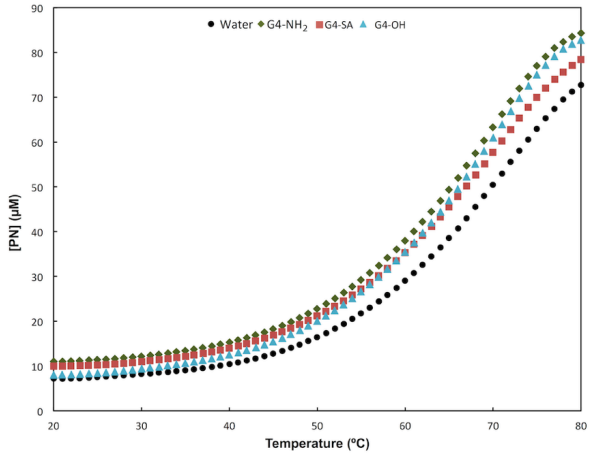

Figure A1. The total concentration of phenanthrene in water or dendrimer solutions as a function of temperature averaged over 3 independent trials for each solution.

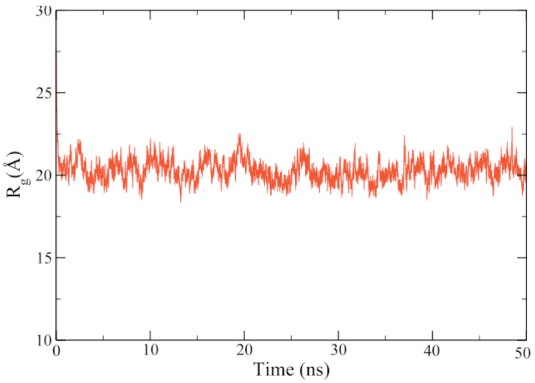

Figure A2. A representative simulation trajectory of Rg as function of time for a G4-NH_2 dendrimer (neutral pH), showing rapid relaxation (2 ns) and equilibration of the system with small thermal fluctuations thereafter.

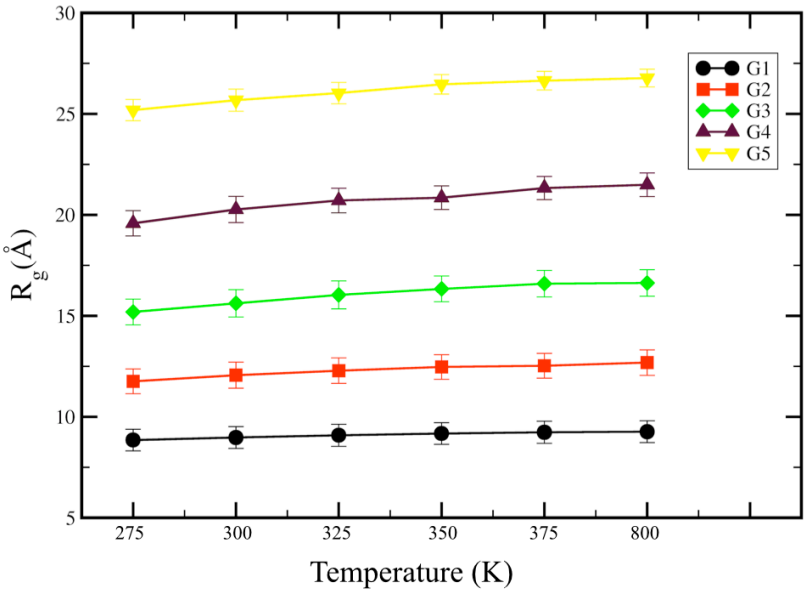

Figure A3. The radius of gyration of NH_2 terminated PAMAM dendrimers of generation 1-5, as a function of temperature. Error bars correspond to standard deviations.

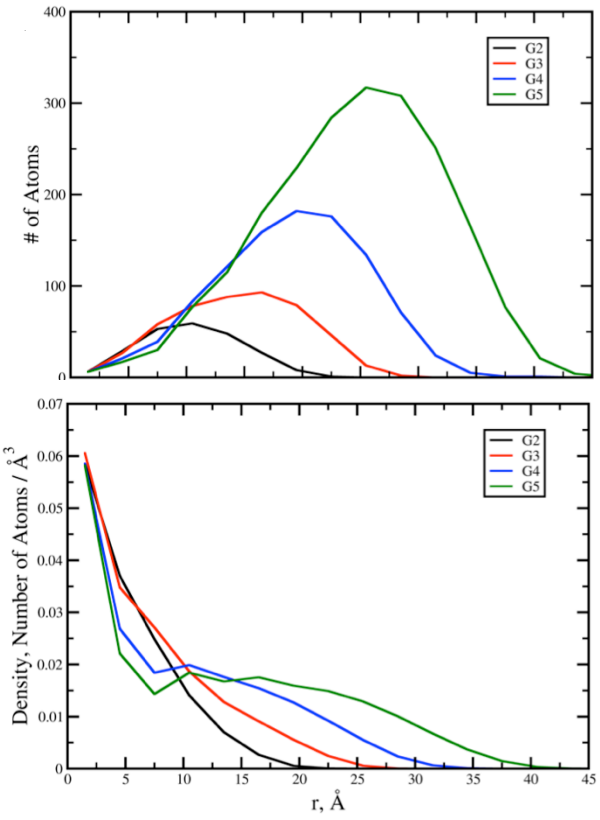

Figure A4. The radial atom distribution (A) and radial density distribution (B) functions are calculated for NH_2-terminated dendrimers of various generations from G2 to G5. Density is computed as the number of atoms per unit volume. The functions are averaged over time where the molecular systems reach equilibrium. As the generation increases, the atom density near the core decreases.

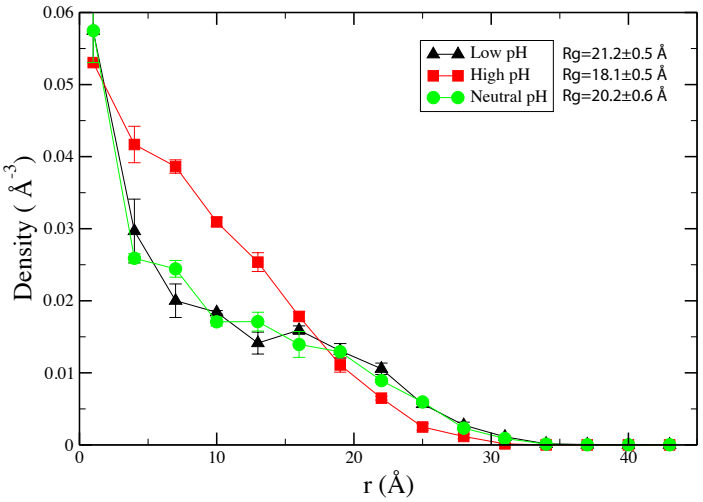

Figure A5. Radial density profile of G4-NH_2 at low, neutral, and high pH, defined as completely protonated, only primary amines protonated, and completely deprotonated, respectively. The error bars are calculated from two independent DMD simulations. We observe a transition from "dense core" (<15 Å) at high pH to "dense shell" (>15 Å) at neutral and low pH, in agreement with previous MD simulations[20]. The average R_g values show modest changes in average size (see inset).

Appendix B

Supporting Information for the study of

"Mechanisms of dendrimer-small molecules binding"

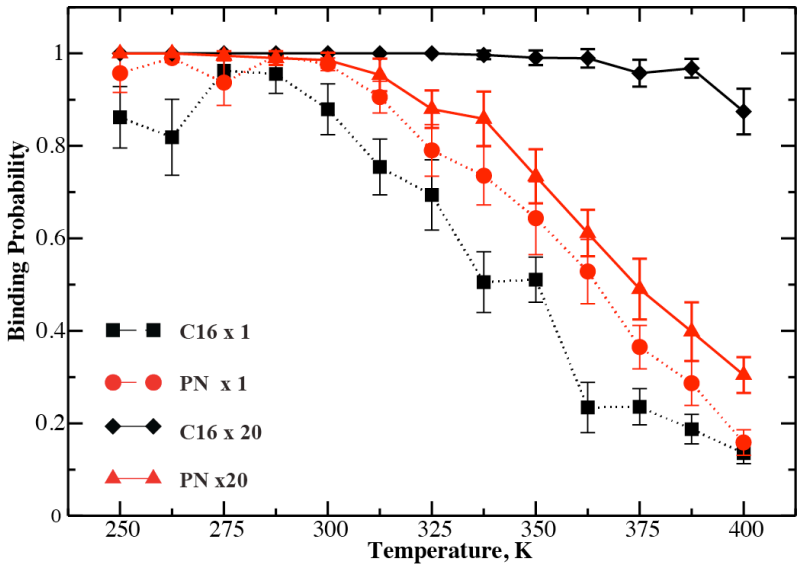

Figure B1. The binding probability per ligand, P_{bind}, was obtained by normalizing with the total number of ligands for simulations of multiple ligands (x20) binding PAMAM (Fig. 2B). For comparison, P_{bind}, for single hydrocarbon binding simulations was also included (dot lines).

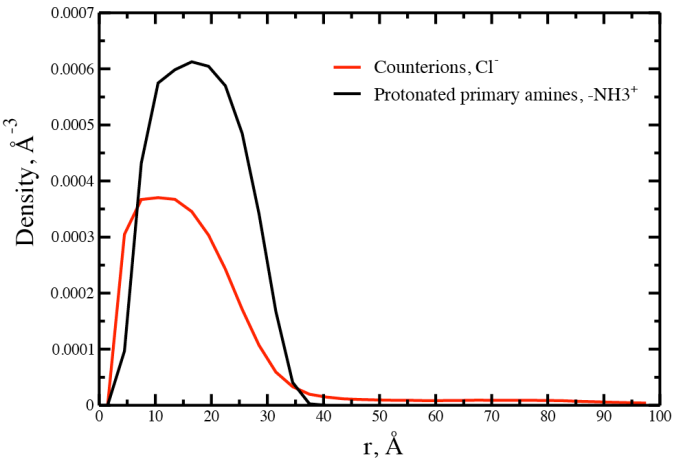

Figure B2. The radial density distributions of counter ions, Cl^-, and protonated primary amines, $–NH_3^+$. The center of the PAMAM core was used as the reference point, and the density was computed as the number of atoms per unit volume with a distance bin size of 2.5 Å. The distributions were averaged over time when the molecular systems reached equilibrium.

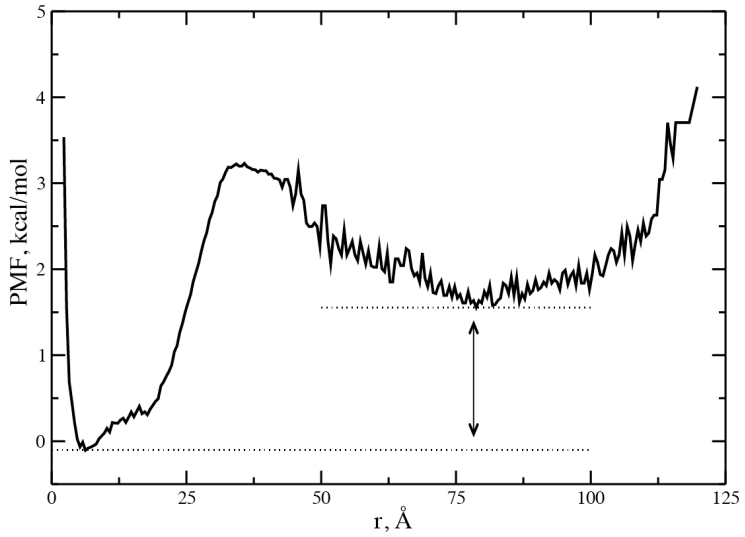

Figure B3. The potential of mean force (PMF) of one C16 binding with one PAMAM dendrimer as the function of the inter-molecular distance, ***r*,** at T = 300 K. The results were calculated from umbrella sampling simulations using the WHAM method (Methods). The PMF minimum at the short ***r*** corresponds to the bound state with a strong inter-molecular interaction. As *r* increases beyond the free energy barrier around ~30 Å (corresponding to the termini of the dendrimer as calculated in Fig. S2), a decrease of PMF occurs, resulting from increased translational degrees of freedom with the minimum around ~80 Å, half of the simulation box size. Dot lines indicate the lowest free energy of bounded and unbounded states.

Table B1. Radius of gyration and ellipiticity of G4-PAMAM dendrimer. The DMD simulation was performed at T=300K for 50 ns.

Radius of gyration, Å	Liu et al.[98] - SANS	This work
	21.4 (0.4)	20.2 (0.6)
Ellipticity	Maiti et al.[11] - MD	This work
	0.70 (0.04)	0.73 (0.07)

Appendix C

Supporting Information for the study of

"Dendrimer as surfactant"

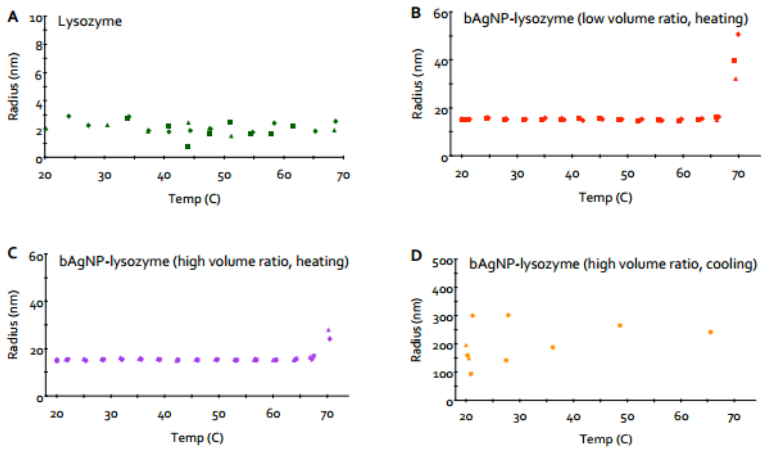

Figure C1. DLS measurement of bAgNP-lysozyme heated from room temperature to 71.4°C and cooled back down to room temperature. (A) Hydrodynamic radius of lysozyme. (B, C) Hydrodynamic radius of bAgNP-lysozyme versus temperature during heating for increasing NP:protein ratios. Lysozyme of 0.9 mg/mL (A-D). bAgNPs of 0.044 mg/mL (B) and 0.088 mg/mL (C, D). (D) Hydrodynamic radius of bAgNP-lysozyme versus temperature during cooling. The diamond, triangles, squares and stars represent data points obtained from different sample wells of the same conditions.

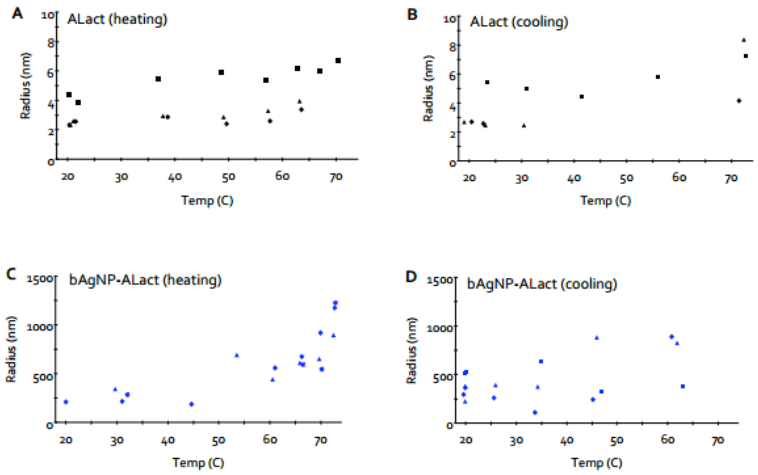

Figure C2. DLS measurement of bAgNP-ALact heated from room temperature to 71.4°C and cooled back down to room temperature. (A, B) Hydrodynamic radius of ALact during heating and cooling. (C, D) Hydrodynamic radius of bAgNP-ALact versus temperature during heating and cooling. ALact: 0.9 mg/mL (A-D). bAgNPs: 0.088 mg/mL (C-D). The diamond, triangles, squares and stars represent data points obtained from different sample wells of the same conditions.

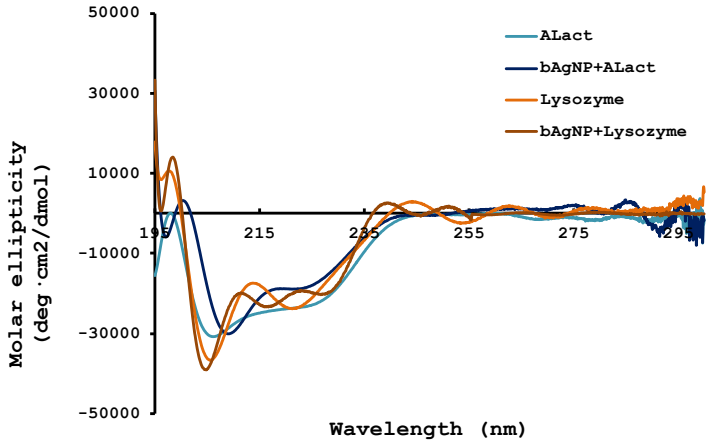

Figure C3. The CD spectra of protein secondary structures in exposure to bAgNPs.

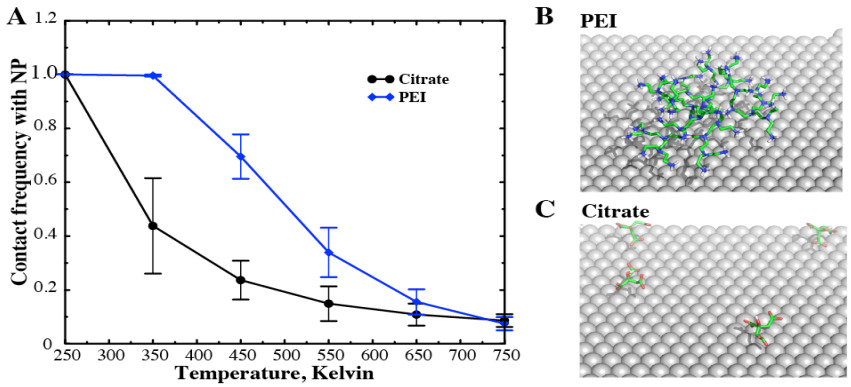

Figure C4. The binding of capping molecules to an AgNP. (A) Two commonly-used capping molecules, citrate and PEI, were studied in DMD simulations. The probability of forming contacts with the NP surface in the simulations was calculated as a function of temperature. PEI displays a stronger binding to NP than citrate because PEI requires a higher temperature to dissociate from the NP surface. The snapshot structures of PEI (B) and citrate (C) bound to NP surface suggest that the strong binding of PEI is due to the electrostatic interactions between the charged amines and their "image" charges.

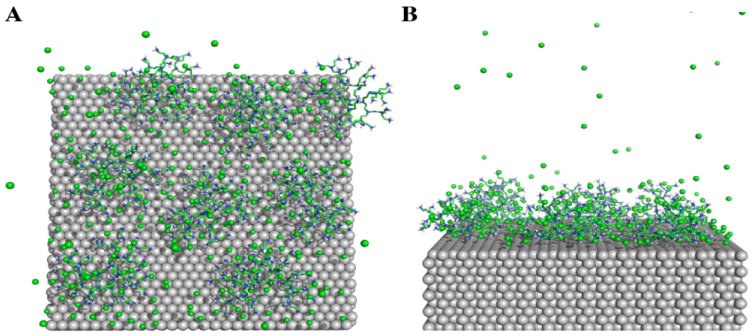

Figure C5. The binding of multiple PEI molecules with an AgNP surface. The counter ions (green spheres) are able to screen the electrostatic repulsion between highly charged PEI molecules (in stick representation), so that multiple PEI molecules can cover the surface of the AgNP to prevent NP-NP aggregation. In our simulations, eight generation-3 PEI dendrimers are able to cover an AgNP surface area of 8.1×8.2 nm^2. Both the top (A) and side (B) views of a PEI-capped NP structure in DMD simulations are shown.

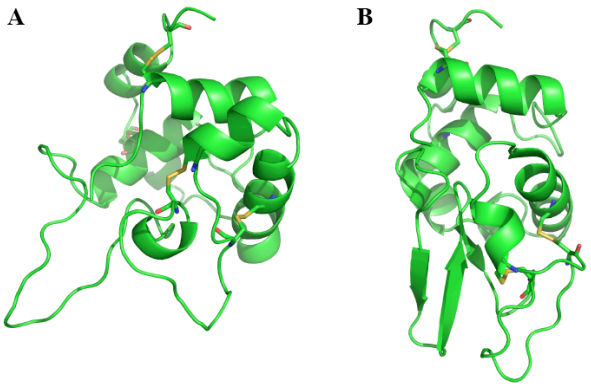

Figure C6. (A) The representative structure of the folding intermediate of lysozyme obtained from DMD simulations. Compared to the native structure (B), the intermediate corresponds to a loss in beta-sheets.

Appendix D

Supporting Information for the study of

"Dendrimers inhibit protein amyloid aggregations"

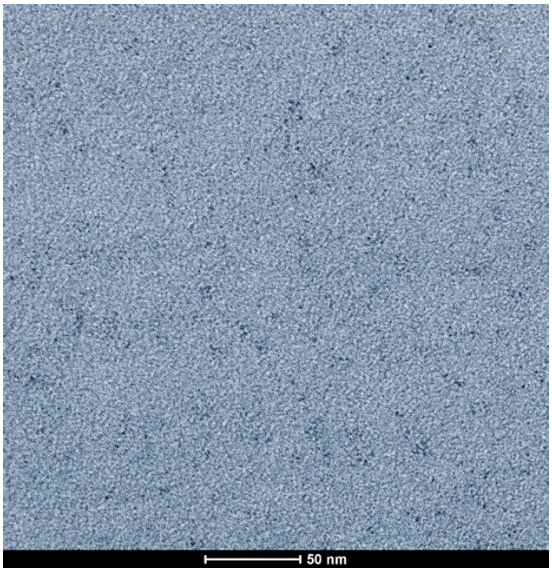

Figure D1. TEM image of PAMAM-OH dendrimer, stained with 2% uranyl acetate and examined using a Tecnai G^2 F30 Transmission Electron Microscope (FEI, Eindhoven, The Netherlands) at a voltage of 300 kV, under the same experimental conditions for acquiring Figures 1A-D.

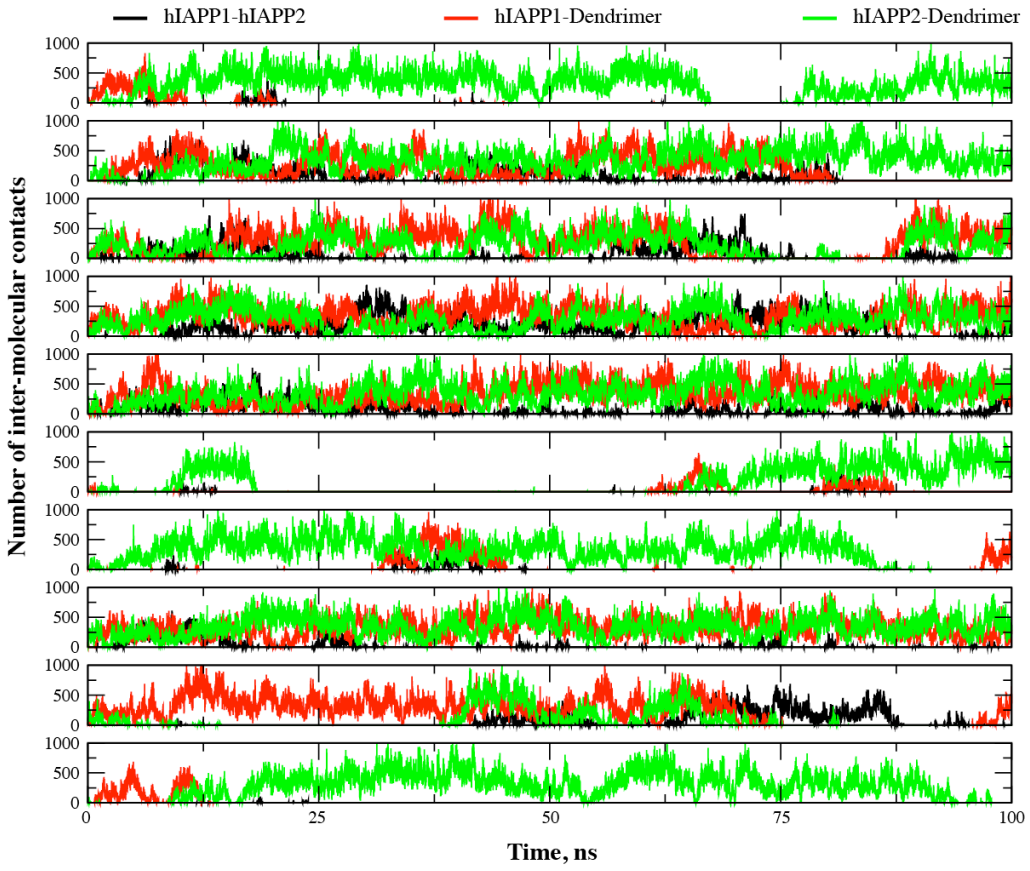

Figure D2. The number of contacts as a function of time between different molecular components (hIAPP-hIAPP, hIAPP-Dendrimer) for ten independent DMD simulations of a G3 PAMAM-OH dendrimer binding with two hIAPP peptides.

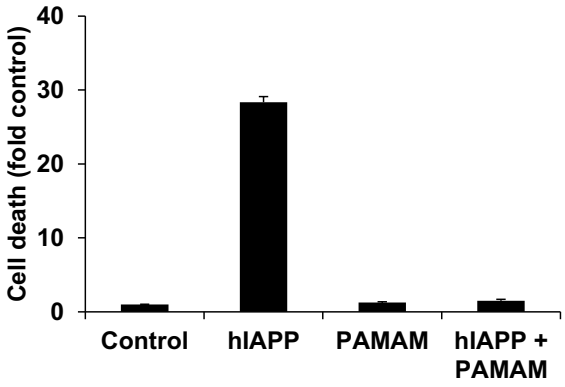

Figure D3. G3 PAMAM-OH dendrimer protects NIT-1 β-cells from hIAPP-induced cell death at a dendrimer/peptide molar ratio of 1:1. Incubation: 24 h. G3 PAMAM-OH dendrimer and hIAPP concentrations: 10 μM. hIAPP was acquired from Abcam for this assay.

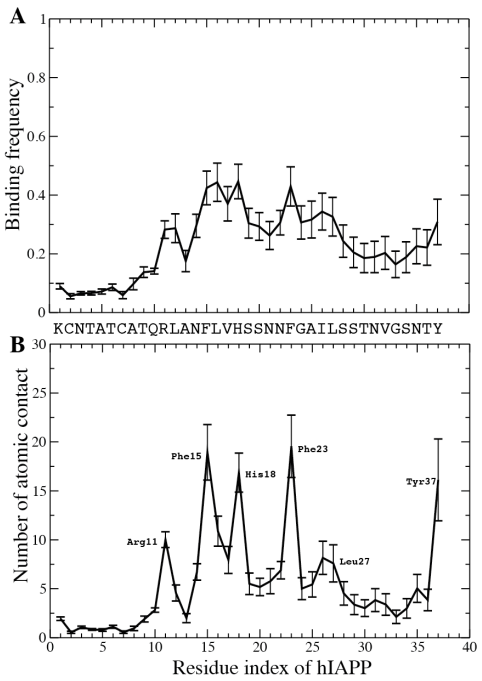

Figure D4. (A) Averaged binding frequency and (B) averaged number of atomic contacts between a G3 PAMAM-OH dendrimer and individual residues of hIAPP dimer.

Appendix E

Copyright permissions

Permission for reproduction of figure 1.1

Copyright Clearance Center RightsLink®

Home | Account Info | Help

Title: New methodologies in the construction of dendritic materials

Author: Anna Carlmark,Craig Hawker,Anders Hult,Michael Malkoch

Publication: Chemical Society Reviews

Publisher: Royal Society of Chemistry

Date: Nov 25, 2008

Logged in as:
Bo Wang
Clemson University
Account #: 3001176633
LOGOUT

Order Completed

Thank you for your order.

This Agreement between Clemson University -- Bo Wang ("You") and Royal Society of Chemistry ("Royal Society of Chemistry") consists of your license details and the terms and conditions provided by Royal Society of Chemistry and Copyright Clearance Center.

Your confirmation email will contain your order number for future reference.

Printable details.

License Number	4156040256009
License date	Jul 25, 2017
Licensed Content Publisher	Royal Society of Chemistry
Licensed Content Publication	Chemical Society Reviews
Licensed Content Title	New methodologies in the construction of dendritic materials
Licensed Content Author	Anna Carlmark,Craig Hawker,Anders Hult,Michael Malkoch
Licensed Content Date	Nov 25, 2008
Licensed Content Volume	38
Licensed Content Issue	2
Type of Use	Thesis/Dissertation
Requestor type	academic/educational
Portion	figures/tables/images
Number of figures/tables/images	1
Distribution quantity	50
Format	print and electronic
Will you be translating?	no
Order reference number	
Title of the thesis/dissertation	Understanding the Structure-Function Relationship of Dendrimers in Environmental and Biomedical Applications
Expected completion date	Jul 2017
Estimated size	181
Requestor Location	Clemson University Clemson University Department of Physics and Astronomy

Permission for reproduction of figure 1.2

Title: Poly(amidoamine) (PAMAM) dendrimers: from biomimicry to drug delivery and biomedical applications

Author: Roseita Esfand,Donald A. Tomalia

Publication: Drug Discovery Today

Publisher: Elsevier

Date: 15 April 2001

Logged in as:
Bo Wang
Clemson University
Account #:
3001176633
LOGOUT

Order Completed

Thank you for your order.

This Agreement between Clemson University -- Bo Wang ("You") and Elsevier ("Elsevier") consists of your license details and the terms and conditions provided by Elsevier and Copyright Clearance Center.

Your confirmation email will contain your order number for future reference.

Printable details.

License Number	4156040572369
License date	Jul 25, 2017
Licensed Content Publisher	Elsevier
Licensed Content Publication	Drug Discovery Today
Licensed Content Title	Poly(amidoamine) (PAMAM) dendrimers: from biomimicry to drug delivery and biomedical applications
Licensed Content Author	Roseita Esfand,Donald A. Tomalia
Licensed Content Date	Apr 15, 2001
Licensed Content Volume	6
Licensed Content Issue	8
Licensed Content Pages	10
Type of Use	reuse in a thesis/dissertation
Portion	figures/tables/illustrations
Number of figures/tables/illustrations	1
Format	both print and electronic
Are you the author of this Elsevier article?	No
Will you be translating?	No
Original figure numbers	figure 2
Title of your thesis/dissertation	Understanding the Structure-Function Relationship of Dendrimers in Environmental and Biomedical Applications
Expected completion date	Jul 2017
Estimated size (number of pages)	181
Requestor Location	Clemson University Clemson University Department of Physics and Astronomy 118 Kinard Lab CLEMSON, SC 29634

Permission for reproduction of figure 1.3

Copyright Clearance Center RightsLink® Home Account Info Help

Title: Dendrimers in biomedical applications—reflections on the field
Author: Sönke Svenson,Donald A. Tomalia
Publication: Advanced Drug Delivery Reviews
Publisher: Elsevier
Date: December 2012

Logged in as:
Bo Wang
Clemson University
Account #:
3001176633
LOGOUT

Order Completed

Thank you for your order.

This Agreement between Clemson University -- Bo Wang ("You") and Elsevier ("Elsevier") consists of your license details and the terms and conditions provided by Elsevier and Copyright Clearance Center.

Your confirmation email will contain your order number for future reference.

Printable details.

License Number	4156041342707
License date	Jul 25, 2017
Licensed Content Publisher	Elsevier
Licensed Content Publication	Advanced Drug Delivery Reviews
Licensed Content Title	Dendrimers in biomedical applications—reflections on the field
Licensed Content Author	Sönke Svenson,Donald A. Tomalia
Licensed Content Date	Dec 1, 2012
Licensed Content Volume	64
Licensed Content Issue	n/a
Licensed Content Pages	14
Type of Use	reuse in a thesis/dissertation
Portion	figures/tables/illustrations
Number of figures/tables/illustrations	1
Format	both print and electronic
Are you the author of this Elsevier article?	No
Will you be translating?	No
Original figure numbers	figure 4
Title of your thesis/dissertation	Understanding the Structure-Function Relationship of Dendrimers in Environmental and Biomedical Applications
Expected completion date	Jul 2017
Estimated size (number of pages)	181
Requestor Location	Clemson University Clemson University Department of Physics and Astronomy 118 Kinard Lab CLEMSON, SC 29634 United States Attn: Clemson University
Publisher Tax ID	98-0397604

Permission for reproduction of figure 1.4

Order Completed

Thank you for your order.

This Agreement between Clemson University -- Bo Wang ("You") and Elsevier ("Elsevier") consists of your license details and the terms and conditions provided by Elsevier and Copyright Clearance Center.

Your confirmation email will contain your order number for future reference.

Printable details.

License Number	4156050020853
License date	Jul 25, 2017
Licensed Content Publisher	Elsevier
Licensed Content Publication	Progress in Polymer Science
Licensed Content Title	Dendrimer space concept for innovative nanomedicine: A futuristic vision for medicinal chemistry
Licensed Content Author	Serge Mignani,Saïd El Kazzouli,Mosto Bousmina,Jean-Pierre Majoral
Licensed Content Date	Jul 1, 2013
Licensed Content Volume	38
Licensed Content Issue	7
Licensed Content Pages	16
Type of Use	reuse in a thesis/dissertation
Portion	figures/tables/illustrations
Number of figures/tables/illustrations	1
Format	both print and electronic
Are you the author of this Elsevier article?	No
Will you be translating?	No
Original figure numbers	figure 8
Title of your thesis/dissertation	Understanding the Structure-Function Relationship of Dendrimers in Environmental and Biomedical Applications
Expected completion date	Jul 2017
Estimated size (number of pages)	181
Requestor Location	Clemson University Clemson University Department of Physics and Astronomy 118 Kinard Lab CLEMSON, SC 29634

Permission for reproduction of figure 1.5A

Title:	Dendrimer-protein interactions versus dendrimer-based nanomedicine
Author:	Dzmitry Shcharbin,Natallia Shcharbina,Volha Dzmitruk,Elzbieta Pedziwiatr-Werbicka,Maksim Ionov,Serge Mignani,F. Javier de la Mata,Rafael Gómez,Maria Angeles Muñoz-Fernández,Jean-Pierre Majoral,Maria Bryszewska
Publication:	Colloids and Surfaces B: Biointerfaces
Publisher:	Elsevier
Date:	1 April 2017

Logged in as:
Bo Wang
Clemson University
Account #:
3001176633
LOGOUT

Order Completed

Thank you for your order.

This Agreement between Clemson University -- Bo Wang ("You") and Elsevier ("Elsevier") consists of your license details and the terms and conditions provided by Elsevier and Copyright Clearance Center.

Your confirmation email will contain your order number for future reference.

Printable details.

License Number	4156050238791
License date	Jul 25, 2017
Licensed Content Publisher	Elsevier
Licensed Content Publication	Colloids and Surfaces B: Biointerfaces
Licensed Content Title	Dendrimer-protein interactions versus dendrimer-based nanomedicine
Licensed Content Author	Dzmitry Shcharbin,Natallia Shcharbina,Volha Dzmitruk,Elzbieta Pedziwiatr-Werbicka,Maksim Ionov,Serge Mignani,F. Javier de la Mata,Rafael Gómez,Maria Angeles Muñoz-Fernández,Jean-Pierre Majoral,Maria Bryszewska
Licensed Content Date	Apr 1, 2017
Licensed Content Volume	152
Licensed Content Issue	n/a
Licensed Content Pages	9
Type of Use	reuse in a thesis/dissertation
Portion	figures/tables/illustrations
Number of figures/tables/illustrations	1
Format	both print and electronic
Are you the author of this Elsevier article?	No
Will you be translating?	No
Original figure numbers	figure 1
Title of your thesis/dissertation	Understanding the Structure-Function Relationship of Dendrimers in Environmental and Biomedical Applications
Expected completion date	Jul 2017

Permission for reproduction of figure 1.5B

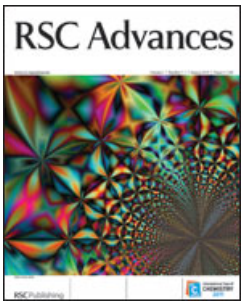

Title: Effects of dendrimer oil dispersants on Dictyostelium discoideum

Author: Nicholas K. Geitner,Rhonda R. Powell,Terri Bruce,David A. Ladner,Pu Chun Ke

Publication: RSC Advances

Publisher: Royal Society of Chemistry

Date: Oct 16, 2013

Logged in as:
Bo Wang
Clemson University
Account #:
3001176633
LOGOUT

Order Completed

Thank you for your order.

This Agreement between Clemson University -- Bo Wang ("You") and Royal Society of Chemistry ("Royal Society of Chemistry") consists of your license details and the terms and conditions provided by Royal Society of Chemistry and Copyright Clearance Center.

Your confirmation email will contain your order number for future reference.

Printable details.

License Number	4156050373117
License date	Jul 25, 2017
Licensed Content Publisher	Royal Society of Chemistry
Licensed Content Publication	RSC Advances
Licensed Content Title	Effects of dendrimer oil dispersants on Dictyostelium discoideum
Licensed Content Author	Nicholas K. Geitner,Rhonda R. Powell,Terri Bruce,David A. Ladner,Pu Chun Ke
Licensed Content Date	Oct 16, 2013
Licensed Content Volume	3
Licensed Content Issue	48
Type of Use	Thesis/Dissertation
Requestor type	academic/educational
Portion	figures/tables/images
Number of figures/tables/images	1
Distribution quantity	50
Format	print and electronic
Will you be translating?	no
Order reference number	
Title of the thesis/dissertation	Understanding the Structure-Function Relationship of Dendrimers in Environmental and Biomedical Applications
Expected completion date	Jul 2017
Estimated size	181
Requestor Location	Clemson University Clemson University Department of Physics and Astronomy 118 Kinard Lab

Permission for reproduction of figure 1.6

Permission for reproduction of "Structure-function relationship of dendrimers"

Title: Structure–Function Relationship of PAMAM Dendrimers as Robust Oil Dispersants

Author: Nicholas K. Geitner, Bo Wang, Rachel E. Andorfer, et al

Publication: Environmental Science & Technology

Publisher: American Chemical Society

Date: Nov 1, 2014

LOGIN

If you're a copyright.com user, you can login to RightsLink using your copyright.com credentials. Already **a RightsLink user** or want to learn more?

PERMISSION/LICENSE IS GRANTED FOR YOUR ORDER AT NO CHARGE

This type of permission/license, instead of the standard Terms & Conditions, is sent to you because no fee is being charged for your order. Please note the following:

- Permission is granted for your request in both print and electronic formats, and translations.
- If figures and/or tables were requested, they may be adapted or used in part.
- Please print this page for your records and send a copy of it to your publisher/graduate school.
- Appropriate credit for the requested material should be given as follows: "Reprinted (adapted) with permission from (COMPLETE REFERENCE CITATION). Copyright (YEAR) American Chemical Society." Insert appropriate information in place of the capitalized words.
- One-time permission is granted only for the use specified in your request. No additional uses are granted (such as derivative works or other editions). For any other uses, please submit a new request.

BACK CLOSE WINDOW

Permission for reproduction of "Mechanisms of dendrimer-small molecules binding"

Title: Deviation from the Unimolecular Micelle Paradigm of PAMAM Dendrimers Induced by Strong Interligand Interactions

Author: Bo Wang, Nicholas K. Geitner, Thomas P. Davis, et al

Publication: The Journal of Physical Chemistry C

Publisher: American Chemical Society

Date: Aug 1, 2015

LOGIN

If you're a copyright.com user, you can login to RightsLink using your copyright.com credentials. Already **a RightsLink user** or want to learn more?

PERMISSION/LICENSE IS GRANTED FOR YOUR ORDER AT NO CHARGE

This type of permission/license, instead of the standard Terms & Conditions, is sent to you because no fee is being charged for your order. Please note the following:

- Permission is granted for your request in both print and electronic formats, and translations.
- If figures and/or tables were requested, they may be adapted or used in part.
- Please print this page for your records and send a copy of it to your publisher/graduate school.
- Appropriate credit for the requested material should be given as follows: "Reprinted (adapted) with permission from (COMPLETE REFERENCE CITATION). Copyright (YEAR) American Chemical Society." Insert appropriate information in place of the capitalized words.
- One-time permission is granted only for the use specified in your request. No additional uses are granted (such as derivative works or other editions). For any other uses, please submit a new request.

BACK CLOSE WINDOW

Permission for reproduction of "Dendrimers as surfactants"
Permission don't need to be requested

Author reusing their own work published by the Royal Society of Chemistry

You do not need to request permission to reuse your own figures, diagrams, etc, that were originally published in a Royal Society of Chemistry publication. However, permission should be requested for use of the whole article or chapter except if reusing it in a thesis. If you are including an article or book chapter published by us in your thesis please ensure that your co-authors are aware of this.

Reuse of material that was published originally by the Royal Society of Chemistry must be accompanied by the appropriate acknowledgement of the publication. The form of the acknowledgement is dependent on the journal in which it was published originally, as detailed in 'Acknowledgements'.

Permission for reproduction of "Dendrimers inhibit protein amyloid aggregations"

Title: Inhibition of hIAPP Amyloid Aggregation and Pancreatic β-Cell Toxicity by OH-Terminated PAMAM Dendrimer

Author: Esteban N. Gurzov,Bo Wang,Emily H. Pilkington,Pengyu Chen,Aleksandr Kakinen,William J. Stanley,Sara A. Litwak,Eric G. Hanssen,Thomas P. Davis,Feng Ding,Pu Chun Ke

Publication: Small

Publisher: John Wiley and Sons

Date: Jan 25, 2016

Order Completed

Thank you for your order.

This Agreement between Clemson University -- Bo Wang ("You") and John Wiley and Sons ("John Wiley and Sons") consists of your license details and the terms and conditions provided by John Wiley and Sons and Copyright Clearance Center.

Your confirmation email will contain your order number for future reference.

Printable details.

License Number	4155991471896
License date	Jul 25, 2017
Licensed Content Publisher	John Wiley and Sons
Licensed Content Publication	Small
Licensed Content Title	Inhibition of hIAPP Amyloid Aggregation and Pancreatic β-Cell Toxicity by OH-Terminated PAMAM Dendrimer
Licensed Content Author	Esteban N. Gurzov,Bo Wang,Emily H. Pilkington,Pengyu Chen,Aleksandr Kakinen,William J. Stanley,Sara A. Litwak,Eric G. Hanssen,Thomas P. Davis,Feng Ding,Pu Chun Ke
Licensed Content Date	Jan 25, 2016
Licensed Content Pages	12
Type of use	Dissertation/Thesis
Requestor type	Author of this Wiley article
Format	Print and electronic
Portion	Full article
Will you be translating?	No
Title of your thesis / dissertation	Understanding the Structure-Function Relationship of Dendrimers in Environmental and Biomedical Applications
Expected completion date	Jul 2017
Expected size (number of pages)	181
Requestor Location	Clemson University Clemson University Department of Physics and Astronomy

REFERENCES

1. Crampton, H. L. & Simanek, E. E. Dendrimers as drug delivery vehicles: non-covalent interactions of bioactive compounds with dendrimers. *Polym. Int.* **56,** 489–496 (2007).
2. Carlmark, A., Hawker, C., Hult, A. & Malkoch, M. New methodologies in the construction of dendritic materials. *Chem. Soc. Rev.* **38,** 352–362 (2009).
3. Tomalia, D. A. & Fréchet, J. M. J. Discovery of dendrimers and dendritic polymers: A brief historical perspective*. *J. Polym. Sci. Part Polym. Chem.* **40,** 2719–2728 (2002).
4. Flory, P. J. Molecular Size Distribution in Three Dimensional Polymers. I. Gelation. *J. Am. Chem. Soc.* **63,** 3083–3090 (1941).
5. Svenson, S. & Tomalia, D. A. Dendrimers in biomedical applications--reflections on the field. *Adv. Drug Deliv. Rev.* **57,** 2106–2129 (2005).
6. Tomalia, D. A. Dendrimers — Nanoscopic Supermolecules According to Dendritic Rules and Principles. in *Supramolecular Stereochemistry* 21–26 (Springer, Dordrecht, 1995). doi:10.1007/978-94-011-0353-4_4
7. Hawker, C. & J. Fréchet, J. M. A new convergent approach to monodisperse dendritic macromolecules. *J. Chem. Soc. Chem. Commun.* **0,** 1010–1013 (1990).
8. Svenson, S. The dendrimer paradox – high medical expectations but poor clinical translation. *Chem. Soc. Rev.* **44,** 4131–4144 (2015).
9. Shcharbin, D. *et al.* Dendrimer-protein interactions versus dendrimer-based nanomedicine. *Colloids Surf. B Biointerfaces* **152,** 414–422 (2017).

10. Esfand, R. & Tomalia, D. A. Poly(amidoamine) (PAMAM) dendrimers: from biomimicry to drug delivery and biomedical applications. *Drug Discov. Today* **6,** 427–436 (2001).

11. Maiti, P. K., Çağın, T., Wang, G. & Goddard, W. A. Structure of PAMAM Dendrimers: Generations 1 through 11. *Macromolecules* **37,** 6236–6254 (2004).

12. Rosenfeldt, S. *et al.* Distribution of End Groups within a Dendritic Structure: A SANS Study Including Contrast Variation. *Macromolecules* **35,** 8098–8105 (2002).

13. Topp, A., Bauer, B. J., Tomalia, D. A. & Amis, E. J. Effect of Solvent Quality on the Molecular Dimensions of PAMAM Dendrimers. *Macromolecules* **32,** 7232–7237 (1999).

14. Prosa, T. J., Bauer, B. J. & Amis, E. J. From Stars to Spheres: A SAXS Analysis of Dilute Dendrimer Solutions. *Macromolecules* **34,** 4897–4906 (2001).

15. Martinho, N. *et al.* Molecular Modeling to Study Dendrimers for Biomedical Applications. *Molecules* **19,** 20424–20467 (2014).

16. Tomalia, D. A., Naylor, A. M. & Goddard, W. A. Starburst Dendrimers: Molecular-Level Control of Size, Shape, Surface Chemistry, Topology, and Flexibility from Atoms to Macroscopic Matter. *Angew. Chem. Int. Ed. Engl.* **29,** 138–175 (1990).

17. Naylor, A. M., Goddard, W. A., Kiefer, G. E. & Tomalia, D. A. Starburst dendrimers. 5. Molecular shape control. *J. Am. Chem. Soc.* **111,** 2339–2341 (1989).

18. Tian, W. & Ma, Y. Theoretical and computational studies of dendrimers as delivery vectors. *Chem. Soc. Rev.* **42,** 705–727 (2012).

19. Gennes, P. G. de & Hervet, H. Statistics of « starburst » polymers. *J. Phys. Lett.* **44,** 351–360 (1983).

20. Liu, Y., Bryantsev, V. S., Diallo, M. S. & Goddard, W. A. PAMAM dendrimers undergo pH responsive conformational changes without swelling. *J. Am. Chem. Soc.* **131,** 2798–9 (2009).

21. Hecht, S. & Fréchet, J. M. J. Dendritic Encapsulation of Function: Applying Nature's Site Isolation Principle from Biomimetics to Materials Science. *Angew. Chem. Int. Ed.* **40,** 74–91 (2001).

22. Hsu, H.-J., Bugno, J., Lee, S. & Hong, S. Dendrimer-based nanocarriers: a versatile platform for drug delivery. *Wiley Interdiscip. Rev. Nanomed. Nanobiotechnol.* **9,** n/a-n/a (2017).

23. Tomalia, D. A. Dendritic effects: dependency of dendritic nano-periodic property patterns on critical nanoscale design parameters (CNDPs). *New J. Chem.* **36,** 264–281 (2012).

24. Mignani, S., Kazzouli, S. E., Bousmina, M. & Majoral, J.-P. Dendrimer space concept for innovative nanomedicine: A futuristic vision for medicinal chemistry. *Prog. Polym. Sci.* **38,** 993–1008 (2013).

25. Mignani, S., El Kazzouli, S., Bousmina, M. M. & Majoral, J.-P. Dendrimer Space Exploration: An Assessment of Dendrimers/Dendritic Scaffolding as Inhibitors of Protein–Protein Interactions, a Potential New Area of Pharmaceutical Development. *Chem. Rev.* **114,** 1327–1342 (2014).

26. Maingi, V., Jain, V., Bharatam, P. V. & Maiti, P. K. Dendrimer building toolkit: Model building and characterization of various dendrimer architectures. *J. Comput. Chem.* **33,** 1997–2011 (2012).

27. Bhattacharya, P., Geitner, N. K., Sarupria, S. & Ke, P. C. Exploiting the physicochemical properties of dendritic polymers for environmental and biological applications. *Phys. Chem. Chem. Phys.* **15,** 4477–90 (2013).

28. Geitner, N. K. *et al.* Understanding dendritic polymer–hydrocarbon interactions for oil dispersion. *RSC Adv.* **2,** 9371 (2012).

29. DeFever, R. S. *et al.* PAMAM Dendrimers and Graphene: Materials for Removing Aromatic Contaminants from Water. *Environ. Sci. Technol.* **49,** 4490–4497 (2015).

30. Duncan, R. & Izzo, L. Dendrimer biocompatibility and toxicity. *Adv. Drug Deliv. Rev.* **57,** 2215–2237 (2005).

31. Wang, L. & Chen, C. Pathophysiologic mechanisms of biomedical nanomaterials. *Toxicol. Appl. Pharmacol.* **299,** 30–40 (2016).

32. Geitner, N. K., Powell, R. R., Bruce, T., Ladner, D. a. & Ke, P. C. Effects of dendrimer oil dispersants on Dictyostelium discoideum. *RSC Adv.* **3,** 25930 (2013).

33. Hong, S. *et al.* Interaction of Polycationic Polymers with Supported Lipid Bilayers and Cells: Nanoscale Hole Formation and Enhanced Membrane Permeability. *Bioconjug. Chem.* **17,** 728–734 (2006).

34. Lee, H. & Larson, R. G. Effects of PEGylation on the Size and Internal Structure of Dendrimers: Self-Penetration of Long PEG Chains into the Dendrimer Core. *Macromolecules* **44,** 2291–2298 (2011).

35. Barraza, L. F., Jiménez, V. A. & Alderete, J. B. Effect of PEGylation on the Structure and Drug Loading Capacity of PAMAM-G4 Dendrimers: A Molecular Modeling Approach on the Complexation of 5-Fluorouracil with Native and PEGylated PAMAM-G4. *Macromol. Chem. Phys.* n/a-n/a (2015). doi:10.1002/macp.201500179

36. Yang, L. & da Rocha, S. R. P. PEGylated, NH2-terminated PAMAM dendrimers: a microscopic view from atomistic computer simulations. *Mol. Pharm.* **11,** 1459–70 (2014).

37. Geitner, N. K. *et al.* Structure–Function Relationship of PAMAM Dendrimers as Robust Oil Dispersants. *Environ. Sci. Technol.* (2014). doi:10.1021/es5038194

38. Mahmoudi, M., Kalhor, H. R., Laurent, S. & Lynch, I. Protein fibrillation and nanoparticle interactions: opportunities and challenges. *Nanoscale* **5,** 2570–2588 (2013).

39. Gurzov, E. N. *et al.* Inhibition of hIAPP Amyloid Aggregation and Pancreatic β-Cell Toxicity by OH-Terminated PAMAM Dendrimer. *Small* **12,** 1615–1626 (2016).

40. Klajnert, B., Cortijo-Arellano, M., Cladera, J. & Bryszewska, M. Influence of dendrimer's structure on its activity against amyloid fibril formation. *Biochem. Biophys. Res. Commun.* **345,** 21–28 (2006).

41. The Art of Molecular Dynamics Simulation | Computational science and modelling. *Cambridge University Press* Available at: http://www.cambridge.org/us/academic/subjects/physics/computational-science-and-modelling/art-molecular-dynamics-simulation-2nd-edition. (Accessed: 27th February 2015)

42. Ding, F. & Dokholyan, N. V. Simple but predictive protein models. *Trends Biotechnol.* **23,** 450–455 (2005).

43. Ding, F., Tsao, D., Nie, H. & Dokholyan, N. V. Ab initio folding of proteins with all-atom discrete molecular dynamics. *Structure* **16,** 1010–8 (2008).

44. Lazaridis, T. & Karplus, M. Effective energy functions for protein structure prediction. *Curr. Opin. Struct. Biol.* **10,** 139–145 (2000).

45. Yin, S., Biedermannova, L., Vondrasek, J. & Dokholyan, N. V. MedusaScore: an accurate force field-based scoring function for virtual drug screening. *J. Chem. Inf. Model.* **48,** 1656–62 (2008).

46. Allen, M. P. & Tildesley, D. J. *Computer Simulation of Liquids*. (Clarendon Press, 1989).

47. Dagliyan, O., Proctor, E. A., D'Auria, K. M., Ding, F. & Dokholyan, N. V. Structural and dynamic determinants of protein-peptide recognition. *Struct. Lond. Engl. 1993* **19,** 1837–1845 (2011).

48. Wang, B. *et al.* Brushed polyethylene glycol and phosphorylcholine for grafting nanoparticles against protein binding. *Polym. Chem.* **7,** 6875–6879 (2016).

49. Ding, F. *et al.* Direct observation of a single nanoparticle–ubiquitin corona formation. *Nanoscale* **5,** 9162 (2013).

50. Tomalia, D. a. & Fréchet, J. M. J. Discovery of dendrimers and dendritic polymers: A brief historical perspective. *J. Polym. Sci. Part Polym. Chem.* **40,** 2719–2728 (2002).

51. Bhattacharya, P. *et al.* PAMAM dendrimer for mitigating humic foulant. *RSC Adv.* **2,** 7997 (2012).

52. Diallo, M. S. *et al.* Poly (amidoamine) Dendrimers : A New Class of High Capacity Chelating Agents for Cu (II) Ions. *Environ. Sci. Technol.* **33,** 820–4 (1999).

53. Xu, Y. & Zhao, D. Removal of copper from contaminated soil by use of poly(amidoamine) dendrimers. *Environ. Sci. Technol.* **39,** 2369–75 (2005).

54. Bradshaw, D. S. & Andrews, D. L. Mechanisms of Light Energy Harvesting in Dendrimers and Hyperbranched Polymers. *Polymers* **3,** 2053–2077 (2011).

55. Nantalaksakul, A., Reddy, D. R., Bardeen, C. J. & Thayumanavan, S. Light harvesting dendrimers. *Photosynth. Res.* **87,** 133–50 (2006).

56. Kurtoglu, Y. E., Mishra, M. K., Kannan, S. & Kannan, R. M. Drug release characteristics of PAMAM dendrimer-drug conjugates with different linkers. *Int. J. Pharm.* **384,** 189–94 (2010).

57. Chandrasekar, D., Sistla, R., Ahmad, F. J., Khar, R. K. & Diwan, P. V. The development of folate-PAMAM dendrimer conjugates for targeted delivery of anti-arthritic drugs and their pharmacokinetics and biodistribution in arthritic rats. *Biomaterials* **28,** 504–12 (2007).

58. Watkins, D. M., Sayed-sweet, Y., Klimash, J. W., Turro, N. J. & Tomalia, D. A. Dendrimers with Hydrophobic Cores and the Formation of Supramolecular Dendrimer - Surfactant Assemblies. *Langmuir* **13,** 3136–3141 (1997).

59. Jansen, J. F. G. A., Meijer, E. W. & de Brabander-van den Berg, E. M. M. The Dendritic Box: Shape-Selective Liberation of Encapsulated Guests. *J. Am. Chem. Soc.* **117,** 4417–4418 (1995).

60. Board, C. on E. of O. D. M. *Using Oil Spill Dispersants on the Sea*. 352 (National Academy Press, 1989).

61. Anderson, S. E., Franko, J., Lukomska, E. & Meade, B. J. Potential immunotoxicological health effects following exposure to COREXIT 9500A during cleanup of the Deepwater Horizon oil spill. *Science* **74,** 1419–30 (2011).

62. Goodbody-Gringley, G. *et al.* Toxicity of Deepwater Horizon source oil and the chemical dispersant, Corexit® 9500, to coral larvae. *PloS One* **8,** e45574 (2013).

63. Hemmer, M. J., Barron, M. G. & Greene, R. M. Comparative toxicity of eight oil dispersants, Louisiana sweet crude oil (LSC), and chemically dispersed LSC to two aquatic test species. *Environ. Toxicol. Chem.* **30,** 2244–52 (2011).

64. Petit, A.-N., Debenest, T., Eullaffroy, P. & Gagné, F. Effects of a cationic PAMAM dendrimer on photosynthesis and ROS production of Chlamydomonas reinhardtii. *Nanotoxicology* **6,** 315–26 (2012).

65. Cancino, J., Paino, I. M. M., Micocci, K. C., Selistre-de-Araujo, H. S. & Zucolotto, V. In vitro nanotoxicity of single-walled carbon nanotube-dendrimer nanocomplexes against murine myoblast cells. *Toxicol. Lett.* **219,** 18–25 (2013).

66. Lewis, T. & Ganesan, V. Interactions between Grafted Cationic Dendrimers and Anionic Bilayer Membranes. *J. Phys. Chem. B* **117,** 9806–20 (2013).

67. Thomas, T. P. *et al.* Cationic poly(amidoamine) dendrimer induces lysosomal apoptotic pathway at therapeutically relevant concentrations. *Biomacromolecules* **10,** 3207–3214 (2009).

68. Jones, C. F. *et al.* Cationic PAMAM dendrimers aggressively initiate blood clot formation. *ACS Nano* **6,** 9900–10 (2012).

69. Ciolkowski, M. *et al.* Surface modification of PAMAM dendrimer improves its biocompatibility. *Nanomed.* **8,** 815–7 (2012).

70. Maiti, P. K., Li, Y., Cagin, T. & Goddard, W. A. Structure of polyamidoamide dendrimers up to limiting generations: a mesoscale description. *J. Chem. Phys.* **130,** 144902 (2009).

71. Wu, B. *et al.* Structured water in polyelectrolyte dendrimers: understanding small angle neutron scattering results through atomistic simulation. *J. Chem. Phys.* **136,** 144901 (2012).

72. Wu, B. *et al.* Charge-dependent dynamics of a polyelectrolyte dendrimer and its correlation with invasive water. *J. Am. Chem. Soc.* **135,** 5111–7 (2013).

73. Liu, Y. *et al.* Effect of counterion valence on the pH responsiveness of polyamidoamine dendrimer structure. *J. Chem. Phys.* **132,** 124901 (2010).

74. Maingi, V., Kumar, M. V. S. & Maiti, P. K. PAMAM dendrimer-drug interactions: effect of pH on the binding and release pattern. *J. Phys. Chem. B* **116,** 4370–6 (2012).

75. Lin, S.-T., Maiti, P. K. & Goddard, W. A. Dynamics and thermodynamics of water in PAMAM dendrimers at subnanosecond time scales. *J. Phys. Chem. B* **109,** 8663–72 (2005).

76. Maiti, P. K. & Bagchi, B. Diffusion of flexible, charged, nanoscopic molecules in solution: Size and pH dependence for PAMAM dendrimer. *J. Chem. Phys.* **131,** 214901 (2009).

77. Ding, F. & Dokholyan, N. V. Emergence of protein fold families through rational design. *PLoS Comput. Biol.* **2,** e85 (2006).

78. Neria, E., Fischer, S. & Karplus, M. Simulation of activation free energies in molecular systems. *J. Chem. Phys.* **105,** 1902 (1996).

79. Lazaridis, T. & Karplus, M. Effective energy functions for protein structure prediction. *Curr Opin Struct Biol* **10,** 139–145 (2000).

80. Andersen, H. C. Molecular dynamics simulations at constant pressure and/or temperature. *J. Chem. Phys.* **72,** 2384 (1980).

81. Antosiewicz, J. M. & Shugar, D. Poisson-Boltzmann continuum-solvation models: applications to pH-dependent properties of biomolecules. *Mol. Biosyst.* **7,** 2923–49 (2011).

82. Porcar, L. *et al.* Structural Investigation of PAMAM Dendrimers in Aqueous Solutions Using Small-Angle Neutron Scattering : Effect of Generation Structural Investigation of PAMAM Dendrimers in Aqueous Solutions Using Small-Angle Neutron Scattering : Effect of Generation. *J Phys Chem B* **112,** 14772–14778 (2008).

83. Porcar, L. *et al.* Intramolecular Structural Change of PAMAM Dendrimers in Aqueous Solutions Revealed by Small-Angle Neutron Scattering. *J Phys Chem B* **114,** 1751–1756 (2010).

84. Liu, Y. *et al.* Electrostatic Swelling and Conformational Variation Observed in High-Generation Polyelectrolyte Dendrimers. *J. Phys. Chem. Lett.* **1,** 2020–2024 (2010).

85. Lee, H. & Larson, R. G. Molecular dynamics simulations of PAMAM dendrimer-induced pore formation in DPPC bilayers with a coarse-grained model. *J. Phys. Chem. B* **110,** 18204–11 (2006).

86. Niu, S., Turro, C., Bossmann, S. H., Tomalia, D. A. & Turro, N. J. Binding of *Ru(phen)32+ to Starburst Dendrimers and Its Quenching by Co(phen)33+: Generation Dependence of the Quenching Rate Constant. *J. Phys. Chem.* **99,** 5512–5517 (1995).

87. Helms, B. & Meijer, E. W. Dendrimers at Work. *Science* **313,** 929–930 (2006).

88. Newkome, G. R., Moorefield, C. N., Baker, G. R., Johnson, A. L. & Behera, R. K. Alkane Cascade Polymers Possessing Micellar Topology: Micellanoic Acid Derivatives. *Angew. Chem. Int. Ed. Engl.* **30,** 1176–1178 (1991).

89. Watkins, D. M., Sayed-Sweet, Y., Klimash, J. W., Turro, N. J. & Tomalia, D. A. Dendrimers with Hydrophobic Cores and the Formation of Supramolecular Dendrimer−Surfactant Assemblies. *Langmuir* **13,** 3136–3141 (1997).

90. Moreno-Bondi, M. C., Orellana, G., Turro, N. J. & Tomalia, D. A. Photoinduced electron-transfer reactions to probe the structure of starburst dendrimers. *Macromolecules* **23,** 910–912 (1990).

91. Turro, N. J., Barton, J. K. & Tomalia, D. A. Molecular recognition and chemistry in restricted reaction spaces. Photophysics and photoinduced electron transfer on the surfaces of micelles, dendrimers, and DNA. *Acc. Chem. Res.* **24,** 332–340 (1991).

92. Gopidas, K. R., Leheny, A. R., Caminati, G., Turro, N. J. & Tomalia, D. A. Photophysical investigation of similarities between starburst dendrimers and anionic micelles. *J. Am. Chem. Soc.* **113,** 7335–7342 (1991).

93. Maiti, P. K. & Bagchi, B. Diffusion of flexible, charged, nanoscopic molecules in solution: Size and pH dependence for PAMAM dendrimer. *J. Chem. Phys.* **131,** 214901 (2009).

94. Yiyun, C. & Tongwen, X. Dendrimers as potential drug carriers. Part I. Solubilization of non-steroidal anti-inflammatory drugs in the presence of polyamidoamine dendrimers. *Eur. J. Med. Chem.* **40,** 1188–1192 (2005).

95. Asthana, A., Chauhan, A. S., Diwan, P. V. & Jain, N. K. Poly(amidoamine) (PAMAM) dendritic nanostructures for controlled sitespecific delivery of acidic anti-inflammatory active ingredient. *AAPS PharmSciTech* **6,** E536–E542 (2005).

96. Kolhe, P., Misra, E., Kannan, R. M., Kannan, S. & Lieh-Lai, M. Drug complexation, in vitro release and cellular entry of dendrimers and hyperbranched polymers. *Int. J. Pharm.* **259,** 143–160 (2003).

97. Lin, S.-T., Maiti, P. K. & Goddard, W. A. Dynamics and Thermodynamics of Water in PAMAM Dendrimers at Subnanosecond Time Scales. *J. Phys. Chem. B* **109,** 8663–8672 (2005).

98. Liu, Y. *et al.* Effect of counterion valence on the pH responsiveness of polyamidoamine dendrimer structure. *J. Chem. Phys.* **132,** 124901 (2010).

99. Geitner, N. K. *et al.* Understanding dendritic polymer–hydrocarbon interactions for oil dispersion. *RSC Adv.* **2,** 9371–9375 (2012).

100. Bhattacharya, P. *et al.* PAMAM dendrimer for mitigating humic foulant. *RSC Adv.* **2,** 7997–8001 (2012).

101. Diallo, M. S. *et al.* Poly(amidoamine) Dendrimers: A New Class of High Capacity Chelating Agents for Cu(II) Ions. *Environ. Sci. Technol.* **33,** 820–824 (1999).

102. *Using Oil Spill Dispersants on the Sea*.

103. Hemmer, M. J., Barron, M. G. & Greene, R. M. Comparative toxicity of eight oil dispersants, Louisiana sweet crude oil (LSC), and chemically dispersed LSC to two aquatic test species. *Environ. Toxicol. Chem. SETAC* **30,** 2244–2252 (2011).

104. Anderson, S. E., Franko, J., Lukomska, E. & Meade, B. J. Potential Immunotoxicological Health Effects Following Exposure to COREXIT 9500A during Cleanup of the Deepwater Horizon Oil Spill. *J. Toxicol. Environ. Health A* **74,** 1419–1430 (2011).

105. Goodbody-Gringley, G. *et al.* Toxicity of Deepwater Horizon Source Oil and the Chemical Dispersant, Corexit® 9500, to Coral Larvae. *PLoS ONE* **8,** e45574 (2013).

106. Geitner, N. K., Powell, R. R., Bruce, T., Ladner, D. A. & Ke, P. C. Effects of dendrimer oil dispersants on Dictyostelium discoideum. *RSC Adv.* **3,** 25930–25936 (2013).

107. Mandal, T., Dasgupta, C. & Maiti, P. K. Nature of the effective interaction between dendrimers. *J. Chem. Phys.* **141,** 144901 (2014).

108. Ding, F., Tsao, D., Nie, H. & Dokholyan, N. V. Ab Initio Folding of Proteins with All-Atom Discrete Molecular Dynamics. *Structure* **16,** 1010–1018 (2008).

109. Ding, F., Furukawa, Y., Nukina, N. & Dokholyan, N. V. Local unfolding of Cu, Zn superoxide dismutase monomer determines the morphology of fibrillar aggregates. *J. Mol. Biol.* **421,** 548–560 (2012).

110. Ding, F. & Dokholyan, N. V. Emergence of Protein Fold Families through Rational Design. *PLoS Comput Biol* **2,** e85 (2006).

111. Manning, G. S. Limiting Laws and Counterion Condensation in Polyelectrolyte Solutions I. Colligative Properties. *J. Chem. Phys.* **51,** 924–933 (1969).

112. Kumar, S., Rosenberg, J. M., Bouzida, D., Swendsen, R. H. & Kollman, P. A. THE weighted histogram analysis method for free-energy calculations on biomolecules. I. The method. *J. Comput. Chem.* **13,** 1011–1021 (1992).

113. Neria, E., Fischer, S. & Karplus, M. Simulation of activation free energies in molecular systems. *J. Chem. Phys.* **105,** 1902–1921 (1996).

114. Maingi, V., Kumar, M. V. S. & Maiti, P. K. PAMAM Dendrimer–Drug Interactions: Effect of pH on the Binding and Release Pattern. *J. Phys. Chem. B* **116,** 4370–4376 (2012).

115. Maynard, A. D. *et al.* Safe handling of nanotechnology. *Nature* **444,** 267–269 (2006).

116. Ke, P. C. & Lamm, M. H. A biophysical perspective of understanding nanoparticles at large. *Phys. Chem. Chem. Phys.* **13,** 7273–7283 (2011).

117. Nel, A. E. *et al.* Understanding biophysicochemical interactions at the nano–bio interface. *Nat. Mater.* **8,** 543–557 (2009).

118. Lynch, I. & Dawson, K. A. Protein-nanoparticle interactions. *Nano Today* **3,** 40–47 (2008).

119. Cedervall, T. *et al.* Understanding the nanoparticle–protein corona using methods to quantify exchange rates and affinities of proteins for nanoparticles. *Proc. Natl. Acad. Sci.* **104,** 2050–2055 (2007).

120. Lundqvist, M. *et al.* Nanoparticle size and surface properties determine the protein corona with possible implications for biological impacts. *Proc. Natl. Acad. Sci.* **105,** 14265–14270 (2008).

121. Hellstrand, E. *et al.* Complete high-density lipoproteins in nanoparticle corona. *FEBS J.* **276,** 3372–3381 (2009).

122. Salvati, A. *et al.* Transferrin-functionalized nanoparticles lose their targeting capabilities when a biomolecule corona adsorbs on the surface. *Nat. Nanotechnol.* **8,** 137–143 (2013).

123. Deng, Z. J., Liang, M., Monteiro, M., Toth, I. & Minchin, R. F. Nanoparticle-induced unfolding of fibrinogen promotes Mac-1 receptor activation and inflammation. *Nat. Nanotechnol.* **6,** 39–44 (2011).

124. Ehrenberg, M. S., Friedman, A. E., Finkelstein, J. N., Oberdörster, G. & McGrath, J. L. The influence of protein adsorption on nanoparticle association with cultured endothelial cells. *Biomaterials* **30,** 603–610 (2009).

125. Walkey, C. D. *et al.* Protein Corona Fingerprinting Predicts the Cellular Interaction of Gold and Silver Nanoparticles. *ACS Nano* **8,** 2439–2455 (2014).

126. Shang, W., Nuffer, J. H., Dordick, J. S. & Siegel, R. W. Unfolding of Ribonuclease A on Silica Nanoparticle Surfaces. *Nano Lett.* **7,** 1991–1995 (2007).

127. Vroman, L., Adams, A. L., Fischer, G. C. & Munoz, P. C. Interaction of high molecular weight kininogen, factor XII, and fibrinogen in plasma at interfaces. *Blood* **55,** 156–159 (1980).

128. Radic, S. *et al.* Effect of fullerenol surface chemistry on nanoparticle binding-induced protein misfolding. *Nanoscale* **6,** 8340–8349 (2014).

129. Moyano, D. F. *et al.* Fabrication of Corona-Free Nanoparticles with Tunable Hydrophobicity. *ACS Nano* **8,** 6748–6755 (2014).

130. Mahmoudi, M. *et al.* Temperature: The 'Ignored' Factor at the NanoBio Interface. *ACS Nano* **7,** 6555–6562 (2013).

131. Chen, P. *et al.* Contrasting Effects of Nanoparticle Binding on Protein Denaturation. *J. Phys. Chem. C* **118,** 22069–22078 (2014).

132. Sotiriou, G. A. & Pratsinis, S. E. Antibacterial Activity of Nanosilver Ions and Particles. *Environ. Sci. Technol.* **44,** 5649–5654 (2010).

133. Kittler, S., Greulich, C., Diendorf, J., Köller, M. & Epple, M. Toxicity of Silver Nanoparticles Increases during Storage Because of Slow Dissolution under Release of Silver Ions. *Chem. Mater.* **22,** 4548–4554 (2010).

134. Tan, S., Erol, M., Attygalle, A., Du, H. & Sukhishvili, S. Synthesis of Positively Charged Silver Nanoparticles via Photoreduction of AgNO3 in Branched Polyethyleneimine/HEPES Solutions. *Langmuir* **23,** 9836–9843 (2007).

135. Ivask, A. *et al.* Toxicity Mechanisms in Escherichia coli Vary for Silver Nanoparticles and Differ from Ionic Silver. *ACS Nano* **8,** 374–386 (2014).

136. Hughes, Z. E., Wright, L. B. & Walsh, T. R. Biomolecular Adsorption at Aqueous Silver Interfaces: First-Principles Calculations, Polarizable Force-Field Simulations, and Comparisons with Gold. *Langmuir* **29,** 13217–13229 (2013).

137. Okamoto, Y. Generalized-ensemble algorithms: enhanced sampling techniques for Monte Carlo and molecular dynamics simulations. *J. Mol. Graph. Model.* **22,** 425–439 (2004).

138. Ding, F., Tsao, D., Nie, H. & Dokholyan, N. V. Ab Initio Folding of Proteins with All-Atom Discrete Molecular Dynamics. *Structure* **16,** 1010–1018 (2008).

139. Chen, L., Hodgson, K. O. & Doniach, S. A Lysozyme Folding Intermediate Revealed by Solution X-ray Scattering. *J. Mol. Biol.* **261,** 658–671 (1996).

140. Kiefhaber, T. Kinetic traps in lysozyme folding. *Proc. Natl. Acad. Sci.* **92,** 9029–9033 (1995).

141. Eleftheriou, M., Germain, R. S., Royyuru, A. K. & Zhou, R. Thermal Denaturing of Mutant Lysozyme with Both the OPLSAA and the CHARMM Force Fields. *J. Am. Chem. Soc.* **128,** 13388–13395 (2006).

142. Mahmoudi, M. *et al.* Protein−Nanoparticle Interactions: Opportunities and Challenges. *Chem. Rev.* **111,** 5610–5637 (2011).

143. Brancolini, G., Kokh, D. B., Calzolai, L., Wade, R. C. & Corni, S. Docking of Ubiquitin to Gold Nanoparticles. *ACS Nano* **6,** 9863–9878 (2012).

144. Shirvanyants, D., Ding, F., Tsao, D., Ramachandran, S. & Dokholyan, N. V. Discrete Molecular Dynamics: An Efficient And Versatile Simulation Method For Fine Protein Characterization. *J. Phys. Chem. B* **116,** 8375–8382 (2012).

145. Schmitz, O., Brock, B. & Rungby, J. Amylin Agonists: A Novel Approach in the Treatment of. *Diabetes* **53,** S233–S238 (2004).

146. Kahn, S. E., Andrikopoulos, S. & Verchere, C. B. Islet amyloid: a long-recognized but underappreciated pathological feature of type 2 diabetes. *Diabetes* **48,** 241–253 (1999).

147. Höppener, J. W. M., Ahrén, B. & Lips, C. J. M. Islet Amyloid and Type 2 Diabetes Mellitus. *N. Engl. J. Med.* **343,** 411–419 (2000).

148. Höppener, J. W. M. & Lips, C. J. M. Role of islet amyloid in type 2 diabetes mellitus. *Int. J. Biochem. Cell Biol.* **38,** 726–736 (2006).

149. Zraika, S. *et al.* Toxic oligomers and islet beta cell death: guilty by association or convicted by circumstantial evidence? *Diabetologia* **53,** 1046–1056 (2010).

150. Ritzel, R. A., Meier, J. J., Lin, C.-Y., Veldhuis, J. D. & Butler, P. C. Human Islet Amyloid Polypeptide Oligomers Disrupt Cell Coupling, Induce Apoptosis, and Impair Insulin Secretion in Isolated Human Islets. *Diabetes* **56,** 65–71 (2007).

151. Chakraborty, S., Chatterjee, B. & Basu, S. A mechanistic insight into the amyloidogenic structure of hIAPP peptide revealed from sequence analysis and molecular dynamics simulation. *Biophys. Chem.* **168–169,** 1–9 (2012).

152. Seino, S. & Study Group of Comprehensive Analysis of Genetic Factors in Diabetes Mellitus. S20G mutation of the amylin gene is associated with Type II diabetes in Japanese. Study Group of Comprehensive Analysis of Genetic Factors in Diabetes Mellitus. *Diabetologia* **44,** 906–909 (2001).

153. Sakagashira, S. *et al.* S20G Mutant Amylin Exhibits Increased in Vitro Amyloidogenicity and Increased Intracellular Cytotoxicity Compared to Wild-Type Amylin. *Am. J. Pathol.* **157,** 2101–2109 (2000).

154. Westermark, P., Andersson, A. & Westermark, G. T. Islet Amyloid Polypeptide, Islet Amyloid, and Diabetes Mellitus. *Physiol. Rev.* **91,** 795–826 (2011).

155. Cohen, F. E. & Kelly, J. W. Therapeutic approaches to protein-misfolding diseases. *Nature* **426,** 905–909 (2003).

156. Klabunde, T. *et al.* Rational design of potent human transthyretin amyloid disease inhibitors. *Nat. Struct. Biol.* **7,** 312–321 (2000).

157. Cao, P., Abedini, A. & Raleigh, D. P. Aggregation of islet amyloid polypeptide: from physical chemistry to cell biology. *Curr. Opin. Struct. Biol.* **23,** 82–89 (2013).

158. Westermark, P., Li, Z.-C., Westermark, G. T., Leckström, A. & Steiner, D. F. Effects of beta cell granule components on human islet amyloid polypeptide fibril formation. *FEBS Lett.* **379,** 203–206 (1996).

159. Abedini, A., Meng, F. & Raleigh, D. P. A single-point mutation converts the highly amyloidogenic human islet amyloid polypeptide into a potent fibrillization inhibitor. *J. Am. Chem. Soc.* **129,** 11300–11301 (2007).

160. Sellin, D., Yan, L.-M., Kapurniotu, A. & Winter, R. Suppression of IAPP fibrillation at anionic lipid membranes via IAPP-derived amyloid inhibitors and insulin. *Biophys. Chem.* **150,** 73–79 (2010).

161. Yan, L.-M., Velkova, A., Tatarek-Nossol, M., Andreetto, E. & Kapurniotu, A. IAPP Mimic Blocks Aβ Cytotoxic Self-Assembly: Cross-Suppression of Amyloid Toxicity of Aβ and IAPP Suggests a Molecular Link between Alzheimer's Disease and Type II Diabetes. *Angew. Chem. Int. Ed.* **46,** 1246–1252 (2007).

162. Yan, L.-M., Tatarek-Nossol, M., Velkova, A., Kazantzis, A. & Kapurniotu, A. Design of a mimic of nonamyloidogenic and bioactive human islet amyloid polypeptide (IAPP) as nanomolar affinity inhibitor of IAPP cytotoxic fibrillogenesis. *Proc. Natl. Acad. Sci. U. S. A.* **103,** 2046–2051 (2006).

163. Meng, F., Abedini, A., Plesner, A., Verchere, C. B. & Raleigh, D. P. The Flavanol (−)-Epigallocatechin 3-Gallate Inhibits Amyloid Formation by Islet Amyloid Polypeptide, Disaggregates Amyloid Fibrils, and Protects Cultured Cells against IAPP-Induced Toxicity. *Biochemistry (Mosc.)* **49,** 8127–8133 (2010).

164. Young, L. M. *et al.* Screening and classifying small-molecule inhibitors of amyloid formation using ion mobility spectrometry–mass spectrometry. *Nat. Chem.* **7,** 73–81 (2015).

165. Noor, H., Cao, P. & Raleigh, D. P. Morin hydrate inhibits amyloid formation by islet amyloid polypeptide and disaggregates amyloid fibers. *Protein Sci. Publ. Protein Soc.* **21,** 373–382 (2012).

166. Zelus, C. *et al.* Myricetin Inhibits Islet Amyloid Polypeptide (IAPP) Aggregation and Rescues Living Mammalian Cells from IAPP Toxicity. *Open Biochem. J.* **6,** 66–70 (2012).

167. Mishra, R., Sellin, D., Radovan, D., Gohlke, A. & Winter, R. Inhibiting Islet Amyloid Polypeptide Fibril Formation by the Red Wine Compound Resveratrol. *ChemBioChem* **10,** 445–449 (2009).

168. Tu, L.-H. *et al.* Mutational Analysis of the Ability of Resveratrol To Inhibit Amyloid Formation by Islet Amyloid Polypeptide: Critical Evaluation of the Importance of Aromatic–Inhibitor and Histidine–Inhibitor Interactions. *Biochemistry (Mosc.)* (2014). doi:10.1021/bi501016r

169. Daval, M. *et al.* The effect of curcumin on human islet amyloid polypeptide misfolding and toxicity. *Amyloid* **17,** 118–128 (2010).

170. Sparks, S., Liu, G., Robbins, K. J. & Lazo, N. D. Curcumin modulates the self-assembly of the islet amyloid polypeptide by disassembling α-helix. *Biochem. Biophys. Res. Commun.* **422,** 551–555 (2012).

171. Adessi, C. & Soto, C. Converting a peptide into a drug: strategies to improve stability and bioavailability. *Curr. Med. Chem.* **9,** 963–978 (2002).

172. Jones, C. F. *et al.* Cationic PAMAM dendrimers aggressively initiate blood clot formation. *ACS Nano* **6,** 9900–9910 (2012).

173. Geitner, N. K., Powell, R. R., Bruce, T., Ladner, D. A. & Ke, P. C. Effects of dendrimer oil dispersants on Dictyostelium discoideum. *RSC Adv.* **3,** 25930–25936 (2013).

174. DeFever, R. S. *et al.* PAMAM Dendrimers and Graphene: Materials for Removing Aromatic Contaminants from Water. *Environ. Sci. Technol.* **49,** 4490–4497 (2015).

175. Geitner, N. K. *et al.* Structure-function relationship of PAMAM dendrimers as robust oil dispersants. *Environ. Sci. Technol.* **48,** 12868–12875 (2014).

176. Klementieva, O. *et al.* Effect of poly(propylene imine) glycodendrimers on β-amyloid aggregation in vitro and in APP/PS1 transgenic mice, as a model of brain amyloid deposition and Alzheimer's disease. *Biomacromolecules* **14,** 3570–3580 (2013).

177. Supattapone, S., Nguyen, H. O., Cohen, F. E., Prusiner, S. B. & Scott, M. R. Elimination of prions by branched polyamines and implications for therapeutics. *Proc. Natl. Acad. Sci. U. S. A.* **96,** 14529–14534 (1999).

178. Klajnert, B. *et al.* The influence of densely organized maltose shells on the biological properties of poly(propylene imine) dendrimers: new effects dependent on hydrogen bonding. *Chem. Weinh. Bergstr. Ger.* **14,** 7030–7041 (2008).

179. Fischer, M. *et al.* Influence of surface functionality of poly(propylene imine) dendrimers on protease resistance and propagation of the scrapie prion protein. *Biomacromolecules* **11,** 1314–1325 (2010).

180. Supattapone, S. *et al.* Branched polyamines cure prion-infected neuroblastoma cells. *J. Virol.* **75,** 3453–3461 (2001).

181. Solassol, J. *et al.* Cationic phosphorus-containing dendrimers reduce prion replication both in cell culture and in mice infected with scrapie. *J. Gen. Virol.* **85,** 1791–1799 (2004).

182. McCarthy, J. M., Appelhans, D., Tatzelt, J. & Rogers, M. S. Nanomedicine for prion disease treatment: New insights into the role of dendrimers. *Prion* **7,** 198–202 (2013).

183. Nowacka, O., Shcharbin, D., Klajnert-Maculewicz, B. & Bryszewska, M. Stabilizing effect of small concentrations of PAMAM dendrimers at the insulin aggregation. *Colloids Surf. B Biointerfaces* **116,** 757–760 (2014).

184. Karolczak, K., Rozalska, S., Wieczorek, M., Labieniec-Watala, M. & Watala, C. Poly(amido)amine dendrimers generation 4.0 (PAMAM G4) reduce blood hyperglycaemia and restore impaired blood–brain barrier permeability in streptozotocin diabetes in rats. *Int. J. Pharm.* **436,** 508–518 (2012).

185. Cummin, B. M., Lim, J., Simanek, E. E., Pishko, M. V. & Coté, G. L. Encapsulation of a Concanavalin A/dendrimer glucose sensing assay within microporated poly (ethylene glycol) microspheres. *Biomed. Opt. Express* **2,** 1243–1257 (2011).

186. Nedumpully-Govindan, P. & Ding, F. Inhibition of IAPP aggregation by insulin depends on the insulin oligomeric state regulated by zinc ion concentration. *Sci. Rep.* **5,** (2015).

187. Kodali, R. & Wetzel, R. Polymorphism in the intermediates and products of amyloid assembly. *Curr. Opin. Struct. Biol.* **17,** 48–57 (2007).

188. Kayed, R. *et al.* Conformational transitions of islet amyloid polypeptide (IAPP) in amyloid formation in vitro. *J. Mol. Biol.* **287,** 781–796 (1999).

189. Liu, K. C. & Yeo, Y. Zwitterionic Chitosan–Polyamidoamine Dendrimer Complex Nanoparticles as a pH-Sensitive Drug Carrier. *Mol. Pharm.* **10,** 1695–1704 (2013).

190. Ban, T., Hamada, D., Hasegawa, K., Naiki, H. & Goto, Y. Direct Observation of Amyloid Fibril Growth Monitored by Thioflavin T Fluorescence ,. *J. Biol. Chem.* **278,** 16462–16465 (2003).

191. Khurana, R. *et al.* Mechanism of thioflavin T binding to amyloid fibrils. *J. Struct. Biol.* **151,** 229–238 (2005).

192. Wiltzius, J. J. W. *et al.* Atomic structure of the cross-β spine of islet amyloid polypeptide (amylin). *Protein Sci.* **17,** 1467–1474 (2008).

193. Hoorens, A., Van de Casteele, M., Klöppel, G. & Pipeleers, D. Glucose promotes survival of rat pancreatic beta cells by activating synthesis of proteins which suppress a constitutive apoptotic program. *J. Clin. Invest.* **98,** 1568–1574 (1996).

194. Bram, Y. *et al.* Apoptosis induced by islet amyloid polypeptide soluble oligomers is neutralized by diabetes-associated specific antibodies. *Sci. Rep.* **4,** (2014).

195. Nicoletti, I., Migliorati, G., Pagliacci, M. C., Grignani, F. & Riccardi, C. A rapid and simple method for measuring thymocyte apoptosis by propidium iodide staining and flow cytometry. *J. Immunol. Methods* **139,** 271–279 (1991).

196. Pillay, K. & Govender, P. Amylin uncovered: a review on the polypeptide responsible for type II diabetes. *BioMed Res. Int.* **2013,** 826706 (2013).

197. Feliu, N. *et al.* Next-generation sequencing reveals low-dose effects of cationic dendrimers in primary human bronchial epithelial cells. *ACS Nano* **9,** 146–163 (2015).

198. Li, S., Schöneich, C. & Borchardt, R. T. Chemical instability of protein pharmaceuticals: Mechanisms of oxidation and strategies for stabilization. *Biotechnol. Bioeng.* **48,** 490–500 (1995).

199. Katarzyna Winnicka, K. B. The Effect of Generation 2 and 3 Poly(amidoamine) Dendrimers on Viability of Human Breast Cancer Cells. *J. Health Sci. - J Health SCI* **55,** 169–177 (2009).

200. Wang, B. *et al.* Thermostability and reversibility of silver nanoparticle–protein binding. *Phys. Chem. Chem. Phys.* **17,** 1728–1739 (2014).

201. Shirvanyants, D., Ding, F., Tsao, D., Ramachandran, S. & Dokholyan, N. V. Discrete molecular dynamics: an efficient and versatile simulation method for fine protein characterization. *J. Phys. Chem. B* **116,** 8375–8382 (2012).

202. Karginov, A. V., Ding, F., Kota, P., Dokholyan, N. V. & Hahn, K. M. Engineered allosteric activation of kinases in living cells. *Nat. Biotechnol.* **28,** 743–747 (2010).

203. Yin, S., Biedermannova, L., Vondrasek, J. & Dokholyan, N. V. MedusaScore: An Accurate Force Field-Based Scoring Function for Virtual Drug Screening. *J. Chem. Inf. Model.* **48,** 1656–1662 (2008).

204. Nanga, R. P. R., Brender, J. R., Vivekanandan, S. & Ramamoorthy, A. Structure and membrane orientation of IAPP in its natively amidated form at physiological pH in a membrane environment. *Biochim. Biophys. Acta BBA - Biomembr.* **1808,** 2337–2342 (2011).

205. Srinivasan, R. & Rose, G. D. A physical basis for protein secondary structure. *Proc. Natl. Acad. Sci. U. S. A.* **96,** 14258–14263 (1999).

206. Ding, F., LaRocque, J. J. & Dokholyan, N. V. Direct Observation of Protein Folding, Aggregation, and a Prion-like Conformational Conversion. *J. Biol. Chem.* **280,** 40235–40240 (2005).

207. McKenzie, M. D. *et al.* Perforin and Fas induced by IFNγ and TNFα mediate beta cell death by OT-I CTL. *Int. Immunol.* **18,** 837–846 (2006).

208. McKenzie, M. D. *et al.* Glucose induces pancreatic islet cell apoptosis that requires the BH3-only proteins Bim and Puma and multi-BH domain protein Bax. *Diabetes* **59,** 644–652 (2010).

209. Casas, S., Novials, A., Reimann, F., Gomis, R. & Gribble, F. M. Calcium elevation in mouse pancreatic beta cells evoked by extracellular human islet amyloid polypeptide involves activation of the mechanosensitive ion channel TRPV4. *Diabetologia* **51,** 2252–2262 (2008).

210. Chiti, F. & Dobson, C. M. Protein Misfolding, Functional Amyloid, and Human Disease. *Annu. Rev. Biochem.* **75,** 333–366 (2006).

211. Shcharbin, D., Klajnert, B. & Bryszewska, M. The effect of PAMAM dendrimers on human and bovine serum albumin at different pH and NaCl concentrations. *J. Biomater. Sci. Polym. Ed.* **16,** 1081–1093 (2005).

212. Giri, J. *et al.* Interactions of Poly(amidoamine) Dendrimers with Human Serum Albumin: Binding Constants and Mechanisms. *ACS Nano* **5,** 3456–3468 (2011).

213. Zhang, H.-M., Lou, K., Cao, J. & Wang, Y.-Q. Interaction of a Hydrophobic-Functionalized PAMAM Dendrimer with Bovine Serum Albumin: Thermodynamic and Structural Changes. *Langmuir* **30,** 5536–5544 (2014).

214. Gabellieri, E., Strambini, G. B., Shcharbin, D., Klajnert, B. & Bryszewska, M. Dendrimer–protein interactions studied by tryptophan room temperature phosphorescence. *Biochim. Biophys. Acta BBA - Proteins Proteomics* **1764,** 1750–1756 (2006).

215. Shcharbin, D. *et al.* Impact of PAMAM G2 and G6 dendrimers on bovine serum albumin (fatty acids free and loaded with different fatty acids). *Colloids Surf. B Biointerfaces* **63,** 27–33 (2008).

216. Shcharbin, D. *et al.* Serum albumins have five sites for binding of cationic dendrimers. *Biochim. Biophys. Acta BBA - Proteins Proteomics* **1774,** 946–951 (2007).

217. Froehlich, E., Mandeville, J. S., Jennings, C. J., Sedaghat-Herati, R. & Tajmir-Riahi, H. A. Dendrimers Bind Human Serum Albumin. *J. Phys. Chem. B* **113,** 6986–6993 (2009).

218. Sekowski, S. *et al.* The interaction between PAMAM G3.5 dendrimer, Cd2+, dendrimer–Cd2+ complexes and human serum albumin. *Colloids Surf. B Biointerfaces* **69,** 95–98 (2009).